FLUID DYNAMICS NUMERICAL MODELING OF SECOND-MODE INSTABILITY MECHANISMS AT MACH 6

by

Armani Batista

A dissertation submitted to the Faculty of the University of Delaware in partial fulfillment of the requirements for the degree of Doctor of Philosophy in Mechanical Engineering

Summer 2019

FLUID DYNAMICS NUMERICAL MODELING OF SECOND-MODE INSTABILITY MECHANISMS AT MACH 6

by

Armani Batista

Approved: ______________________________

Ajay K. Prasad, Ph.D.
Chair of the Department of Mechanical Engineering

Approved: ______________________________

Levi T. Thompson, Ph.D.
Dean of the College of Engineering

Approved: ______________________________

Douglas J. Doren, Ph.D.
Interim Vice Provost for Graduate and Professional Education and Dean of the Graduate College

I certify that I have read this dissertation and that in my opinion it meets the academic and professional standard required by the University as a dissertation for the degree of Doctor of Philosophy.

Signed: ______________________________

Joseph J. Kuehl, Ph.D.
Professor in charge of dissertation

I certify that I have read this dissertation and that in my opinion it meets the academic and professional standard required by the University as a dissertation for the degree of Doctor of Philosophy.

Signed: ______________________________

Ajay K. Prasad, Ph.D.
Member of dissertation committee

I certify that I have read this dissertation and that in my opinion it meets the academic and professional standard required by the University as a dissertation for the degree of Doctor of Philosophy.

Signed: ______________________________

Lian-Ping Wang, Ph.D.
Member of dissertation committee

I certify that I have read this dissertation and that in my opinion it meets the academic and professional standard required by the University as a dissertation for the degree of Doctor of Philosophy.

Signed: ______________________________

Fabrice Veron, Ph.D.
Member of dissertation committee

ACKNOWLEDGEMENTS

First and foremost, I would like to thank God. Next, I want to say thank you to my wife Rosa Sendy Batista for moving with me 5 times, over 6 years, in 3 different states (California, Texas, and Delaware), on both coasts of this country in pursuit of the Ph.D. Thank you to my advisor Dr. Joe Kuehl, including his guidance and never being too busy to answer my myriad of on-going questions. To my committee members Dr. Ajay Prasad, Dr. Lian-Ping Wang, and Dr. Fabrice Veron for all their help and support. I'd also like to thank our collaborations: Dr. Steven Schneider, Dr. Brandon Chynoweth, Dr. Carlo Scalo, Victor Sousa, Dr. Hermann Fasel, Dr. Christoph Hader, Dr. Thomas Juliano, and Dr. Bradley Wheaton. Finally, I want to thank my grandmother Barbara Jean Young and Dr. Keith Evan Schubert for their continued support and guidance throughout my education.

TABLE OF CONTENTS

LIST OF TABLES

LIST OF FIGURES

LIST OF SYMBOLS

A	Wave amplitude
c_p	Specific heat at constant pressure
c_v	Specific heat at constant volume
M	Mach number
m	Mass or meters (context provided by text)
mm	Millimeters
$N - factor$	Non-dimensional of the natural log (ln) of amplitude ratios
P	Pressure [Pa]
R_n	Nose radius [mm] or [in]
Re	Reynolds number
s	Entropy [J/K]
T	Temperature [K]
t	time [s]
U	Streamwise velocity [m/s]
u	Streamwise velocity [m/s]
v	Wall-normal velocity [m/s]
W	Weight function
w	Azimuthal velocity [m/s]
x	Streamwise direction [m]
y	Wall-normal direction [m]
z	Azimuthal direction [m]
α	Streamwise wave number
β	Crossflow wave number
γ	Specific heat ratio

ν	Kinematic viscosity [m^2/s]
ρ	Density [kg/m]
Σ	Summation
σ	Bandwidth deviation
Φ	Generic wave variable
ϕ	Generic flow variable
ω	Frequency [kHz]
$'$	Disturbance quantity or wall-normal derivative (context provided by text)
$\bar{}$	Basic state identifier or slow variable assumption (context provided by text)
$\hat{}$	Generalized inflection point criteria identifier (context provided by text)
Subscript	
0	Stagnation quantity
e	Boundary layer edge quantity
i	Variable number
k	Index number
∞	Freestream quantity

LIST OF ABBREVIATIONS AND ACRONYMS

AFOSR	Air Force Office of Scientific Research
BAM6QT	Boeing/AFOSR Mach-6 Quiet Tunnel
CFD	Computational Fluid Dynamics
DNS	Direct Numerical Simulation
LPSE	Linear Parabolized Stability Equations
LST	Linear Stability Theory
NPSE	Nonlinear Parabolized Stability Equations
PSD	Power Spectral Density
PSE	Parabolized Stability Equations
TSP	Temperature Sensitive Paint

ABSTRACT

This research is a numerical investigation of second-mode stability behavior within hypersonic boundary layers. Two-dimensional, hypersonic boundary layer stability and transition is dominated by second-mode acoustic disturbances at freestream Mach numbers of 4 and higher as shown by Mack. However, the physical mechanisms and amplitude based prediction of the second-mode is not fully understood which are important for sustained and controlled hypersonic flight to become feasible. In this research, the modeled hypersonic flow conditions corresponded to a flared cone tested in the Boeing/AFOSR Mach-6 Quiet Tunnel at Purdue University, and 7 degree half angle straight cones with various nose radii at the new AFOSR-Notre Dame Large Mach 6 Quiet Tunnel. The methodology employed used a computational fluid dynamics (CFD) solver US3D to generate a laminar, steady state solution (basic state). Then, the basic state is fed into stability solvers. Starting with linear stability theory (LST) which is a generalized eigenvalue solver, which also serves as the initial condition for linear and nonlinear parabolized stability equations (PSE) to calculate the disturbance behavior. These stability results are then compared to experimental data and direct numerical simulations (DNS).

Two recent contributions by Kuehl (2017 and 2018) were made regarding second-mode disturbances. The first was the reformulation of the nonlinear parabolized stability equations (NPSE) to quantify the finite bandwidth nature (wavepackets) of the second-mode disturbances. The second was the proposed thermoacoustic interpretation which describes the fundamental physics of second-modes as trapped acoustic waves within an acoustic impedance well. These contributions raised new questions regarding the applications and implications of second-mode behavior. These questions were investigated in this research for improved amplitude based modeling of second-mode physics.

Specifically, the following objectives were achieved: wavepacket applications and implications, comparisons of PSE results with experimental data and direct numerical simulation (DNS), applications and implications of the thermoacoustic interpretation, and exploiting this to understand and develop novel second-mode control methods.

Utilizing and improving the wavepacket formulation within NPSE led to second-mode amplitudes between 20% to 40% on the Purdue flared cone. This is in good agreement with Purdue experimental results of ∼30%. Another important implication was the onset of spectral broadening which identifies the region where nonlinearities begin to assert themselves. This is where the amplitude ratio of the primary disturbance divided by the first harmonic begin to non-negligibly decrease when moving downstream. As such, the wavepacket NPSE showed the onset of spectral broadening was identified and produced good agreement to experimental results of amplitude ratio. Also, the wavepacket NPSE had good agreement with DNS results for the primary mode and the first harmonic. Therefore, the wavepacket NPSE is capable of improved numerical modeling and amplitude prediction of the second-mode disturbance.

Regarding the thermoacoustic interpretation, it suggests that the second-mode disturbance growth or suppression is tied directly to the strength of the basic state density gradient. The interpretation was applied to identify the physical mechanism for the downstream movement of the transition front caused by increasing the nose radius of a cone. This was an important first step in understanding the blunt body paradox, where once a critical nose radius (bluntness) is reached, transition jumps forward. It was shown that if entropy disrupts the proper formation of the acoustic impedance well by diluting the density gradient, the well becomes weakened, and the second-mode disturbance is no longer able to resonate, thereby suppressing its growth. Conversely, a well-defined density gradient allows acoustic disturbances to resonate within the boundary layer inducing second-mode growth. Subsequently, a criterion was developed based on Lees and Lin generalized inflection point criterion to quantify when the density gradient is strong enough for second-modes to be present.

Finally, the thermoacoustic interpretation aided in describing the behavior of second-mode amplification and damping when cooling and heating the wall of the Purdue flared cone. It was shown that cooling and heating the wall effects the acoustic impedance well length scale, thereby changing the resonant frequency of the second-mode. This led to the concept of upstream cooling and downstream heating which showed potential max N-factor damping of three compared to a non-cooled/heated wall.

Chapter 1

INTRODUCTION

1.1 Overview

1.1.1 Motivation

Controlled and sustained hypersonic flight remains an open problem and a U.S. national priority. Several gaps in fundamental knowledge exist which must be addressed before sustained flight operations can be achieved that analog the commercial aviation industry or applications related to civil defense [1, 2]. One important, open question is a fundamental understanding of the physical mechanisms responsible for the transition from a laminar to a turbulent boundary layer (the "transition" problem) [2, 3]. At high Mach numbers (ie. $10 < \mathrm{M} < 50$; relevant to atmospheric re-entry), these gaps in knowledge take the form of aerothermodynamic heating, chemical non-equilibrium, ablation, and more [1, 3]. Even at lower hypersonic Mach numbers ($3 < \mathrm{M} < 10$), where the compressible Navier-Stokes equations and ideal assumptions hold, these gaps in knowledge persist [1, 3]. It is this lower hypersonic Mach number range which is the focus of this research.

Beyond the scientific implications, a commonly used engineering example for the benefit of sustained hypersonic flight is a non-stop flight from New York to Los Angeles. On a typical, transonic, commercial aircraft, this flight takes about 6 hours. Whereas, a hypersonic aircraft at Mach 5 would take only about 1 hour to make the same trip. Clearly, such hypersonic transit would yield significant logistical benefits to commercial air travel and cargo transportation. In addition to commercial applications, military and civil defense applications are numerous. Another application is atmospheric re-entry. During re-entry into the Earth's atmosphere, or entry into another planetary atmosphere, a vehicle traverses through a wide range of hypersonic conditions (from Mach $\approx$ 3 to 50). As such, these vehicles' flight dynamics traverse many physical and chemical phenomena [1, 3].

The effect of transition on aerothermal heating of a vehicle is important. Turbulent boundary layers experience about 5-10 times larger heating than equivalent laminar boundary layer [2, 3, 4]. Thus, delaying the transition from laminar to turbulent flow over a vehicle results in significant reduction in thermal load. This allows for a more efficient vehicle design by reducing the amount of heat shielding required. The effect of transition on flight trajectory accuracy is slightly more subtle. Consider a laminar boundary layer over a streamlined vehicle. Laminar boundary layers result in less skin-friction drag than turbulent boundary layers. If the vehicle experiences asymmetric transition (ie. one side of the vehicle is laminar and the other side is turbulent), an asymmetric drag will result. Due to their streamlined nature, hypersonic vehicles have limited control surface functionality. Such asymmetric drag can overwhelm vehicle control capability, potentially resulting in loss of vehicle flight stability and catastrophic vehicle failure [2, 5].

1.1.2 Document Organization

The next few sections describe the goal, objectives, and methodology of this research. Chapter 2 provides the background and literature review of hypersonic boundary layer stability as applied to second-mode disturbance analysis on the Mach 6 Purdue flared cone. Chapter 3 covers the hypersonic computational fluid dynamics (CFD) research methodology for numerical stability analysis. Chapters 4 through 8 are results based on published conference papers and journal articles. Specifically, chapters 4, 5, and 6 address the first 3 objectives of this research on wavepacket analysis, and chapters 7 and 8 address the remaining 2 objectives on thermoacoustic interpretation and control. Chapter 9 presents a summary of the completed research objectives and conclusions of this research. Finally, chapter 10 includes future work pertaining to the research objectives in this dissertation. Note, the appendix provides a brief overview and reference of hypersonic flows.

1.2 Research Goal

Laminar to turbulent hypersonic boundary layer stability and transition (BLST) is a rich topic with a variety of interesting open questions due to its inherent nonlinear nature. Publications encompassing hypersonic flow and BLST phenomena with respect to the theoretical, experimental, and numerical determinations were reviewed in this research. It was Mack who first showed that first-mode ($1 < M < 4$) and second-mode ($4 < M$) instabilities are the most amplified disturbances within two dimensional (or axisymmetric) boundary layers at supersonic and hypersonic velocities respectively [6]. The ultimate goal of this research is to better understand the physical mechanisms, evolution, and nonlinear (amplitude based) modeling/prediction of the "second-mode" instability. Specifically, this research aims to numerically show how second-mode instabilities within the boundary layer grow, decay, and interact linearly and nonlinearly as a precursor to transition. Such understanding is necessary for the development of transition control schemes and thereby paving the way towards sustained hypersonic flight.

1.3 Research Objectives

1.3.1 Wavepackets

In 2017, Kuehl reformulated the nonlinear parabolized stability equations (NPSE) to consider finite bandwidth disturbances (ie. wavepackets) and showed that such a formulation improved the numerical representation of nonlinear energy transfer between disturbances in the boundary layer [7]. This new formulation created a series of new questions. What wavepacket bandwidths should be used? How many primary disturbances should be employed? In general, what are the implications of using wavepackets to model disturbance physics on the Purdue flared cone at Purdue Boeing/AFOSR Mach-6 Quiet Tunnel conditions? The specific research objectives for wavepackets are:

1. Research applications and implications of modeling boundary layer disturbances as wavepackets.

2. Conduct a comparison between the PSE wavepacket formulation and experimental data.

3. Conduct a comparison between the PSE wavepacket formulation and DNS computations.

1.3.2 Thermoacoustic Resonance

Recently, a new theory describing the fundamental physics of second-modes was proposed (Kuehl 2018) [8]. It hypothesizes that second-modes behave as trapped acoustic waves which are resonating in an acoustic impedance well and that the fundamental mechanism for disturbance growth is thermoacoustic Reynolds stress. However, the proper implications and applications of the theory remained. For instance, the theory described that a thermoacoustic impedance well must be present for second-modes to grow, and laid the groundwork for determining the strength of the well necessary to support second-mode growth, via the generalized inflection point criterion. However, it did not explicitly describe how to apply this criterion, particularly in the case of competing density and velocity gradients, nor how to interpret when the second-mode is present in such a situation. An example of when such details are particularly important, is the case of blunt bodies. Specifically the blunt body paradox: where transition moves downstream with increasing nose cone radii, then suddenly jumps upstream for a critical (sufficiently large) nose radius or bluntness. Below are the two objectives within this sub-topic, bringing the total to five objectives.

4. Research applications and implications of thermoacoustic interpretation of second-mode instability.

5. Exploit this new interpretation to develop novel control methods, and a better understanding of existing control schemes.

1.4 Research Methodology Overview

Although experimental investigation in the form of flight and wind-tunnel testing are the standards for discovering the physical behavior of hypersonic phenomena and qualifying vehicle designs, these methods are not readily available for everyone. As such, computational fluid dynamics (CFD) and numerical analysis were the primary methods employed to conduct this research. Then, these numerical results were compared with experimental and direct numerical simulations (DNS) data kindly provided by our collaborators, and previously established theoretical findings to validate the results. We are calling this approach the hypersonic CFD stability analysis process.

The dynamics quantified encompass the linear and weakly-to-moderate nonlinear dynamics flow regime of hypersonic boundary layer disturbances leading up to laminar to turbulent transition. Linear stability theory (LST) and linear/nonlinear parabolized stability equations (PSE) results were compared with direct numerical simulations (DNS) and quiet hypersonic wind tunnel experimental measurements. In general, this first required the generation of a steady state CFD solution (basic state) of a hypersonic flow field. Then, the disturbance equation was solved on this basic state by performing stability analysis. Two forms of linear stability theory were utilized: 1. A traditional eigenvalue problem solver (standard LST); 2. A linear parabolized stability equations (LPSE) solver. In addition, a nonlinear parabolized stability equations (NPSE) solver was employed to study the nonlinear behavior of disturbance evolution. The particular solver used, called JoKHeR [9], was originally developed by Dr. Kuehl and Dr. Helen Reed as part of the National Center for Hypersonic Laminar-Turbulent Transition.

The primary geometries considered were the Purdue flared cone and the Notre Dame cones at Mach 6. The Purdue flared cone was specifically designed with a 3 meter radius flare to isolate second-mode dynamics, and thus exhibits second-mode driving transition at the Purdue Quiet Tunnel conditions [10, 11]. Also, there is a large amount of high-quality benchmark data (experimental and numerical) available for comparison. This data is extremely valuable for physics-driven analysis [11]. The other geometry considered are the Notre Dame cones which are 7 degree half angle straight cones to be fabricated and tested in the new, AFOSR-Notre Dame Large Mach 6 Quiet Tunnel.

Chapter 2

BACKGROUND

2.1 Hypersonic Flow Background

We begin with a brief review of boundary layers in general. Next, some of the particulars of hypersonic boundary layers are mentioned. Then, moving onto stability and transition of boundary layers. Finally, the literature review which encompasses hypersonic BLST theoretical, experimental, and computational is reviewed with respect to the Mach 6 Purdue flared cone. An overview of compressible, supersonic, and hypersonic flow aspects is not covered here, but is included in appendix A.

2.1.1 Boundary Layers

2.1.1.1 Overview

Prandtl stated that a moving fluid can be broken up into an inviscid flow region, and a thin viscous region called a boundary layer [12, 13]. The implication of the boundary layer is that it allows a divide and conquer approach to be taken which greatly simplifies solving the governing equations by isolating where change to the flow occurs with regards to viscosity, energy transfer, and chemical reactions. The viscous boundary layer typically considered in fluid mechanics is with respect to the velocity gradient. It will be hard to get past review if we don't address the small scales. Starting from the wall, where the no-slip condition imposes zero velocity of the fluid velocity in the x-direction denoted $\mathrm{u} = \mathrm{u(y)}$ where u is a function of y. The u velocity increases until $\mathrm{u} = \mathrm{U}_\infty$ which is the velocity in the inviscid flow region or freestream velocity. Next, in heat transfer a thermal boundary layer is considered, which in high-speed flows can also become important as the temperature gets high. Lastly, in chemically reacting flows are occurring such as at high Mach numbers, a mass diffusion boundary layer may also be considered.

2.1.1.2 Hypersonic Boundary Layers

There are many special phenomena which are unique to hypersonic boundary layers. Shock boundary layer interactions are the result of secondary shocks forming off control surfaces or at very high Mach numbers, when shock can become very close to the body [1, 3]. Of course, acoustic instabilities exist in hypersonic boundary layers as mentioned in chapter 1. These acoustic instabilities can be thought of as acoustic waves propagating within the boundary layer [14]. This brings forth the idea of a relative sonic-line which would be the height above the wall where the fluid reaches a velocity of Mach 1 [14]. The relative sonic-line corresponds to a turning point in the inviscid governing equations of motion. Between the wall and the turning point, the flow exhibits oscillating solutions, while beyond the turning point the solutions are exponentially decaying [14]. Depending on the situation, the relative sonic line may be within, equal to or greater than the boundary layer height. The location of the turning point affects the acoustic disturbance frequencies as the distance from the wall will change the rate of oscillation [14]. The thermoacoustic interpretation provides a more physical explanation for this behavior, which will be discussed in section 2.3 [8]. Particularly important for blunt nosed geometries, entropy generated by curved shocks can impinge on the vehicle wall creating an entropy layer that interacts with the boundary layer [3]. The entropy layer adversely affects the acoustic impedance well, thereby altering the dynamics of acoustic waves in high-speed boundary layers [8]. A sufficiently large nose radius can even change the fundamental type of transition observed, the so-called "blunt body paradox" [15].

2.2 Stability and Transition

To consider the stability and transition from laminar to turbulent fluid flow, one can take a step back, and recall Reynolds pipe flow experiment in 1883. Reynolds observed that the flow would transition from laminar to turbulent when $(v_{avg}D)/\nu \approx 3000$, where v = velocity, D = pipe diameter, and ν = kinematic viscosity. This criteria would later be called the critical Reynolds number (Re_{cr}), by Orr and Sommerfeld, who derived the stability equations for small disturbances in parallel flows. The general solution form of the Orr-Sommerfeld equation is: $v' = v(y)e^{i(\alpha x+\beta z-\omega t)}$, where x,y,z are spatial coordinates, t is time, α and β are the wavenumbers, and ω is the angular frequency. Later, Tollmien solved the Orr-Sommerfeld equation for a Blasius boundary layer which defined Re_{cr} for the Blasius case. Then, Schlichting calculated the growth rates, and showed they're quite small which suggested the importance of viscosity to boundary layer instabilities [16, 17]. Next, Squire showed that, for modal growth, the 3D disturbance problem can be reduced to that of an equivalent 2D problem at lower Reynolds numbers [18]. As such, this split the problem into two parts for the onset of instability, a laminar stability problem associated with 2D waves, and a turbulent fluctuation stability problem associated with 3D waves. Subsequently, this led to linear and nonlinear stability analysis, which wasn't experimentally verified until Schubauer and Skramstad found these 2D waves, which later were called Tollmien-Schlichting (TS) waves, and Klebanoff et al., who showed that as TS waves grow in amplitude, they begin to exhibit 3D or spanwise behavior [16]. As disturbance amplitude increases, and after the spanwise (3D) wave form develops, Lambda (Λ) vortices form, which in turn breakdown into turbulent spots. These turbulent spots are locations of isolated turbulence pockets. These spots may re-laminarize, or continue to grow in size and number. When the number of spots grow large enough to overlap and coalesce, the boundary layer becomes fully turbulent. Figure 2.1 below illustrates this process, along with showing the locations of Re_{cr} and Re_{tr} where transition/breakdown begins [12].

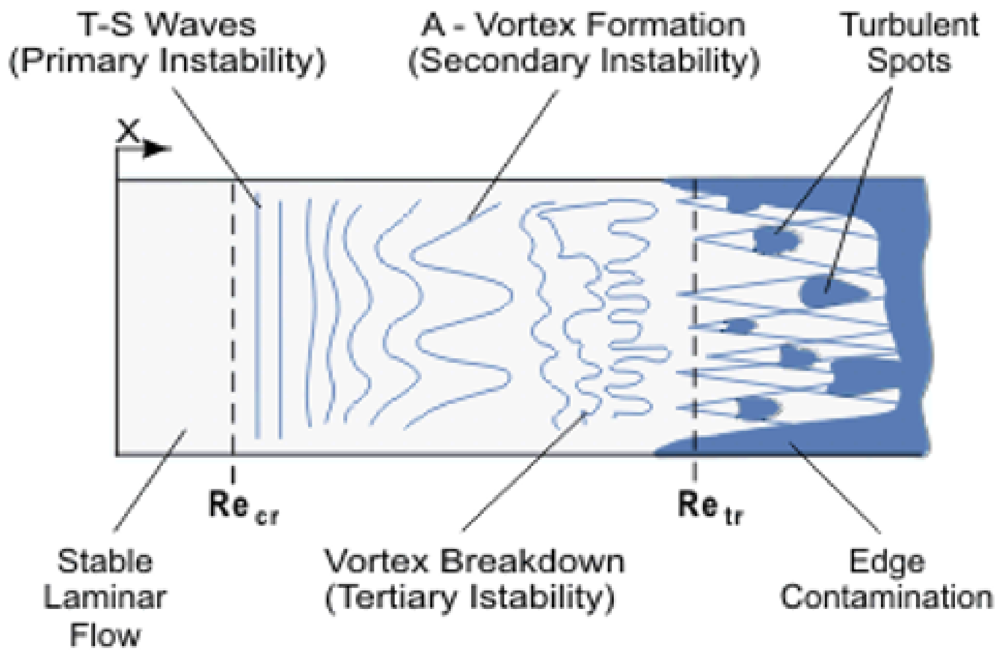

Figure 2.1: Laminar to turbulent boundary layer transition diagram [12].

2.3 Literature Review

2.3.1 High-Speed Flow Transition Theory

The stability and transition scenario described in the section 2.3 provides a good theoretical explanation for the transition phenomena based on low speed flows experience. At higher-speed, this "modal stability theory" scenario is commonly incorporated today. The modal growth scenario for hypersonic flows, starts with small disturbances, in the form of acoustic waves, surface roughness, temperature perturbations, and/or pressure perturbations, that enter the boundary layer [15]. This process by which such disturbances are mapped into the boundary layer is called receptivity. Once introduced into the boundary layer, these small amplitude disturbances grow linearly. As growth continues, the disturbances undergo nonlinear interactions including: harmonic generation, nonlinear modulation, saturation, and secondary instabilities, which eventually breakdown into turbulent spots. Lastly, the spots coalesce into fully turbulent flow [12, 15, 7]. Note that from experimental data and numerical calculations, it will be shown these disturbances are often identified as wavepackets and not pure harmonics. This transition scenario is illustrated in path A of Figure 2.2 below by Reshotko [15]. This figure illustrates an important point about the transition problem: there are multiple paths/processes by which a boundary layer may transition to turbulence. The modal growth pathway is just one of them, though arguably the most prevalent. Also, interactions among these paths are not fully understood. Active research areas, such as transient growth, rely on the non-orthogonality of disturbance modes which opens the possibility for interactions between paths [15].

2.3.1.1 Instability Mechanisms

In this section, various types of instability mechanics will be reviewed to give the reader an overview of some of the common instability mechanisms in a hypersonic flow. The two most commonly studied instabilities in high speed flow are the first and second Mack modes [6, 19]. These instabilities exist for two dimensional flows, but may exhibit three dimensional structure. Generically, the form of the disturbances can be represented by a shape function (ϕ) and a wave part, where (n,k) correspond to the type of mode (disturbance) considered.

$$\phi' = \phi(y)e^{i(\alpha x + k\beta z - n\omega t)} \tag{2.1}$$

$$\phi' = \phi(y)e^{i(\alpha x - n\omega t)} \mid \beta = 0 \tag{2.2}$$

$$\phi' = \phi(y)e^{i(\alpha x + k\beta z)} \mid n = 0 \tag{2.3}$$

$$\phi' = \phi(y)e^{i(\alpha x)} \mid \beta = 0, n = 0 \tag{2.4}$$

Representations 2.1 through 2.4 are variations of the wave form from section 2.3. Representation 2.1 corresponds to a 3D oblique mode instability. The disturbance is oblique in that it travels in an oblique angle relative to the flow direction. This models a first-mode instability, which is believed to be the high-speed extension of the viscous T-S wave [6]. At low speeds the T-S wave is 2D, but at high-speeds the wave become oblique. Representation 2.2 with $\beta = 0$, corresponds to a 2D instability mode.

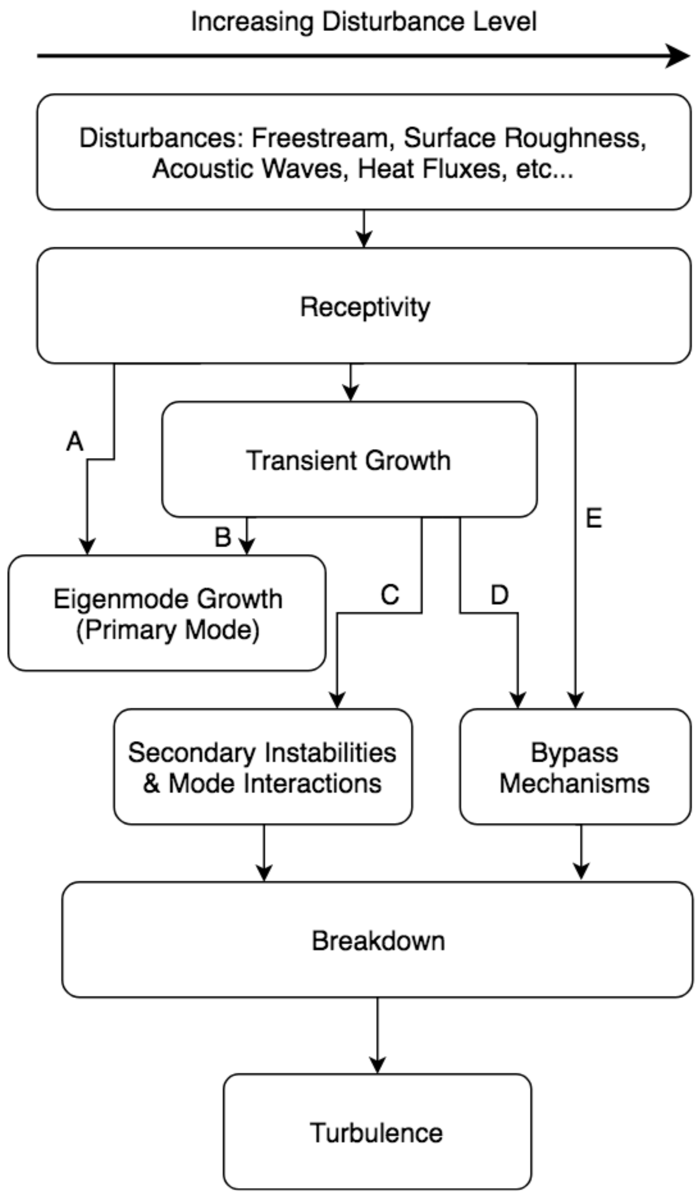

Figure 2.2: Modal stability theory, redrawn from Reshotko [15].

There is no more z-component to the wave, so it traverses only along the x direction. This models a second-mode instability, which is believed to be an inviscid, acoustic disturbance that dominates in hypersonic transition at Mach numbers greater than 4 [6]. Representation 2.3, corresponds to oblique steady disturbances which physically manifest as vortices. These vortical modes are used to model crossflow or Gortler instability [20, 21]. The flared cone is great for isolating the second-mode, but the concave geometry induces such Gortler modes [22]. These are counter rotating instabilities which are quite sensitive to surface roughnesses [22]. The last representation (2.4) corresponds to a steady streamwise-only growing disturbance. Physically, this models nonlinear modification to the basic flow states and is referred to as the mean flow distortion (MFD) [23]. The MFD is the mechanism by which the perturbed flow feeds back onto the mean flow [22, 24]. Figure 2.3 below depicts how energy flows between the various boundary layer disturbances and mean flow.

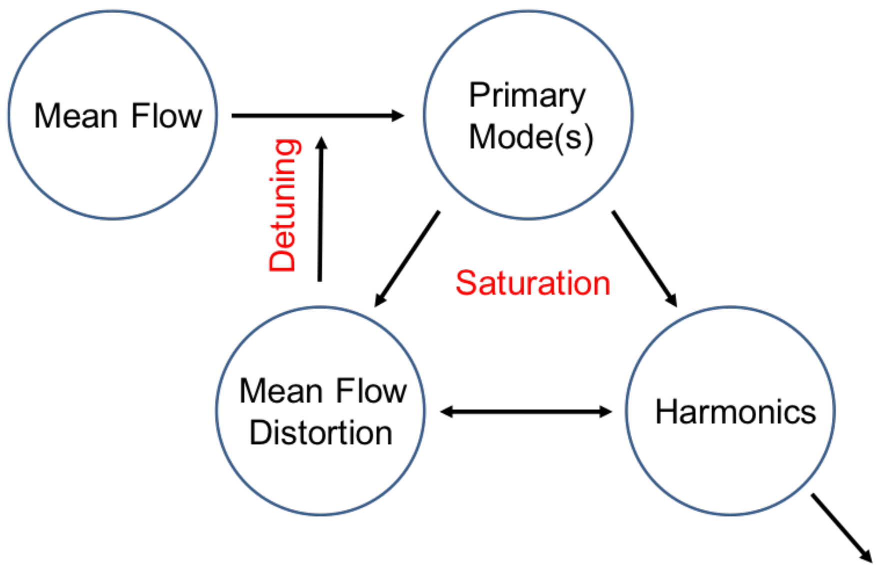

Figure 2.3: Energy flow chart including: energy saturation, primary feeds into harmonics, which feedback via mean flow distortion through nonlinear detuning [25].

As mentioned earlier, in supersonic and low hypersonic flows ($1 < \mathrm{M} < 4$) the viscous first-mode dominates transition, whereas when $\mathrm{M} > 4$ the inviscid second-mode is the prevalent instability at work [6, 19]. Further, there are interesting differences between first and second mode behaviors. One important difference occurs when heating the wall beneath a first-mode amplifies it, while cooling dampens it. Whereas, a second-mode behaves in the opposite manner, heating dampens it and cooling amplifies it [19]. This behavior for second-modes is exploited as a novel control mechanism, and discussed in chapter 8.

Additionally, nonlinear interactions can occur resulting in different stability and transition mechanisms than with second-modes alone. For instance, a (1,0) mode interacts with a (0,1) mode producing a (1,1) oblique mode [26]. Another interaction occurs when first and second modes can interact roughly in the range of Mach 4 through Mach 5. Instead of the normal case where only one mode dominates, both modes may be prevalent causing a different type of instability growth [6, 19].

2.3.1.2 Thermoacoustic Interpretation of Second-Mode Waves

Up to this point, various instabilities have been mentioned, but not how they propagate, or where their energy comes from. A recent contribution to second-mode instability theory, the thermoacoutic interpretation was provided by Kuehl (2018) [8]. The theory posits that second-modes behave as standing waves which are resonant in a thermoacoustic impedance well formed between the wall and the maximum density gradient in the boundary layer. Figure 2.4 depicts phases of the second-mode oscillation within the impedance well by plotting the: velocity variation, pressure variation, and acoustic impedance in the wall normal direction [8].

It is seen that the second-mode behaves as a quarter-wavelength standing wave which oscillates between the wall and the maximum density gradient. The maximum density gradient is approximately at the same location as the sonic line and turning point mentioned above. This wave form is then advected downstream as it oscillates within the well [8]. Outside the impedance well (relative sonic line, turning point) the oscillatory motion of the wave changes to exponential decay [8]. The impedance well size is related to the boundary layer height, although as the former is primarily thermal and the latter is primarily inertial, they are not necessarily the same height, which was shown by Koican, Hofferth, Saric, Oliviero, Perez, Kuehl, and Reed [27, 28]. Further, Kuehl showed that second-mode resonance is driven by thermoacoustic Reynolds stress. That is, second-mode waves derive their energy from the base flow through a

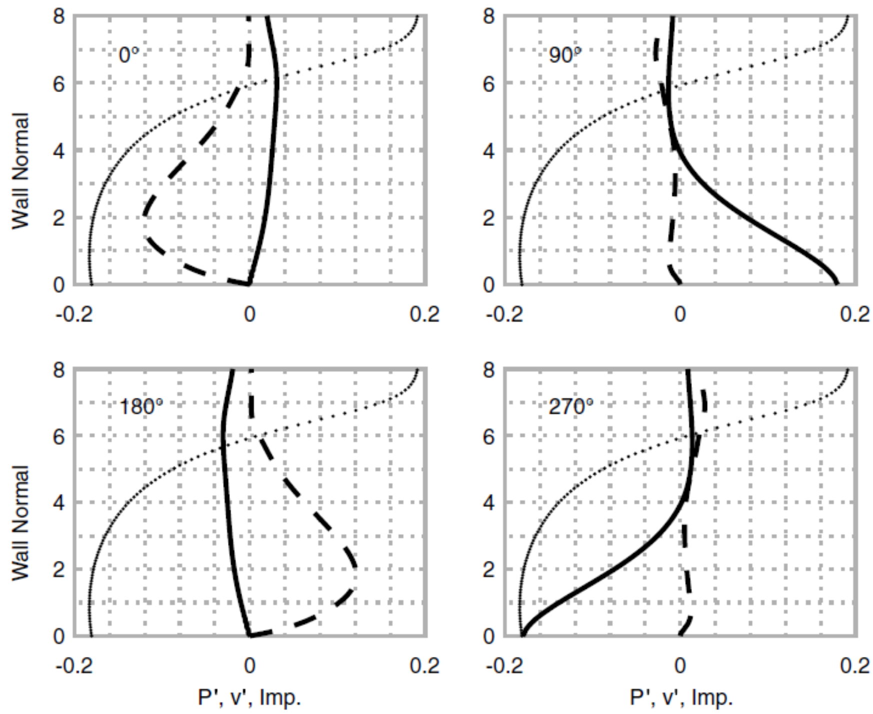

Figure 2.4: Second-mode oscillation phases in the wall normal vs velocity variation (dashed line), pressure variation (solid line), and acoustic impedance (dotted line) [8].

combination thermodynamic work and the divergence of acoustic power [8], which is manifest as thermoacoustic Reynolds stress in the inviscid Navier-Stokes equations and the acoustic energy equation:

$$\frac{D\rho}{Dt} = -\rho\nabla\cdot\mathbf{u} \tag{2.5}$$

$$\rho\frac{D\mathbf{u}}{Dt} = -\nabla p \tag{2.6}$$

$$\rho\frac{DT}{Dt} - \frac{1}{c_p}\frac{DP}{Dt} = 0 \tag{2.7}$$

$$\frac{D\left\langle e\right\rangle}{Dt} - \left[\left\langle \frac{d}{dy}(\bar{\rho}T'v')\right\rangle + \left\langle \frac{d}{dy}(\bar{T}\rho'v')\right\rangle\right] = 0 \tag{2.8}$$

$$\left\langle e\right\rangle = \frac{1}{2}\rho_e\left\langle u'^2\right\rangle + \frac{1}{2\rho_e a^2}\left\langle p'^2\right\rangle \tag{2.9}$$

Equations 2.5-2.7 combine to produce the cycle-averaged, 1D thermoacoustic energy

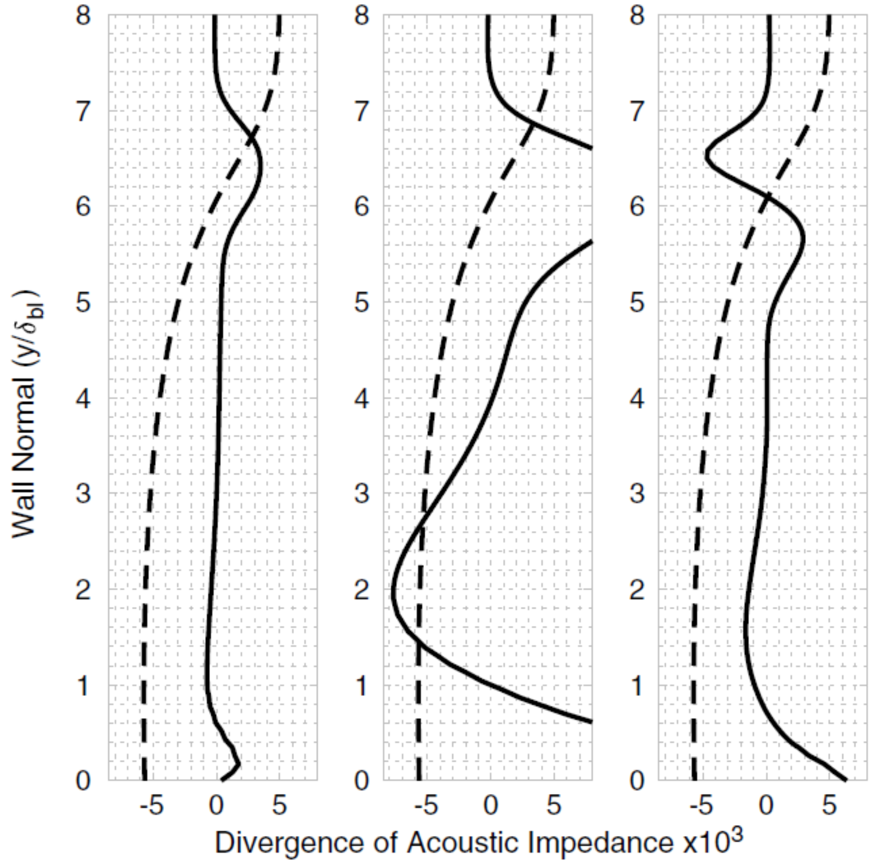

Figure 2.5: Wall normal y/δ_{bl} vs divergence of acoustic impedance plot [8].

equations (2.8), where energy is defined in 2.9. If the thermoacoustic Reynolds stress terms are less than 0, then the disturbances will be amplified in that region [8]. LST was computed, and shows that the unstable 285 kHz disturbance was amplified and had a negative Reynolds stress [8]. Whereas the neutrally-stable disturbances, 235 and 345 kHz, have diminished Reyonlds stress (refer to figure 2.5 where each plot from left to right is 235 kHz, 285 kHz, and 345 kHz) [8]. This represents the driving energy source which sustains second-mode growth. Thus second-mode waves behave as forced thermoacoustic resonators causing the fluid parcels to oscillate at a specific frequency within the impedance well [8]. Additionally, fluid parcels get a net increase in internal energy from pressure work during each oscillation [8], which appears to be a means of energy redistribution within the boundary layer. It is worth mentioning that a complete energy closure, accounting for viscous dissipation, has yet to be conducted [8]. The implications and applications of this new theory are addressed in this dissertation.

2.3.1.3 The Blunt Body Paradox

One of the many interesting open questions concerning hypersonic boundary layer transition is the so-called "blunt body paradox." That is, in second-mode dominated transitional boundary layers (such as blunt straight cones), the laminar-to-turbulent transition is delayed with increasing nose bluntness. However, there exists a critical nose bluntness at which the transition front will jump forward (upstream). The cause of this "upstream jump" is unknown and is referred to as the "blunt body paradox" [29]. Much effort has focused on resolution of this paradox, with the bulk of the work revolving around the so-called transient growth mechanisms, i.e. non-modal instability [30, 31].

Reshotko and Tumin (2000) laid much of the theoretical groundwork for non-modal stability, transient growth as a potential mechanism for the blunt body paradox [29]. At it most fundamental level, transient growth results from the non-orthogonal nature of boundary layer disturbances. For example, T-S waves and Squire modes can exchange energy resulting in algebraic growth, before eventual exponential decay. Transient growth is particularly sensitive to surface roughness, which appears to be the primary source of receptivity in many instances [29]. Particularly interesting is that the authors state that transition in this case usually occur in the subsonic region behind the bow shock where stable T-S waves with a favorable pressure gradient have been found [29].

While these dynamics have been well documented both numerically and experimentally (Marineau et al. 2014, 2015) the underlying physical mechanisms remain elusive (for both transition delay and upstream jump) [32, 33]. The computational study of Tufts and Kimmel (2017) verified the hypothesis of Juliano et al. (2015) that the delay in transition (downstream movement of the transition front) is associated with the suppression of second-mode growth and not associated with larger transitional N-factors [34, 35]. Tufts and Kimmel also documented the relationship between the entropy layer swallowing length (Stetson 1983) and second-mode growth suppression [36]. Meaning, second-mode growth was found to be suppressed within the entropy layer (upstream of the entropy layer swallowing length) while outside of the entropy layer (downstream of entropy layer swallowing length) second-mode growth was found to be unaffected by the bluntness. Thus, it seems obvious that second-mode growth suppression is caused by entropy layer modifications to the boundary layer. However, the physical mechanism by which such suppression occurs is not yet fully understood, and is related to one of the research objectives in this dissertation.

2.3.2 Experimental Methods of High-Speed Instability Phenomena

The majority of experimental methods for testing hypersonic boundary layers are flight and wind-tunnel tests. Flight tests by nature are expensive, provide limited data, and are non-trivial to perform, but when successful provide the most useful data of hypersonic boundary layers behavior. This is because atmospheric conditions are very quiet, meaning the boundary layer's stability is not adversely affected by noise from the environment [37]. However, noise can be radiated from other parts of the vehicle such as the engine(s) which can contaminate the test.

For hypersonic wind tunnel experiments, there are important characteristics in order to study hypersonic flows including pros and cons. The major tradeoff of high-speed wind tunnels compared to flight tests are much more data can be generated, with more options for high quality data. The difficulty though, particularly with hypersonic flows is it is very difficult to re-produce the same conditions during flight [37, 38]. Before the advent of quiet tunnels, noise was one of the major factors which contaminated or even tripped the boundary layer in ground tests. Quiet tunnels are not easy to build as they must be designed to not just study, but also control transition [38]. Consider, if the boundary layer on the tunnel wall is turbulent, then a substantial noise would radiate off the walls, contaminating the test. This and many other design factors are important in quiet tunnel design and operation, and is an active area of research [37, 38].

2.3.2.1 Purdue Boeing/AFOSR Mach-6 Quiet Tunnel (BAM6QT)

As of the writing of this dissertation, some of the quiet hypersonic tunnels are: Purdue Boeing/AFOSR Mach-6 Quiet Tunnel (BAM6QT), Texas A&M's Mach 6 Quiet Tunnel, and the recently built AFOSR-Notre Dame Large Mach 6 Quiet Tunnel. The BAM6QT is primarily focused on in this dissertation since tests conducted in it were compared to in this research. The Purdue Boeing/AFOSR Mach-6 Quiet Tunnel (BAM6QT) is a quiet hypersonic wind tunnel with a 2.590 meter long nozzle which allows for thick boundary layers to form along the wall which are less affected by ambient noise [39]. The tunnel is a Ludwieg design with a convergent-divergent nozzle, vacuum tank on the most downstream end, and an air pressurized driver tube on the upstream end. A double diaphragm is broken to initiate flow from the driver tube towards the vacuum tank, see figure 2.6 for details [11, 39].

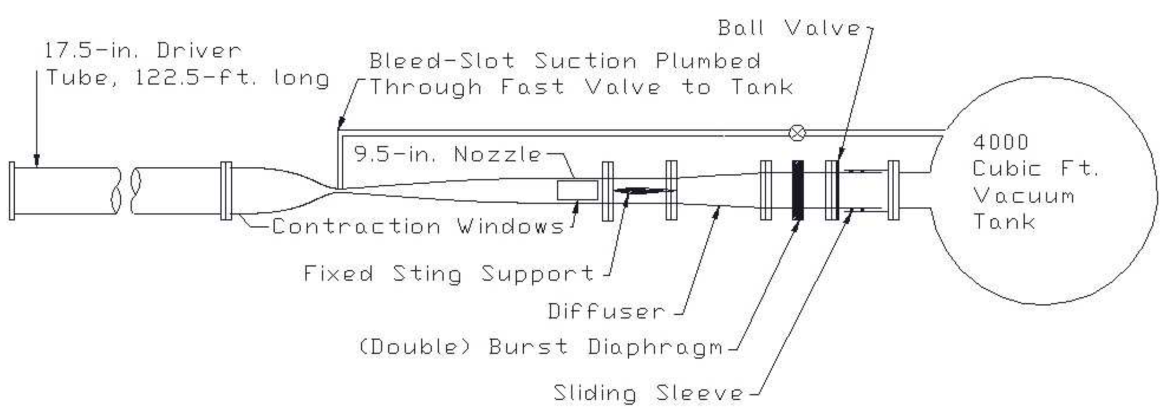

Figure 2.6: Purdue Boeing/AFOSR Mach-6 Quiet Tunnel (BAM6QT) Diagram (used with permission) [11].

The experimental second-mode instability work of Casper et al. provides a reasonable starting point and motivation for a rigorous treatment of finite-bandwidth (wavepacket) effects [39]. Casper et al. summarized two types of tests to experimentally study wavepackets and generate turbulent spots: naturally occurring and controlled disturbances. The naturally occurring disturbances, which formed into viably measured turbulent spots, were observed to propagate as wavepackets along the nozzle wall [39]. However, in this case it wasn't feasible to track the origin and development of the disturbance into a turbulent spot due to its small initial amplitude, hence the need for a controlled disturbance initiation. The controlled disturbances were generated from a pulsed-glow perturbations created by an electrode which produced an electric discharge similar to that of a car spark plug. After the disturbances were created, they were observed to travel as wavepackets downstream, where the pressure transducers were used to measure the surface pressure fluctuations on the nozzle wall, near the region of the turbulent spot formations [39]. Three unit Reynolds number (Re) ranges were tested: $6.3-6.4\times10^6, 8.25-8.4\times10^6$, and $10.6-10.8\times10^6$ m^{-1}.

The flow conditions for the natural disturbance case were: $Re = 10.6-10.8\times10^6$ m^{-1}, $P_0 = 1031$ kPa, and $T_0 = 415.9$ K. In the streamwise direction, several pressure fluctuation measurements along with the determined power spectral density (PSD) were made on the nozzle wall of a wavepacket breaking down into a turbulent spot between 2.201 m and 2.831 m [39]. Measurements were also taken in the spanwise direction at 2.679 m. They also calculated ensemble-averaged disturbances along the streamwise, centerline of the pressure, and power spectral densities (PSD) for each Reynolds number tested [39]. After the disturbance generation, the wavepacket grows linearly in amplitude as it travels downstream. Once it reaches a certain streamwise distance: 2.679 m at $Re = 6.33\times10^6$ m^{-1}, 2.480 m at $Re = 8.25\times10^6$ m^{-1}, and between 2.378 m and 2.480 m at $Re = 10.8\times10^6$ m^{-1}, the wavepacket becomes nonlinear, indicated by the appearance of a 1st harmonic (twice the frequency of the primary mode) in the PSD data [39]. These nonlinear waves interact with each other, forcing more harmonics, and an overall increase in the wavepacket's amplitude. Finally, the wavepacket breaks down to a turbulent spot. Notice, in the $Re = 8.25\times10^6$ m^{-1} case at 2.781 m, the broadband amplitude of the disturbance in the PSD results. The overall trend with increasing Re, is that the wavepacket growth and breakdown to turbulence moves upstream. This summary sheds a little more light into the modal growth scenario by considering a wavepacket's evolution from the linear to the nonlinear.

An example of the aforementioned wavepacket behavior can be considered by measurements made along the 2.5 inch nose radius slender cone tested in the BAM6QT by Dr. Brandon Chynoweth [11]. Specifically, the results under quiet tunnel conditions by Chynoweth in figure 2.7 help to identify the weak, moderate, and strong nonlinear regimes of the wavepacket on its way to turbulence transition. This can be seen in the figure by identifying the number of peaks and amplitude growth. The first peak at 91.6 cm between 110 and 120 kHz represents the primary disturbance undergoing mostly linear growth since the harmonics are still small. Further downstream, the second peak at roughly 220 kHz is the first harmonic. The shift from 91.6 to 99.3 cm shows the beginning of growth of the first harmonic and very small amount of growth for the second harmonic (roughly 330 kHz). If one focuses at 114.5 cm downstream, there are more harmonics and much larger amplitudes for the primary and harmonics showing very strong nonlinear growth potentially leading into breakdown. Next, figure 2.8 shows the test results under noisy tunnel conditions for very strong nonlinearities, then, a short breakdown period potentially with turbulent spots between 101 and 112 cm, finally followed by the broadband spectrum of the disturbance at 114.5 cm downstream.

Casper et al. also performed spanwise measurements and created contour plots between 2.679 and 2.831 meters downstream for the varied Re cases [39]. They showed the positive and negative pressure fluctuations with the evolution of the wavepacket from nonlinear waves to breakdown to the arrowhead shaped turbulent spot. An interesting result is that this wavepacket first breaks down in the center and then spreads in the spanwise direction, and at hypersonic velocities, the wavepacket continues to travel along with the turbulent spot [39]. The measured pressure drops show the second-mode waves present just ahead and trailing the turbulent spot at $Re = 8.4 \times 10^6$ m^{-1}, forming a calmed pressure region [39]. This phenomenon shows that a sudden demarcation of breakdown and transition does not occur, and implies a more apt description could be

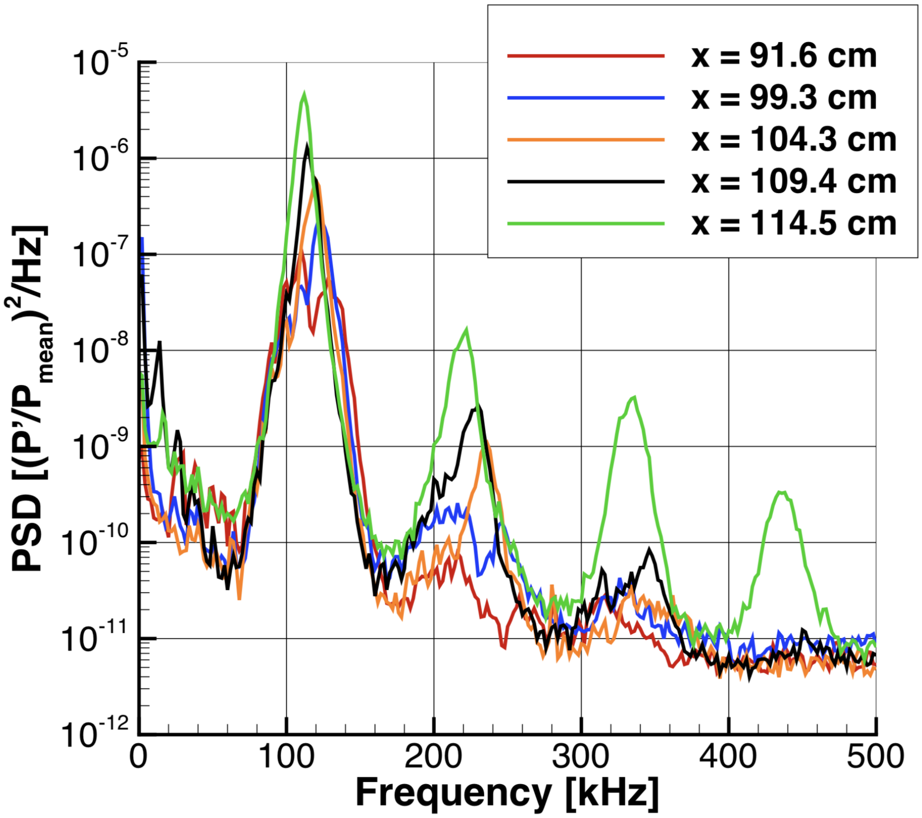

Figure 2.7: Power spectral density (PSD) showing growth, nonlinearities/harmonics, with increased harmonics amplitude likely approaching breakdown to turbulence at quiet tunnel conditions on 2.5 degrees half-angle slender cone, $Re = 9.5 \times 10^6$ m^{-1} (used with permission) [11].

analogous to a kinetic range of energy transfer marching towards an equilibrium state.

2.3.2.2 Purdue Flared Cone

The subsequent experiments conducted in BAM6QT are similar in nature, but included a test article. Various geometries were been tested, but the main geometry considered in this report is the Purdue flared (compression) roughness insert cone [10, 11] (figure 2.9. The benefit of using a flared cone is to create a more consistent boundary layer height. Since the boundary layer δ(x) grows with downstream distance, the flare of the cone counteracts boundary layer growth, resulting in a nearly constant

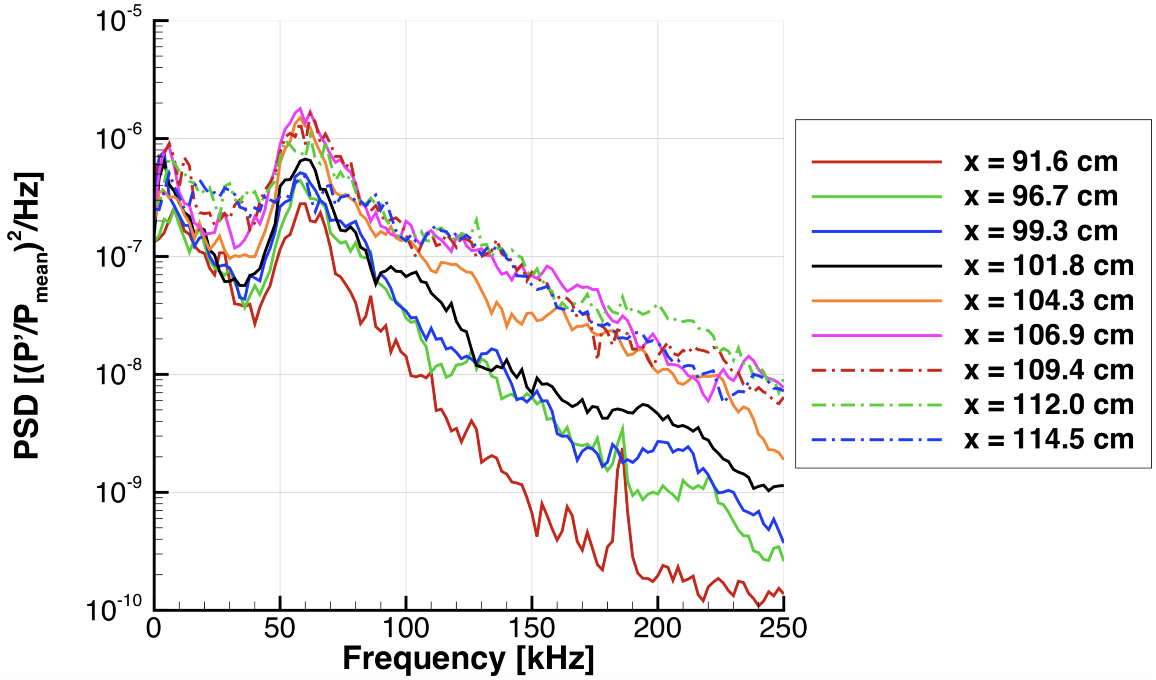

Figure 2.8: Power spectral density (PSD) showing growth, nonlinearities/harmonics, with increased harmonics amplitude likely approaching breakdown to turbulence at noisy tunnel conditions on 2.5 degrees half-angle slender cone, $Re = 1.8 \times 10^6$ m^{-1} (used with permission) [11].

boundary layer along the length of the cone. As the most unstable second-mode frequency is tied to boundary layer height, this allows for the amplification of a particular frequency second-mode along the entire length of the cone. This allow for the study of natural transitions studies, without the need to force disturbance initiation [10, 11]. Additionally, this simplifies the calculations for the basic state and disturbance evolution. The dimensions and features of the cone are as follows [10, 11]. The cone is composed of three parts: nosetip, roughness insert ring, and frustrum. The nosetip is the front-most part measuring 25.4 cm long, and has an initial, opening half angle of 1.5 degrees. The roughness insert area comes next, and is 0.635 cm long where smooth or rough rings can swapped to initiate disturbances from discrete roughness elements. The aft-most part is the frustrum, measuring 25.654 cm long. This brings the total length of the cone to 51.69 cm, with a base half radius of 5.715 cm wide, and a flare radius of 3 meters (curved arc portion of the cone wall).

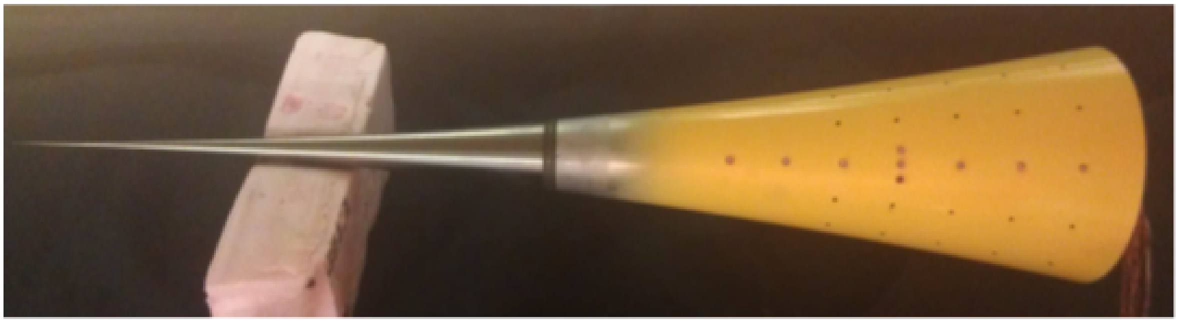

Figure 2.9: Purdue flared roughness insert cone (used with permission) [10, 11].

The research group at Purdue have extensively characterized this geometry at Mach 6 condition using temperature sensitive paint (TSP) and PCB pressure sensors to collect data for disturbance growth and evolution [10, 11, 40, 41]. Below are examples of a TSP image and a power spectral density (PSD) measurements on the flared cone. This data was collected from a run at the following tunnel conditions: $Re = 9.2 \times 10^6 m^{-1}$, $P_{0,i} = 130.1 psia$, $T_{0,i} = 161.7 psia$, $P_0 = 121.3 psia$, $x = 44 cm$. The TSP image shows a hot-cold-hot streak pattern generated by temperature modulations of the disturbance waves flowing over the cone [10]. The PSD figure shows the root-mean-square (RMS) pressure change versus the spectrum of the disturbances at 6 downstream distances [10]. The first peak in the graph is the primary disturbance of the second Mack mode, and is at 300 kHz with the peak amplitude at 44.1 cm downstream. The next peak is the first harmonic, which is double the primary disturbance frequency at 600 kHz. The last peak frequency, triple the primary around 900 kHz is the second harmonic. Same as the tunnel wall tests, the harmonics show nonlinear behavior of the disturbance. Comparing the PSD plot to the TSP image, it can be seen that disturbance amplitude grows, then decays which is consistent with the estimated heat transfer rates as measured from the temperatures in the TSP image [10]. These experimental result serve as the benchmark against which the numerical investigation of chapter 4 will be compared.

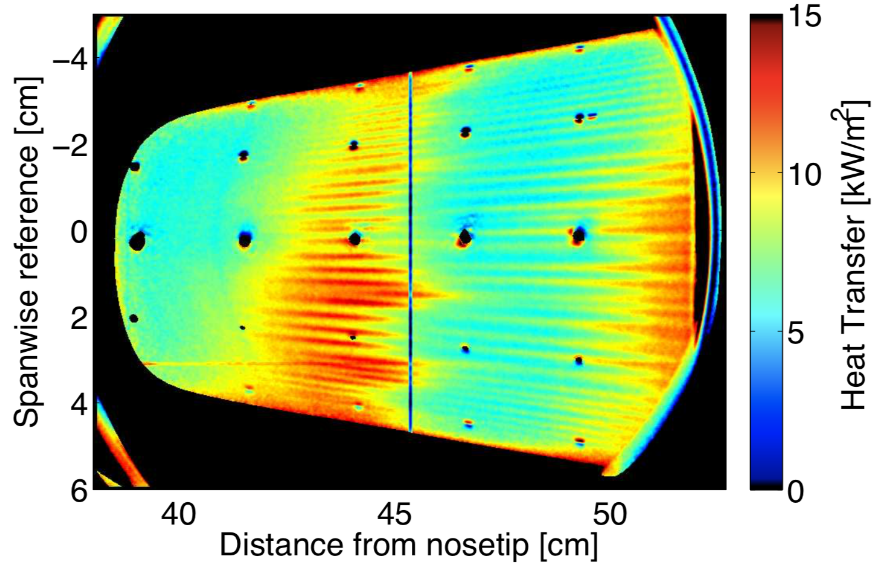

Figure 2.10: Purdue flared roughness insert cone TSP image showing hot-cold-hot streak temperature pattern (used with permission) [10].

2.3.3 Computational Modeling of High-Speed Instability Phenomena

2.3.3.1 JoKHeR Overview

The JoHKeR Parabolized Stability Equations (PSE) package was developed by Kuehl 2012 in collaboration with Dr. Helen Reed at Texas A&M as part of the efforts of the National Center for Hypersonic Laminar-Turbulent Transition Research [9, 25]. The program employs a Quasi-3D, compressible, ideal gas, primitive variable formulation; that is, it marches disturbances along a predefined path with the assumption of uniformity in the perpendicular direction. The package consists of Linear Stability Theory (LST), Linear Parabolized Stability Equations (LPSE) and Nonlinear Parabolized Stability Equations (NPSE) solvers. These stability solvers have been extensively validated against experimental, and numerical datasets [22, 25, 27, 28, 42, 43, 44, 45]. A unique feature of JoHKeR is that it employs a nonlinear wavepacket formulation for NPSE implementation which allows for the modeling of finite bandwidth disturbances, and thus accounts for spectral broadening and low-frequency content generation which is important for accurate prediction of nonlinear energy exchange [7, 24, 25, 46]. The

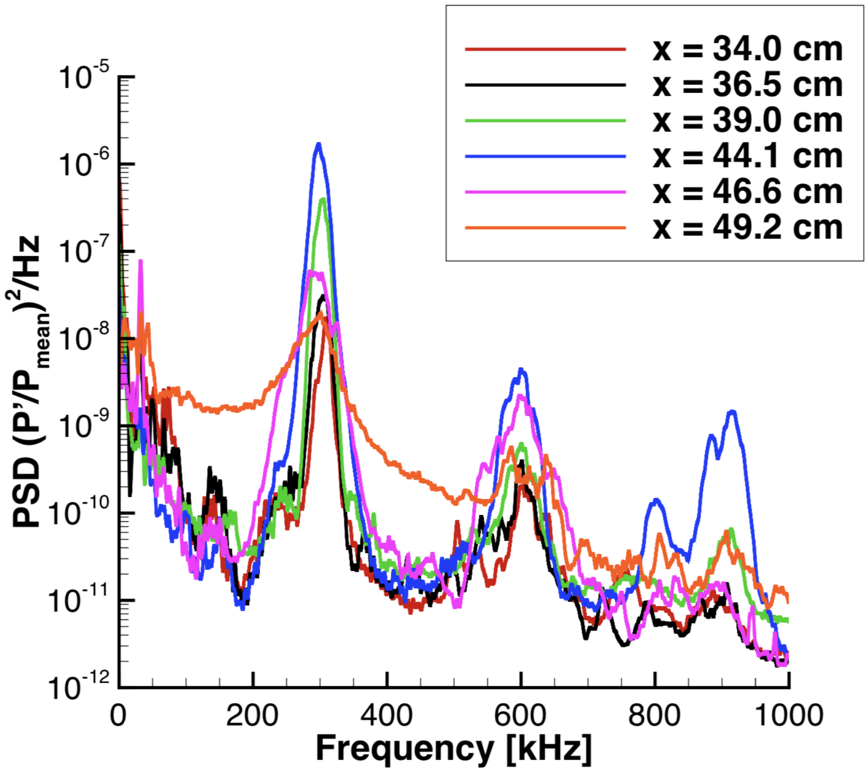

Figure 2.11: Purdue flared roughness insert cone PSD data (used with permission) [10].

next several sections describe JoKHeR in more detail.

2.3.3.2 Linear Stability Theory

Linear stability theory (LST) considers a steady basic flow state, determined from separate CFD simulations, and solves the disturbance equation (which follows from substitution of equation 2.10 into the Navier-Stokes equations) assuming linear, parallel flow. The disturbance is assumed to be of the form indicated by equation 2.11, substitution of which into the disturbance equations leads to the generalized eigenvalue problem with α and ω being the streamwise wave number and the frequency respectively. The resulting eigenvalues are used to determine instability and the corresponding eigenvector represent the shape of the disturbance in the wall normal direction.

$$\phi(x,y,z,t) = \underbrace{\bar{\phi}(y)}_{basic\,state} + \underbrace{\phi'(x,y,z,t)}_{disturbance} \tag{2.10}$$

$$\phi' = \hat{\phi}(y)e^{i(\alpha x+\beta z-\omega t)} \tag{2.11}$$

2.3.3.3 Parabolized Stability Equations

Originally identified by Herbert and Bertolotti (1987), during a critical review of Gaster's (1974) early nonparallel work, the parabolized stability equations have been developed as an efficient and powerful tool for studying the stability of advection-dominated laminar flows [47, 48]. Excellent introductions to the PSE method and summary of its early development were provided by Herbert (1994,1997) [16, 49]. During the early stages of both linear and nonlinear development of this technique, much was established related to basic marching procedures, curvature, normalization conditions, and numerical stability of the method itself (Bertolotti 1991; Chang et al. 1991, Joslin et al. 1992, Li and Malik 1996, and Haynes and Reed 2000) [50, 51, 52, 53, 54].

In a relatively short time, the field rapidly expanded to include complex geometries, compressible flow, and finite-rate thermodynamics (Stuckert and Reed 1994, Chang et al. 1997, Johnson et al. 1998, Haynes and Reed 2000, Malik 2003, Chang 2004, Johnson and Candler 2005, Li et al. 2010, Theofilis 2011, Paredes et al. 2011, Kuehl et al. 2012, Kocian et al. 2013, and Perez et al. 2012) [9, 28, 54, 55, 56, 57, 58, 59, 60, 61, 62, 63, 64].

PSE is similar to the Fourier/Laplace transform in that it considers an initial-value problem. However, the slowly varying basic state assumption is made in the streamwise direction and a slow variable $\bar{x} = \frac{x}{Re}$ is introduced. Ultimately, disturbances are assumed of the form

$$F[\phi'] = \underbrace{\tilde{\phi}(\bar{x},y)}_{\text{shape}}\underbrace{\Phi(x,t)}_{\text{wave}}$$

where the wave part satisfies

$$\frac{\partial \Phi}{\partial x} = i\alpha(\bar{x})\Phi \tag{2.12}$$

$$\frac{\partial \Phi}{\partial t} = -i\omega\Phi, \tag{2.13}$$

where $Re = \frac{U_e \delta_r}{\nu_e}$ is a Reynolds number based on characteristic values of edge velocity (U_e), edge kinematic viscosity (ν_e), and reference boundary-layer length scale (δ_r). Thus, PSE considers disturbances of the form

$$\phi' = \int_{-\infty}^{\infty} \underbrace{\tilde{\phi}(\bar{x}, y, \omega)}_{\text{shape}} \underbrace{A(\bar{x}, \omega)e^{-i\omega t}}_{\text{wave}} d\omega \tag{2.14}$$

where $A(\bar{x}, \omega) = e^{i\int \alpha(\bar{x},\omega)dx}$ and the dependence of the shape function ($\tilde{\phi}$) and amplitude function (A) on ω has been made explicit. The shape and amplitude functions are essentially the Fourier transform of the disturbance. Upon expansion of the streamwise derivatives

$$\frac{\partial \phi'}{\partial x} = \int_{-\infty}^{\infty} \left(\frac{1}{Re}\frac{\partial \tilde{\phi}}{\partial \bar{x}} + i\alpha\tilde{\phi} \right) Ae^{-i\omega t} d\omega$$

$$\frac{\partial^2 \phi'}{\partial x^2} = \int_{-\infty}^{\infty} \left(\frac{1}{Re^2}\frac{\partial^2 \tilde{\phi}}{\partial \bar{x}^2} + \frac{2i\alpha}{Re}\frac{\partial \tilde{\phi}}{\partial \bar{x}} + \frac{i\tilde{\phi}}{Re}\frac{\partial \alpha}{\partial \bar{x}} - \alpha^2\tilde{\phi} \right) Ae^{-i\omega t} d\omega,$$

it is found that the second spatial derivative $\frac{\partial^2 \tilde{\phi}}{\partial \bar{x}^2}$ is of highest order and a perturbation expansion may be consistently truncated resulting in the neglect of this term. This leaves the disturbance equation nearly parabolized, and an efficient marching solution may be sought [53].

JoKHeR implements a wavepacket formulation (Kuehl 2017) which appears to better represent energy transfer between modes in a nonlinear calculation [7]. Ultimately, in the Quasi-3D formulation, the disturbance is discretely represented as $\phi' = \sum_k \tilde{\phi}(\bar{x}, y)_k A(\bar{x})_k W(\omega)_k e^{-i\omega_k t}$, and a frequency content for each mode is assumed of the form $W_0 = \frac{1}{\sigma_0\sqrt{2\pi}} e^{-\frac{(\omega-\omega_0)^2}{2\sigma_0^2}}$. With bandwidth of the harmonics obeying

$\sigma_i = \sqrt{i+1}\sigma_0$, and harmonic balancing is used to calculate nonlinear interactions. This representation of spectral energy appears to be crucial for modeling the spectral broadening seen in experiments. Details of this are provided in the next section.

2.3.3.4 Nonlinear PSE (NPSE) - Traditional vs Wavepacket

The recently developed, nonlinear PSE (NPSE) wavepacket formulation extends the PSE methodology to properly account the experimentally observed wavepacket's nonlinear dynamics [7]. Equation 2.15 represents how nonlinear interactions (the right hand side) force the linear disturbances (left hand side). In spectral space, nonlinear interactions are represented as the convolution of the Fourier transforms of the individual disturbance modes. The weight functions W_1 and W_2 contain the spectral information and thus are central to modeling nonlinear disturbance interactions [7].

$$\int_{-\infty}^{\infty} \tilde{\phi}_0 A_0 W_0 e^{-i\omega t} d\omega \leftrightarrow \tilde{\phi}_1 \tilde{\phi}_2 A_1 A_2 \int_{-\infty}^{\infty} (W_1 \star W_2) e^{-i\omega t} d\omega \tag{2.15}$$

The traditional PSE formulation inherently assumes pure harmonics and thus the weighting function take the form of delta function.

$$W_0 = \delta(\omega - \omega_0), \tag{2.16}$$

$$(W_1 \star W_2) = \delta(\omega - (\omega_1 + \omega_2)) \tag{2.17}$$

Plugging this into equation 2.15 yields:

$$\tilde{\phi}_0 A_0 W_0 e^{-i\omega_0 t} \leftrightarrow \tilde{\phi}_1 \tilde{\phi}_2 A_1 A_2 e^{-i(\omega_1+\omega_2)t}. \tag{2.18}$$

This yields a harmonic balancing condition ($\omega_0 = \omega_1 + \omega_2$) which is important to keep the time and frequency related terms in the exponential from averaging to 0 [7]. To model wavepackets (ie. disturbances with finite bandwidths), a Gaussian weight function is defined instead:

$$W_0 = S_0 e^{-\frac{(\omega-\omega_0)^2}{2\sigma_0^2}}, \tag{2.19}$$

$$(W_1 \star W_2) = S_{1,2} e^{-\frac{(\omega-(\omega_1+\omega_2))^2}{2(\sigma_1^2+\sigma_2^2)}}. \tag{2.20}$$

Where: $S_0 = \frac{1}{\sqrt{2\pi\sigma_0^2}}$ and $S_{1,2} = \frac{1}{\sqrt{2\pi(\sigma_1^2+\sigma_2^2)}}$ are the nonlinear coupling coefficients. When these new weight functions are substituted into equation 2.15 producing,

$$\tilde{\phi}_0 A_0 S_0 e^{-i\omega_0 t} \int_{-\infty}^{\infty} e^{-\frac{(\delta\omega)^2}{2\sigma_0^2}} e^{-i\delta\omega t} d(\delta\omega) \leftrightarrow \tilde{\phi}_1 A_1 \tilde{\phi}_2 A_2 S_{1,2} e^{-i(\omega_1+\omega_2)t} \int_{-\infty}^{\infty} e^{-\frac{(\delta\omega)^2}{2(\sigma_1^2+\sigma_2^2)}} e^{-i\delta\omega t} d(\delta\omega). \tag{2.21}$$

an additional requirement to the harmonic balancing condition is found. A bandwidth condition appears which captures the energy transfer between the modes denoted by $\sigma_0^2 = \sigma_1^2 + \sigma_2^2$ [7]. Consider figure 2.11 which again consists of pressure sensor data from a hypersonic flow experiment, it is trivial to see a finite bandwidth treatment more closely represents these disturbances than a pure harmonic delta function.

This finite nature of the disturbance is exactly what the wavepacket formulation seeks to capture. When the primary disturbance is convolved with itself, a wider, Gaussian disturbance, is produced; the first harmonic. When this first harmonic is fed back onto the primary disturbance, some of the energy is projected back into the primary disturbance, while some is projected onto the side lobes. This is the nonlinear mechanism responsible for so-called spectral broadening, a widening of the spectrum as at the onset of nonlinearity. Figure 2.12 is an illustration of this overall process, and figure 2.13 shows the details of the convolution.

2.3.3.5 Wavepacket PSE Results on the Purdue Flared Cone

Comparisons between the discrete versus Gaussian NPSE formulations for second-modes are shown in figures 2.14 and 2.15 [7]. A steady state, Mach 6 solution for flow around the Purdue flared cone, corresponding to a $Re = 10.283 \times 10^6$ m^{-1} as similarly tested by Chynoweth (2015) in the BAM6QT, was generated in the CFD solver GASP [41]. The NPSE calculations were initialized with LST eigenmodes at 285 kHz for the

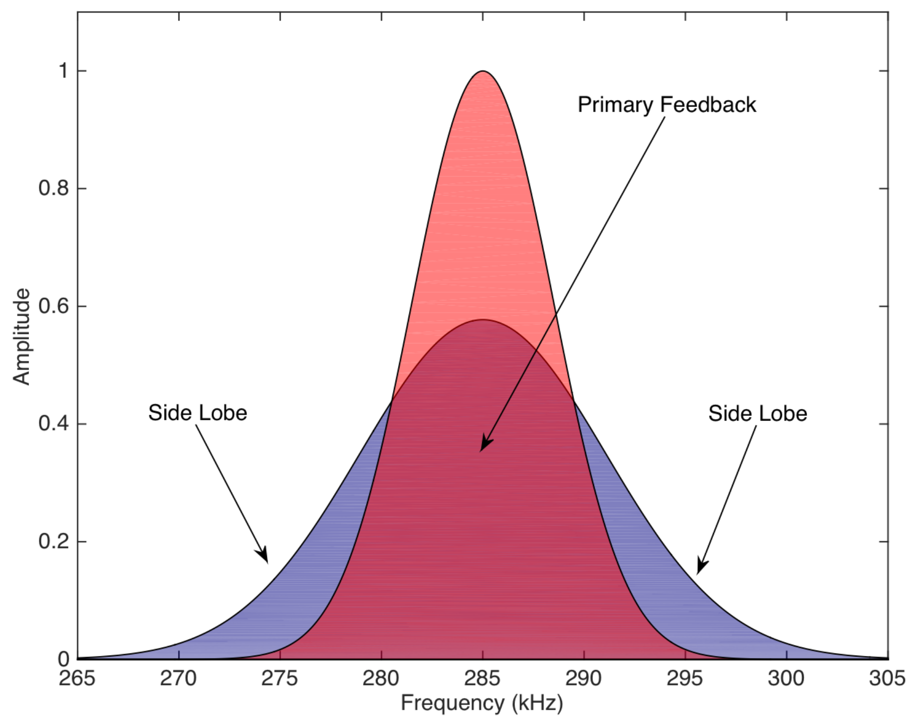

Figure 2.12: Primary disturbance graphic with side lobes and nonlinear feedback [7].

primary disturbance, and side-lobes at 265 and 305 kHz. The cone's geometry and flow conditions were: length = 0.49 m, base diameter = 0.11684 m, nose radius = 0.001 m, radius of curvature = 3 m, AoA = 0 Freestream: $M = 6$, $T_\infty = 52.8$ K, $P_\infty = 610.775$ Pa, $Re = 10.283 \times 10^6$ m^{-1}, Isothermal wall boundary condition: $T_{wall} = 300$ K.

In figure 2.14 Kuehl showed the comparisons of discrete versus wavepacket NPSE formulation. All three plots show root mean square of the disturbance amplitudes versus the streamwise distance. Further, the top plot is a discrete mode at 285 kHz, and compares nonlinear saturation to the linear results. The middle plot considers 3 discrete modes at 285 kHz (primary mode), 265 and 305 kHz (side lobe modes) which all grow and nonlinearly saturate, but there is no spectral broadening. This is as expected because the delta function does not capture the transfer of energy among modes. The bottom plot shows the results for the wavepacket formulation for the same 3 modes. This time, there is a higher saturation amplitude of the primary mode, and

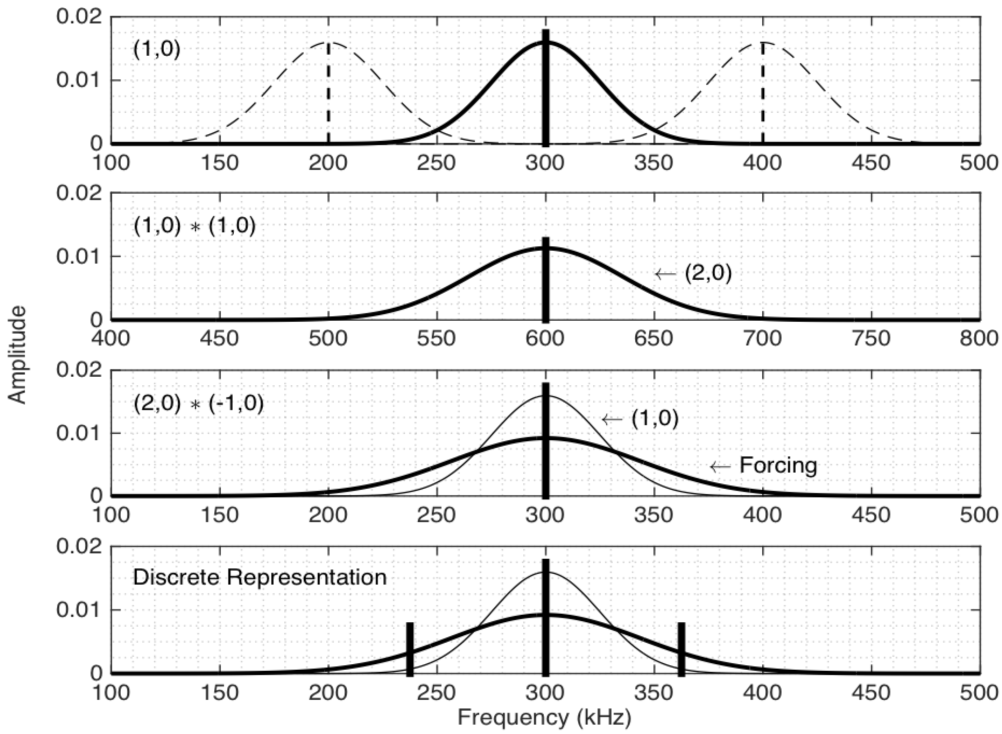

Figure 2.13: Convolution example of primary disturbance, nonlinear feedback onto side lobes, and corresponding to spectral broadening [7, 65].

significant growth of the side lobe frequencies. This is spectral broadening. Next, in figure 2.15 a comparison of the discrete and wavepackets formulations disturbance velocity and pressure amplitudes and experiments were performed. The results showed two important findings: first that the wavepacket formulation more accurately captures nonlinear energy, and second, the wavepacket formulation improves upon amplitude prediction when compared with experimental data.

Benefits of the Parabolized Stability Equations (PSE) include a lower computational cost as compared to direct numerical simulations (DNS), the ability to isolate and probe specific physical mechanisms of the flow and the technique is broadly applicable (low-speed aerodynamic designs, swept wings, pipe flows, geophysical flows, jet wakes, etc.) An excellent review of the PSE method is provided by Herbert [16].

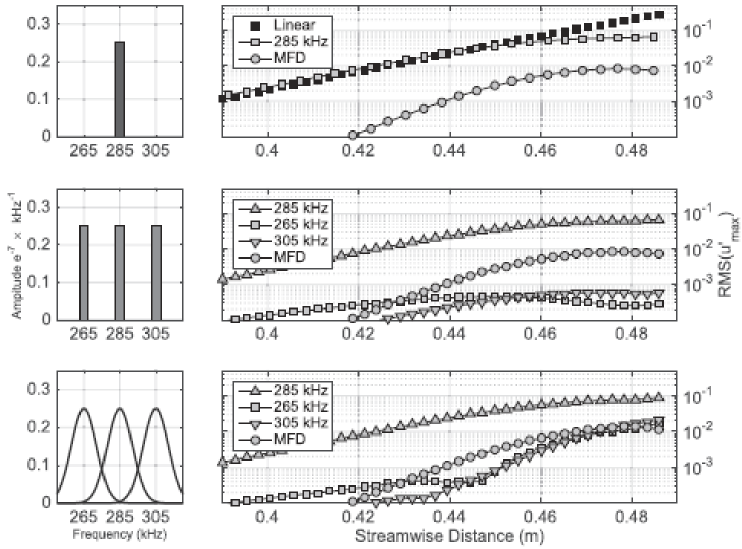

Figure 2.14: Comparison results of the NPSE run on Purdue flared cone at M = 6. The root mean square of the disturbance amplitude vs the streamwise distance. The top plot is the single mode case, the middle is the 3 mode delta function case, and the bottom is the 3 mode wavepacket case [7].

2.3.3.6 DNS

Direct numerical simulation (DNS) can provide accurate solutions to the N-S equations assuming good convergence. However, the computational cost can be high, convergence is not trivial for complex geometries, and the physical mechanisms of transition can be obscured [16]. DNS does provide much insight into the experimental results of transition, and a good numerical benchmark. DNS is usually employed by requiring very fine computational meshes in a two pass solution scheme [26]. The first pass is the laminar, undisturbed, steady state solution (basic state). The second step takes as an input the basic state, then performs a higher order stability and transition solution generation. To disturb the basic state, blowing or suction is usually imposed at an upstream location on the geometry. Then the higher order, compressible Navier-Stokes equations are solved [26]. The DNS results for the disturbance evolution are then compared against experimental or other numerical results for verifications/validation.

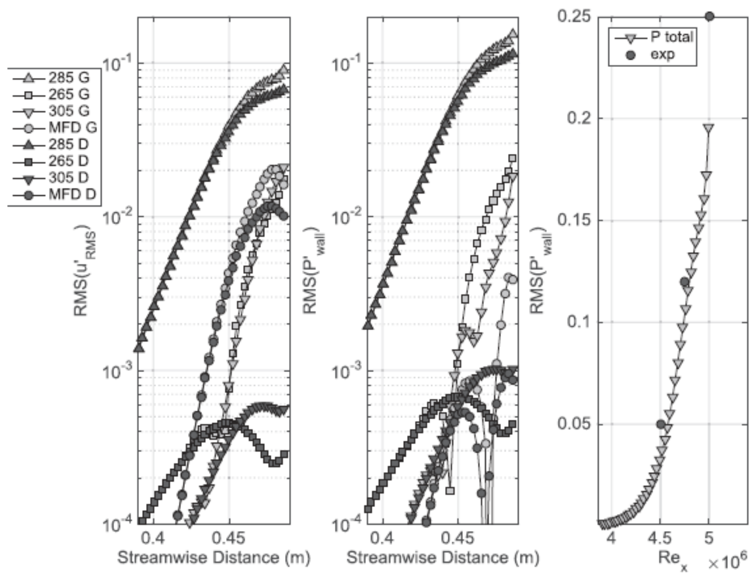

Figure 2.15: Comparison results of the NPSE run on Purdue flared cone at $M = 6$. Left: The root mean square (RMS) of the disturbance velocity vs the streamwise distance comparing Gaussian and delta functions. Middle: RMS disturbance pressure vs the streamwise distance comparing Gaussian and delta functions. Right: RMS disturbance pressure vs Reynolds number comparing Gaussian NPSE and experimental results [7].

Chapter 3

METHODOLOGY

3.1 Overview

Computational stability analysis of fluid flow around a geometry is generically broken into 6 steps:

1. Geometry
2. Meshing
3. Solving
4. Visualization
5. Data Extraction
6. Analysis.

First, the desired geometry is created in a computer aided design (CAD) program. Second, this geometry is imported into a gridding / meshing software package. Third, the grid / mesh is imported into the computational fluid dynamics (CFD) software package, (US3D is used in this research) and a basic state solution is generated. Fourth, the basic state solution is visualized for initial validation. Fifth, pertinent data is extracted from the basic state solution and more carefully validated. At this point, the typical CFD process is essentially complete. For example, one could take this solution and use it to create a test plan for a preliminary vehicle design. In this dissertation, the sixth and final step is to import the basic state solution into a numerical stability program (linear stability theory, parabolized stability equations, or direct numerical simulation). This step also indirectly validates the basic state solution [44], and produces the stability analysis results which can then be compared to the theory, experimental data, flight data, and even other numerical stability results. The following sections will show an example case of the aforementioned numerical analysis methodology.

3.2 CFD Basic State Generation Process

3.2.1 Geometry

Solidworks is used to create the CAD models for the geometries to be tested. Figures 3.1 and 3.2 show the Purdue flared roughness insert cone half body at two different stages of the modeling. The dimensions are the same as mentioned in chapter 2, with an initial half angle of 1.5 degrees, the total length is 516.89mm, the half base is 57.15mm, and the nose-tip radius is 0.15mm [10]. The flared curvature of the cone has a reference radius of 3m.

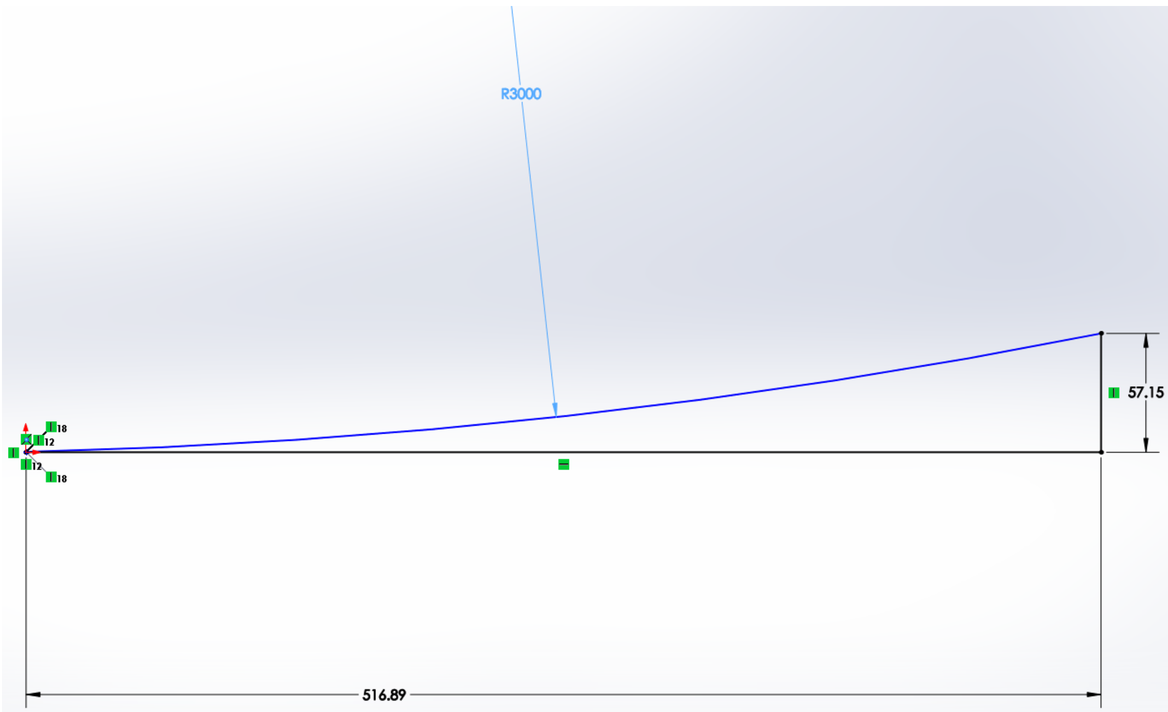

Figure 3.1: Solidworks CAD model with dimensions shown

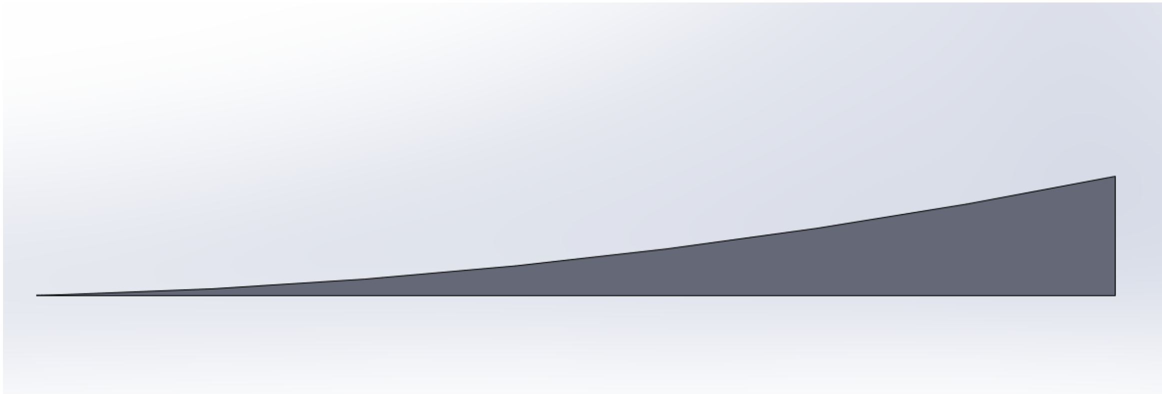

Figure 3.2: Solidworks CAD model final

3.2.2 Meshing

To create the computational domain (grid or mesh), the gridding / meshing software Pointwise is used. The Solidworks model is imported into Pointwise, where grid points are applied along the top edge, starting from the leading edge of the nose, to the trailing edge at the end of the cone. Then, quadrilateral points are extruded normal to the wall, a sufficiently high amount in order to create the 2D computational domain. In our case "sufficiently high" means outside the shock into the undisturbed free-stream. This required estimating the shock angle and the height above the wall of the cone, and is done using the θ-β-Mach diagram. At Mach 6, for a nominally sharp nosed, streamlined body, a weak oblique shock would form. We follow the path for the average angle of the cone to get the angle of the shock. Then estimate the height of the shock, add some additional grid points beyond our estimate shock location for computational padding. One does not want to go too high above the shock as this is computationally wasteful, but too low and the shock will not be captured within the computational domain. To help keep the grid point count lower, and to be more computationally efficient, the normal extrusion has a higher fidelity (much larger number of grid points) close to the wall, and a growth rate is added so the number of grid points become sparser with each layer above the wall. This is easily seen in the figure 3.4 where the grid resolution is so fine near the wall, that one cannot even see the individual points, but close to the top boundary, the grid is distinguishable. Boundary layer stability calculations require extremely well resolved boundary layers, so it is common to cluster 150 or more grid points within the wall normal direction of the boundary layer. Such grid clustering not only saves memory, but also on the shear number of calculations required for each cell, greatly reducing computational time. Again, it is important to remember that sparse grids can provide basic state solutions that "look good", but closer inspection to determine if the necessary physical processes are properly resolved is always necessary.

After the normal extrusion process is complete, the next step is to extrude rotationally since this is a cone. Since the experiments performed on this cone were nominally at an angle of attack (AoA) of 0 degrees, we do not need to create the entire cone computational domain in the azimuthal direction (ie. 360 degrees of rotation around the cone). A one degree "slice", axisymmetric domain rotational extrusion in the azimuthal direction is sufficient, with appropriately set boundary conditions. This simplification saves orders of magnitude of extraneous grid points. Looking at an iso view in figure 3.5, it can be seen the mesh has been rotationally extruded in the azimuthal direction by 1 degree creating a 3D domain not a 2D plane.

Now that the mesh has been made, the boundary conditions can be specified. This specification happens twice, once with the mesh, and again within the solver. Figure 3.5 illustrates the boundary condition and their locations. We set the "inflow" where flow enters the domain and the freestream flow conditions such as velocity, temperature, and density will be specified. The inflow runs from the leading edge of the nose, all the way up to the very top of the domain. "Outflow" is set where the flow leaves the domain. "Wall" condition is set where the no slip condition is imposed at the body's surface(s). The last boundary condition for this case is to set "symmetry" conditions on both of the two length-wise sides of the domain.

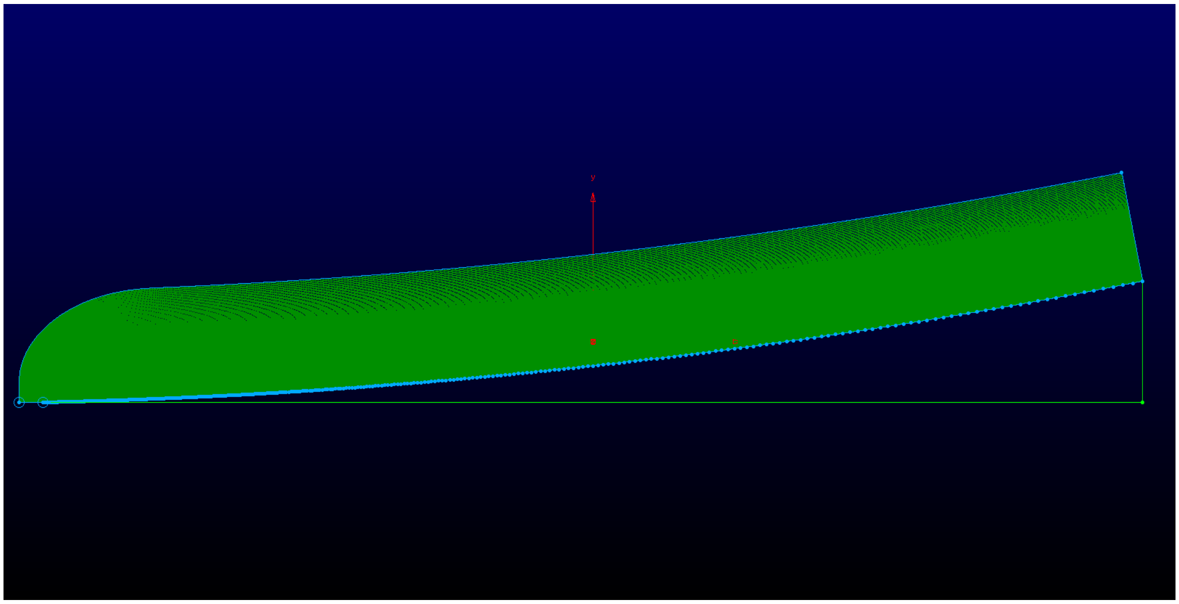

Figure 3.3: Pointwise mesh: 1.25 million quadrilateral grid points

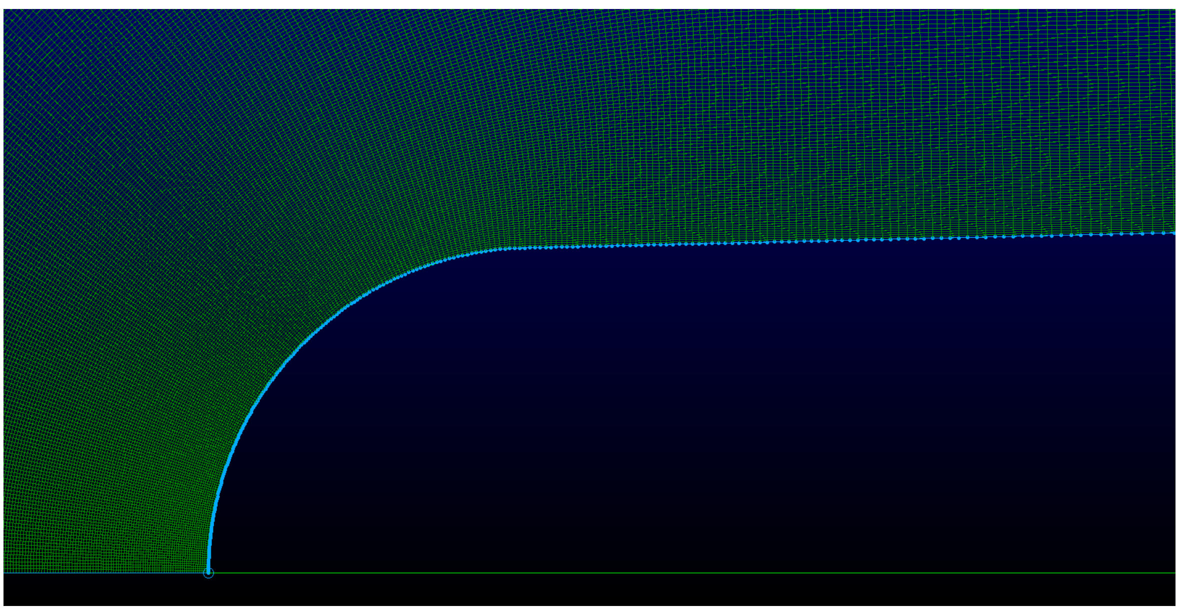

Figure 3.4: Zoom in of mesh at nose tip

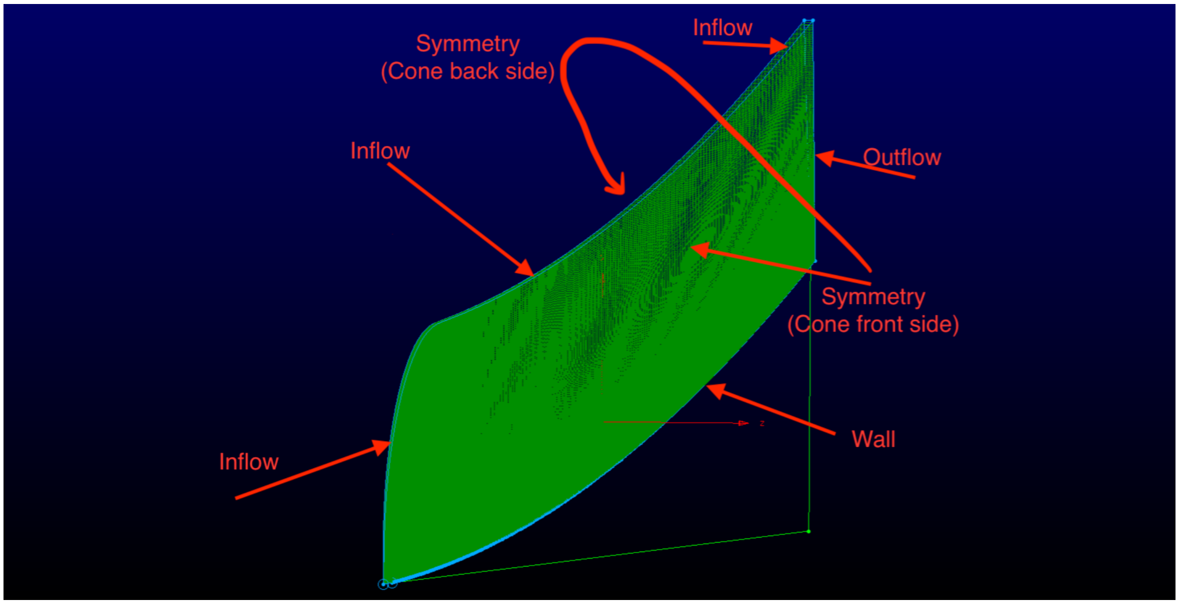

Figure 3.5: Iso view of mesh

3.2.3 Solving

US3D is a CFD software package specifically designed for high-speed flows [66, 67, 68]. Many general purpose CFD packages already exist and provide great first order approximations, however, such packages tend to either struggle at hypersonic flow conditions through excessive numerical viscosity, neglected physical aspects of hypersonic flows, or insufficiently robust convergence schemes. US3D uses the finite volume method (FVM) to calculate fluxes across cells [66, 67, 68]. This is different than the finite difference method which calculates the differences of the partial differential equations it is solving. The FVM performs numerical integration sharing more of a connection with its finite element analysis (FEA) roots and control volume analysis. Moreover, US3D incorporates high-order solving schemes, multiple viscosity and gas properties, and other physical aspects (chemical reacting multi-species gases, turbulence closure models, etc.) which help to create accurate solutions. US3D first pre-processes the mesh created in Pointwise. Then, the input deck which includes all of the fluid, flow, and numerical properties and settings for solver, must be prepared.

This includes such inputs as: gas species, boundary conditions, inviscid or viscous flow, freestream velocity, density, temperature, wall temperature, wall heat transfer method (ie. isothermal or adiabatic), and number of iterations. An example of free-stream input conditions, from the BAM6QT, are listed in tables 3.1 and 3.2.

Table 3.1: BAM6QT example experimental setup conditions [10].

$P_{0,i}$ [kPa]	$T_{0,i}$ [K]	P_0 [kPa]	$Re \times 10^6/m$	γ_{air}
8.9676	434.85	8.361	9.2	1.4

Table 3.2: Calculated US3D freestream and wall initial conditions calculated from tunnel conditions.

Run Case	Boundary	ρ [kg/m^3]	T [K]	u [m/s]
Base	Inflow	0.0355	51.9799	867.1092

At this unit Reynolds number, initial stagnation temperature and pressure, total pressure, and the fact that the tunnel operates at around Mach 6 for plain air, it is permissible to assume an ideal gas and use the isentropic chain, shown in equations 3.1 and 3.2, to calculate the freestream temperature [10]. Once the freestream temperature is determined, the freestream pressure and density are calculated from equation 3.1 and the ideal gas law: equation A.6. Lastly, the speed of sound for tunnel conditions can be calculated from equation A.15 which when used with the Mach number in equation A.14 produces the freestream velocity. These inflow conditions can now be inputted into the input deck.

$$\frac{P_0}{P} = \left(\frac{\rho_0}{\rho}\right)^{\gamma} = \left(\frac{T_0}{T}\right)^{\frac{\gamma}{\gamma-1}} \tag{3.1}$$

$$\frac{T_0}{T} = 1 + \frac{\gamma-1}{2}M^2 \tag{3.2}$$

The wall boundary conditions are usually either isothermal or adiabatic and an initial wall temperature is set. With these initial and boundary conditions set, the major aspects of the input deck are ready to run, an example excerpt is shown below.

```
[CFD_SOLVER]
!-----------------------------------------------------------------------
!   nstop      ires     nplot     iconr       impl      kmax    kmaxo
   600000         0      1000         0          1         4        4
!
!   ivisc      ivib     ichem      itrb      ibase    idiss_g
       13         0         0         0          0          1
!
!   ivmod     ikmod     idmod       ikv       icfl      dtfix
        2      -999         1         1          1     0.0d0
!
!  iorder      iuem      ikve       kbl       iman
        2         3         1        60        100
!
!   npfac     npvol
       0         0
!
!     cfl      epsj      wdis
   1.0d00       0.3  0.005d-2
!-----------------------------------------------------------------------
[/CFD_SOLVER]
[GAS_SPECIES]
Air
[/GAS_SPECIES]
[MANAGE]
!-----------------------------------------------------------------------
 4
 500   1.0d0
 700   2.5d0
1000   5.0d0
...
100100   5.0d0 20
101500   1.0d1 20
103000   5.0d1 20
140000   1.0d2 20
160000   2.5d2 20
180000   5.0d2 20
200000   1.0d3 20
```

```
220000  2.0d3 20
250000   1.0d3 24
275000   2.0d3 24
300000   1.0d3 24
!-------------------------------------------------------------------------
[/MANAGE]
[CFD_BCS]
!-------------------------------------------------------------------------
! Boundary condition section
! Mach 6.0
! zone    bcn    igrow   name       [parameters]  ...
! ----    ----   -----   --------   ------------
     4      7      0     "bottom"
     5     10      0     "inlet"    3.550d-2 51.9799d0 51.9799d0  867.1092
     6     36      0     "outlet"
     7      7      0     "top"
     8      3    400     "wall"      2       300.0d0
done
!
! Required mass fractions
! ----------------------
  "inlet"   1.000000
!
! Required direction cosines
! -------------------------
  "inlet"   1.000000 0.000000 0.000000
!
!-------------------------------------------------------------------------
[/CFD_BCS]
```

Once the input deck has been setup, the US3D solver is run for the set number of iterations. The goal is to get the solution to converge a quickly as possible, to the smallest level of residuals (numerical error) possible. There is not a rigorous convergence criteria for every flow, grid, and geometry, but the rule of thumb which gets passed by word of mouth is an error on the order of 10^{-4} is loosely converged, 10^{-5} is moderately converged, and 10^{-6} is strongly converged. Again, the determining factor for convergence depends on the application. With stability analysis, a converged solution is the solution for which stability results no longer change with refinement. Below is a snippet of the first and last 10 iterations of a solution run. The convergence variable columns in order are: iteration, residual, simulation time, timestep, and CFL number.

```
 iter residual time timestep CFL
      1   4.502457478E+07   1.423865887E-11   1.423865887E-11   1.000E+00
      2   4.495474168E+07   2.847613514E-11   1.423747627E-11   1.000E+00
      3   4.489408445E+07   4.271242906E-11   1.423629391E-11   1.000E+00
      4   4.483938367E+07   5.694754085E-11   1.423511179E-11   1.000E+00
      5   4.478930851E+07   7.118147077E-11   1.423392992E-11   1.000E+00
      6   4.474291898E+07   8.541421904E-11   1.423274828E-11   1.000E+00
      7   4.469960590E+07   9.964578592E-11   1.423156688E-11   1.000E+00
      8   4.465897250E+07   1.138761716E-10   1.423038572E-11   1.000E+00
      9   4.462069121E+07   1.281053764E-10   1.422920480E-11   1.000E+00
     10   4.458451945E+07   1.423334006E-10   1.422802412E-11   1.000E+00
...
 599990   2.199365007E-06   6.294345982E-03   1.260698179E-08   1.000E+03
 599991   2.194666894E-06   6.294358589E-03   1.260698179E-08   1.000E+03
 599992   2.208751332E-06   6.294371196E-03   1.260698179E-08   1.000E+03
 599993   2.234233412E-06   6.294383803E-03   1.260698179E-08   1.000E+03
 599994   2.237404708E-06   6.294396410E-03   1.260698179E-08   1.000E+03
 599995   2.241673047E-06   6.294409017E-03   1.260698179E-08   1.000E+03
 599996   2.234666960E-06   6.294421624E-03   1.260698179E-08   1.000E+03
 599997   2.210507348E-06   6.294434231E-03   1.260698179E-08   1.000E+03
 599998   2.206189000E-06   6.294446838E-03   1.260698179E-08   1.000E+03
 599999   2.211048990E-06   6.294459445E-03   1.260698179E-08   1.000E+03
 600000   2.198688019E-06   6.294472052E-03   1.260698179E-08   1.000E+03
```

The first 3 columns are apparent, so let us focus on the last two: timestep and CFL. The timestep is the Δt of the simulation. The CFL number or Courant-Friedrichs-Lewy condition number is defined by equation 3.3. The CFL number is a necessary condition for convergence, but not a sufficient one. Also, this is one of the main control knobs in US3D that affects the convergence rate, which also in turn controls the timestep. In general, a bigger CFL number speeds up the solver convergence rate, but can cause instability and even divergence if too large. Conversely, too low of a CFL dramatically extends the computational time required to converge the solution to a sufficiently low residual level.

$$CFL = \Delta t \sum_{i=0}^{n} \frac{\Delta V_i}{\Delta X_i} \tag{3.3}$$

Once the solution is converged, the solution is post-processed in US3D to extract and convert the desired flow data into a format which can be loaded into a visualization software such as Tecplot.

3.2.4 Visualization

3.2.4.1 Axisymmetric Case @ 0 AoA

The first qualify control applied to basic state solutions generated in US3D, is visualization. In this dissertation, Tecplot is used for visualization.

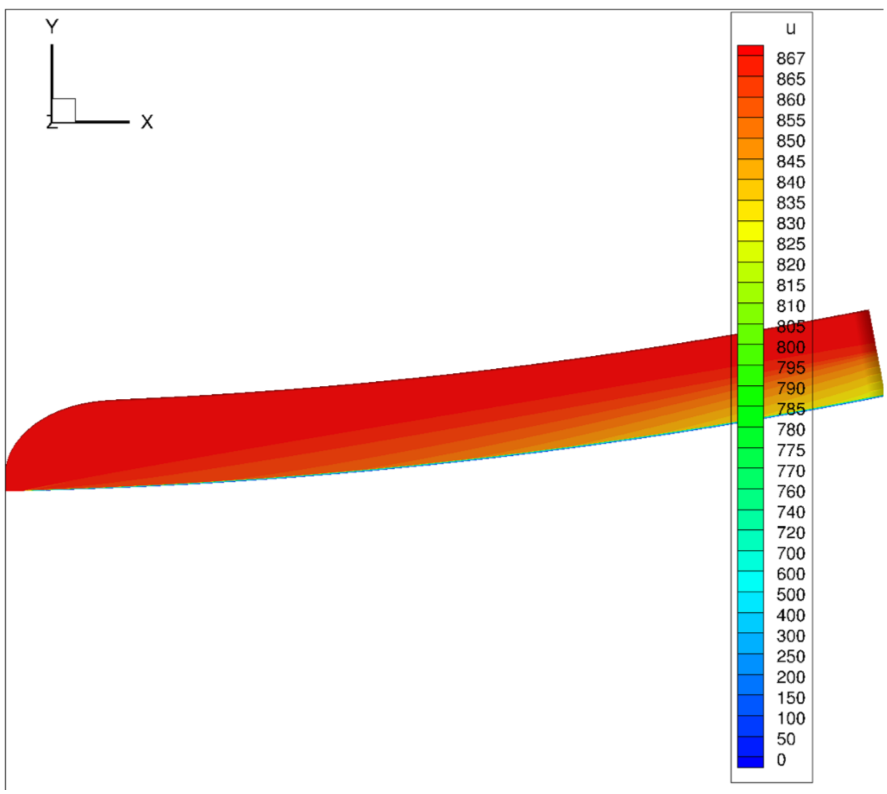

Figure 3.6: u velocity contour plot of Mach 6 Purdue flared cone.

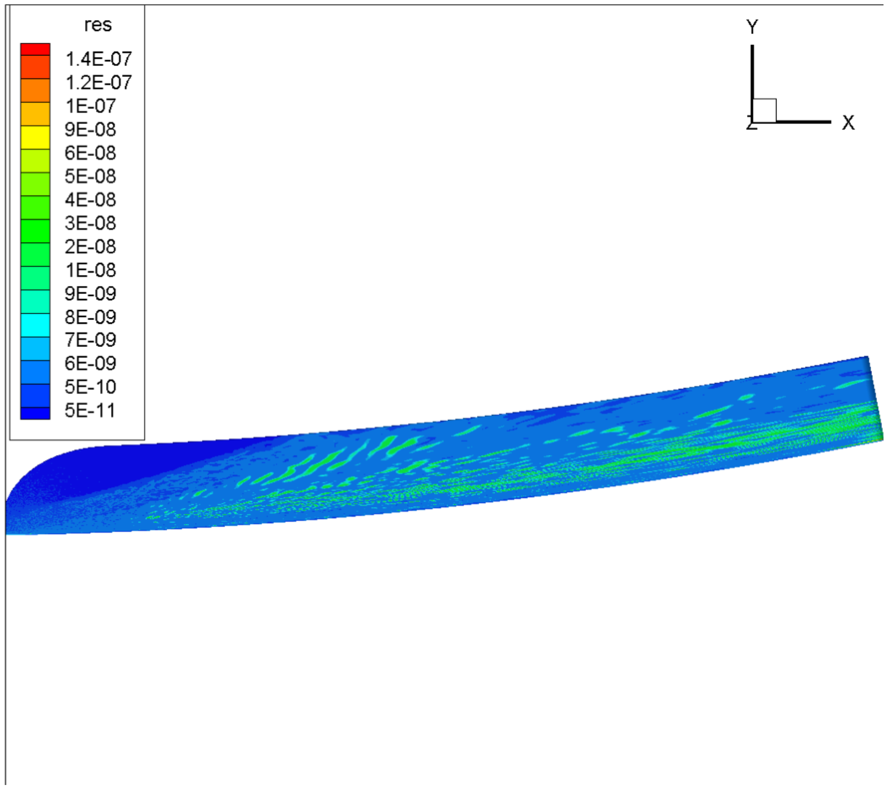

Figure 3.7: CFD Residuals contour plot of Mach 6 Purdue flared cone.

Figures 3.6 and 3.7 are results from the basic state calculations of the flared cone at Mach 6. Shown are contour plots of the flow velocity (u) in the x-direction and the spatial residuals or numerical error, respectively. From such visualization, errors in the basic state calculations can be identified and trouble shot. Here, the velocity field looks reasonable (grid captures shock, boundary layer resolved, no apparent discontinuities, etc.), and the spatial residuals are quite low (an order of magnitude less than or equal to 10^{-7}), which indicates a well converged solution.

The next 5 figures (3.8, 3.9, 3.10, 3.11, 3.12) show an example of a solution which is not physical/correct. This example was of a straight cone, 7 degree half angle at Mach 6. The Mach contour plot looks good, with a reasonable looking shock which is well developed and contained within the grid. The u velocity contour plot, upon first glance, also look fine. However, upon closer inspection, when zooming into the nose, the velocity does not look quite right. The problem is that the flow is reversed in front of the nose, which is indicative of an incorrect solution. When visualizing the spatial residuals, the order of magnitude is as high as 10^4 in front of the nose and within the entire shock region the resuduals are unacceptably large. This example illustrates that the visualization step is important during the CFD process, and at this point, it would be necessary to troubleshoot the solver conditions and possibly the grid, then re-run the solver. In this particular case, the grid was carefully analyzed, and was found to insufficiently resolve the nose region. This is because an insufficient amount and inadequate spacing of wall normal points was specified in the mesh.

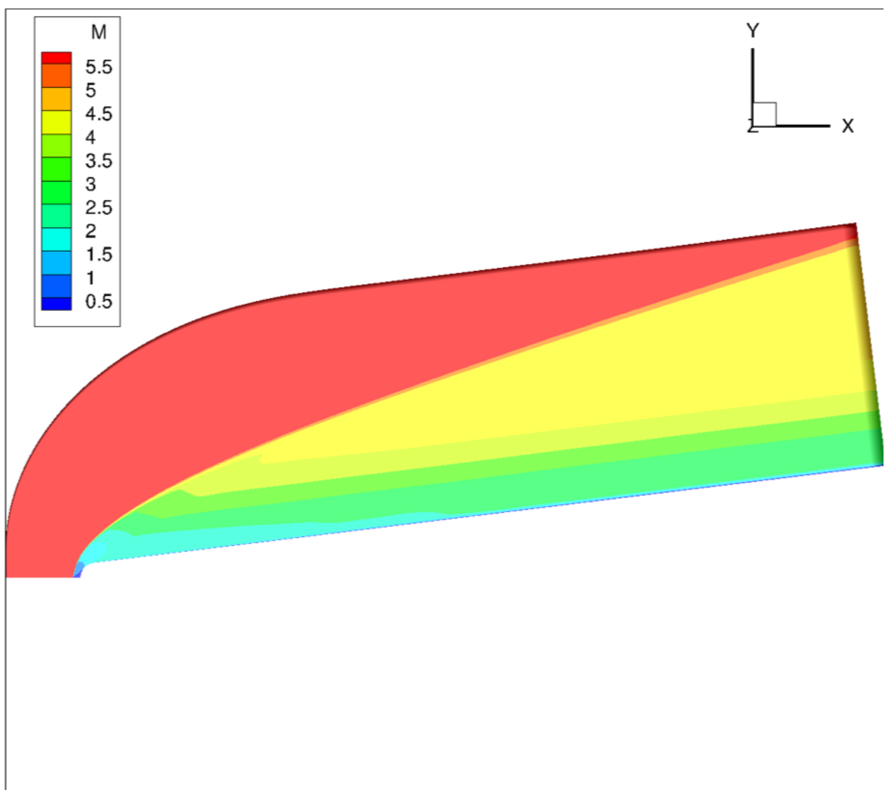

Figure 3.8: Mach number contour plot of straight cone at Mach 6.

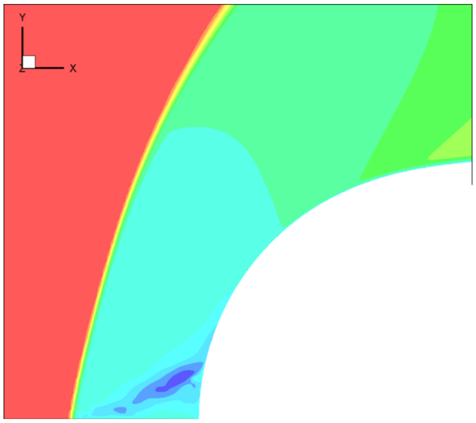

Figure 3.9: Zoom in of nose region of contour plot over straight cone at Mach 6 - flow velocity in x-direction.

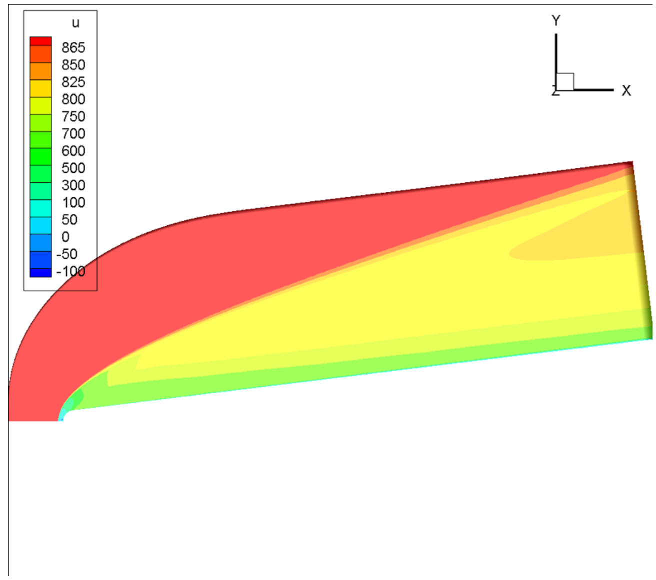

Figure 3.10: Contour plot over straight cone at Mach 6 - flow velocity in x-direction.

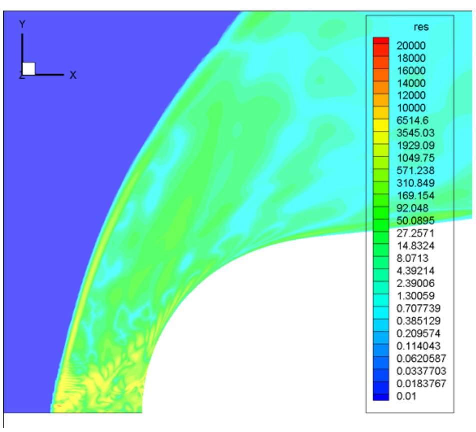

Figure 3.11: Zoom in of nose region of contour plot over straight cone at Mach 6 - spatial residuals.

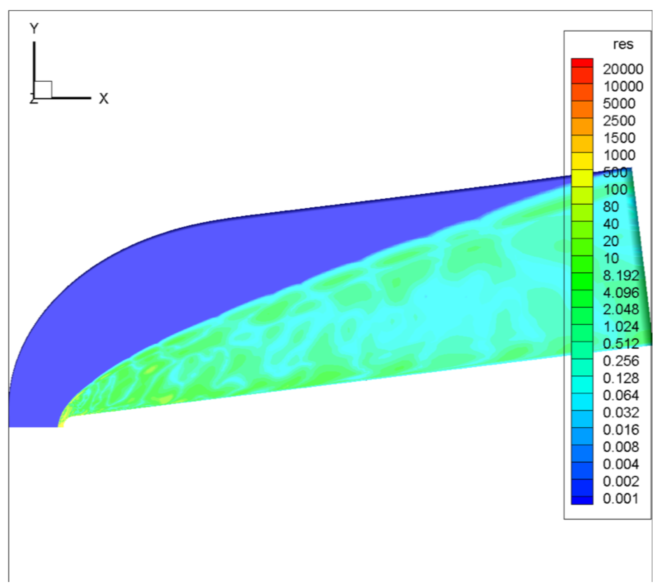

Figure 3.12: Contour plot over straight cone at Mach 6 - spatial residuals.

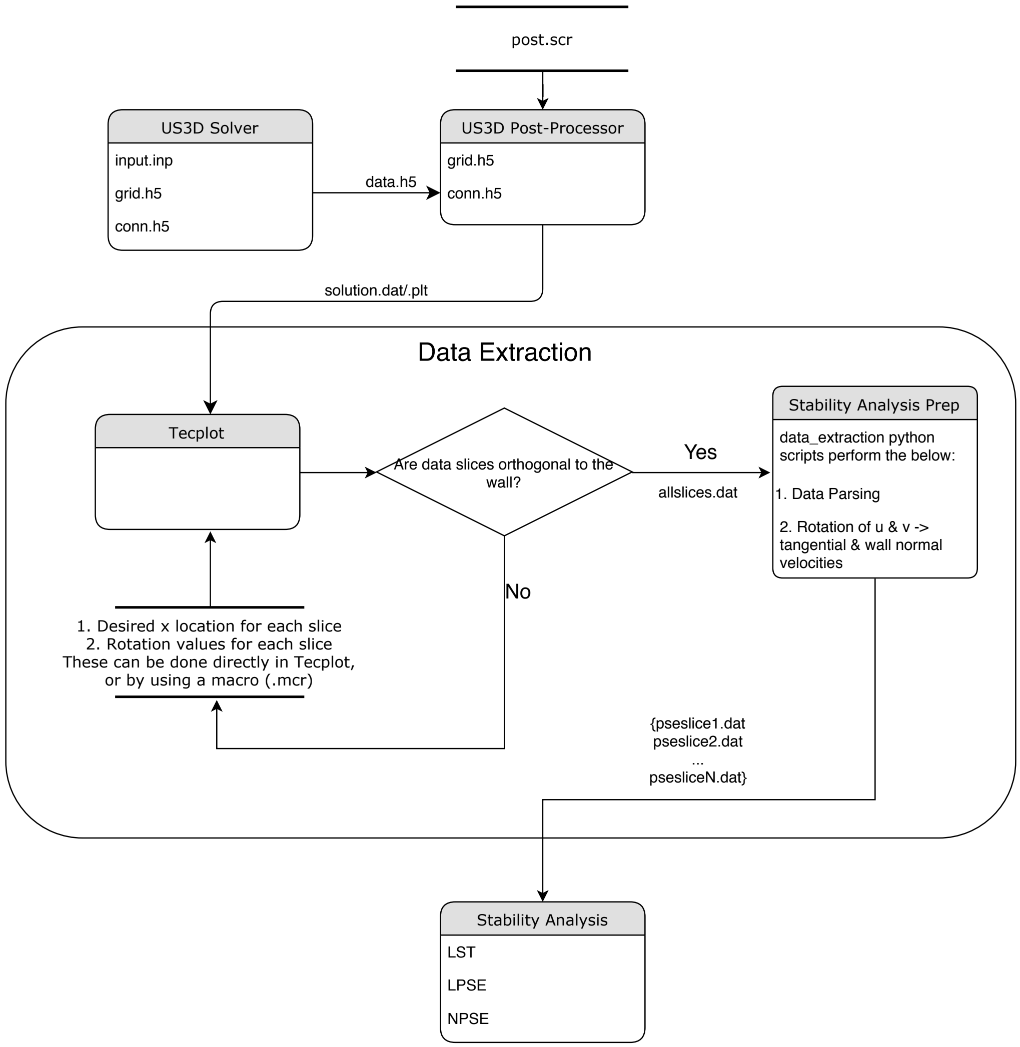

Figure 3.13: Data extraction process - Starting from the US3D solver output, to the data file slices for input into the stability solvers.

3.2.5 Data Extraction

After visualization, the data is extracted, validated, and then analyzed. The first thing to understand is that data extraction is a process, not a single operation. This process is illustrated in figure 3.13, and is described further in this section. The data needed for LST are: x,y spatial locations, u,v,w velocity components, density, and temperature. The data needs to be extracted at many different locations in wall-normal slices and then rotated in the wall-normal and wall-parallel directions. Scripts were written coupling Python, Matlab, and Tecplot macros to automate this process. For 2D, straight cones (constant half angle), this is a fairly straightforward calculation using the cone's half angle. However, for varying wall half angle, or non-constant wall vectors, this calculation is much more intensive.

In principle, data extraction is straight forward, however, when the geometry even has one varying angle in one direction, it can become more complex. Again, consider the Purdue flared cone with its changing wall contour. Most software packages have built-in features to extract planes or profiles of data at various locations. However in practice, and particularly when interfacing between multiple software packages, it is strongly recommended to carefully check the extracted data. It was found to be useful, to first extract straight profiles along the y-axis (perpendicular to the flow direction) to create a reference set of actual computational data, to create a reference, and to check for off-sets between expected (analytical calculations) and actual data positions. This is important if we recall, a model is generated in Solidworks, which is imported into Pointwise to generate a grid. That grid is imported into US3D to generate a flow field solution. That solution is imported into Tecplot for visualization, and data extraction along with any additional data parsing and preparation before finally being imported into the stability solver. This opens multiple opportunities for roundoff or truncation errors.

From the extracted y-axis data, rotation angles are calculated. These rotation angles are checked for being sufficiently perpendicular to the geometry's wall. Then this information is transformed into Tecplot rotation values, and fed-back into a Tecplot macro which extracts the wall normal data. Tecplot outputs a raw data file which is processed using in-house developed Python scripts to create individual data slice files of each desired streamwise location, at which x,y,u,v,T,ρ data are saved into a directory. For example, In the case of the flared cone, there were 451 files (slices) spanning 50mm to 500mm downstream in 1mm increments.

3.2.6 Validation

Validation of basic state solutions is vital part of the stability process, with availability of benchmarks being pivotal. Unless one is solving a brand new geometry or flow situation, there likely exists a prior created CFD solution, experimental data set, or analytic approximation. Verification can be as simple as checking to see that the Mach number of the flow field matches between your solution and the benchmark's, to extracting data from the benchmark and comparing boundary layer profiles, slice by slice, to performing multiple stability analyses looking for changes in the basic states' stability behavior. Secondary verification can also be achieve by comparing quantities derived from the basic state solution. For instance, it is common in stability and transition research to consider comparison of the bandwidth of instabilities between computations and experiment to serve as verification of a numerical basic state calculations [44]. Of course, as researchers blaze new territory, verification is not always possible. In such cases, research must rely on CFD best practices. Of particular importance in such cases are grid sensitivity studies. Multiple basic states are calculated with increasing grid resolution. As the grid is refined, if the change in the resultant solution becomes negligible, then one can state the grid is sufficiently resolved from this perspective given the computational variables at hand (ie. geometry, flow conditions, numerical scheme, etc...). Time permitting and driven by complexity and sensitivity requirements, all or a subset of the aforementioned validation techniques should be employed.

It should also be noted that this is not an exhaustive list of methods and best practices for creating basic states. This is the methodology which has shown to work sufficiently well for performing linear and parabolized stability analysis on streamlined bodies such as cones and wedges. Results of some basic states will be shown in the next section. There are many factors which include: fluid properties, flow properties, geometry, computational parameters, and phenomena to be studied. Each with their own complexities which must be addressed depending on the situation.

3.3 Computational Stability Analysis

The numerical solver employed in this research for performing linear stability (LST), linear parabolized stability equations (LPSE), and nonlinear parabolized stability equations (NPSE) is called JoKHeR which was developed by Dr. Joseph Kuehl and Dr. Helen Reed, at Texas A&M University, as part of the National Center for Hypersonic Laminar-Turbulent Transition Research [9]. An overview of the process for using the JoKHeR solver for numerical stability analysis will be described in this section.

3.3.1 LST

LST is solely performed in Matlab. First, the data slice files need to be imported into Matlab. This is done by the get_data script. This script takes as input, the data slices, the height above the wall just below the shock (shock cut off), and outputs a Matlab matrix file with this data in a format the LST solver can accept. Next, flow parameters, metric coefficients, and a grid need to be set up for the LST finite difference scheme. This step is performed by the build_dual.m script. The basic state data matrix file is inputted into build_dual.m which interpolates it onto a grid. The pertinent parameters shown below are required to be updated: gas type, in the case of this research it is air, the shock cut off point specified, the number of points past the N1 neutral point (Nx) (note: the neutral point is where the disturbance becomes unstable), the number of points above the wall (Ny), and the desired x location to analyze (xloc). Also, when performing LST, this desired x location is spanned in the streamwise direction, or for PSE preparation, it is a location just before the mode becomes unstable.

```
szy     = 350; % Shock wave data cut off point
xloc    = 35 % Desired location to run LST on
Nx      = 300; % Number location beyond N1
Ny      = 250; % Number of points in wall normal
%Gas parameters: ie. Air
R_gas     = 287.0580D0; %Gas Parameter for Air
mu_ref    = 1.716D0*10^(-5); %Gas Parameter for Air
```

```
gamma   = 1.40D0; %Gas Parameter for Air
```

After, build_dual.m has been set and ran, the generalized eigenvalue problem for real and imaginary parts of α as mentioned in section 2.3.3.2 can be solved by the Matlab script LST_traj.m. The key point for running LST_traj is to set the desired frequency (ie. 300 kHz), then after it has completed, to check the eigenvalue spectrum for a stable or unstable mode, then check its shape function or eigenmode matches the expected shape function for a second-mode. Examples are shown below. To investigate the eigenvalue spectrum, the following plot command is ran, then one zooms into the right-hand plane near the origin.

```
plot(real(diag(val)),imag(diag(val)),'k.')
```

Figures 3.14 through show an example of the spectrum, zooming into the region where the second-mode is found, and locating the eigenvalue which will end up being a second-mode. In figure 3.16 the second-mode is indicated by the selected value with the X: value corresponding to the real part of α, and Y: corresponding to the imaginary part of α.

Next, the below command is used for plotting the u component of the eigenvector or shape function.

```
plot(abs(vecu(:,index)),y_out,'k.-')
```

This shape function in figure 3.17 is indeed the second-mode looked for, whereas figure shows an example of a shape function which is not a second-mode which should be skipped over. For LST alone, the $-\alpha_i$ amplitude, x location, Reynolds number, frequency, non-dimensional frequency, and mode number would be saved.

This process is repeated by spanning various frequencies, and continuing to move downstream creating a region where eigenmodes are stable or unstable. The stable versus unstable region forms the linear stability diagram ("banana plot") [69]. An example of one where LST was performed on a straight cone at Mach 10 by Sakakeeny is shown in figure 3.19 [69].

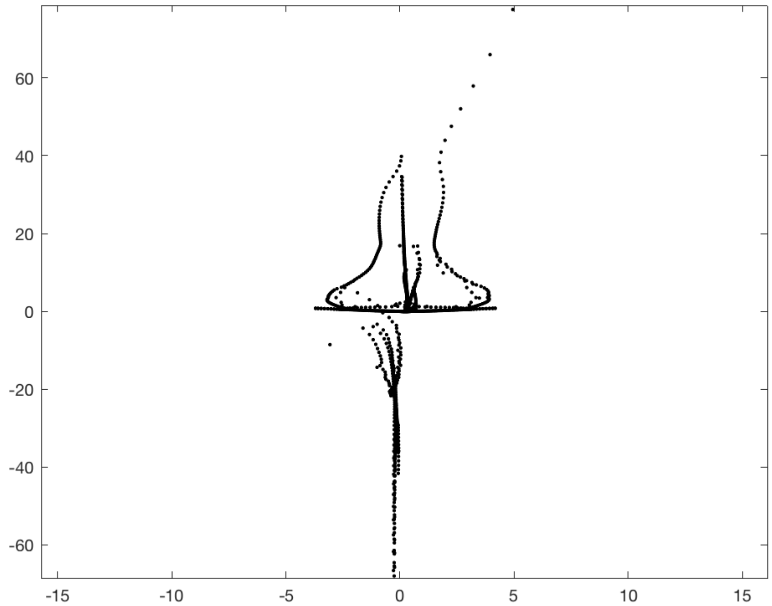

Figure 3.14: Eigenvalue spectrum plot 1.

3.3.2 LPSE

For LPSE and NPSE there are some differences when running LST. The first is that one does not span the streamwise locations of the cone like with LST. Instead, PSE integrates spatially downstream, so one performs the LST procedure until an unstable eigenmode is found. Then, keeping the frequency constant, one re-runs LST moving upstream until a barely stable second-mode is found. This stable second-mode's parameters are saved which will correspond to the initial conditions for PSE. In detail, the following are saved for the initial conditions: mode index, eigenvectors for u, v, w, temperature, density, and phase by running the Matlab script IC_traj.m.

After the desired initial mode has been saved from LST, we begin the LPSE. Running the LSPE and NPSE JoKHeR programs are similar, so the procedure will be described in general for LPSE, then the nonlinear aspects will be covered in the next section. JoKHeR is written in Fortran 95, supports thread level parallelism via

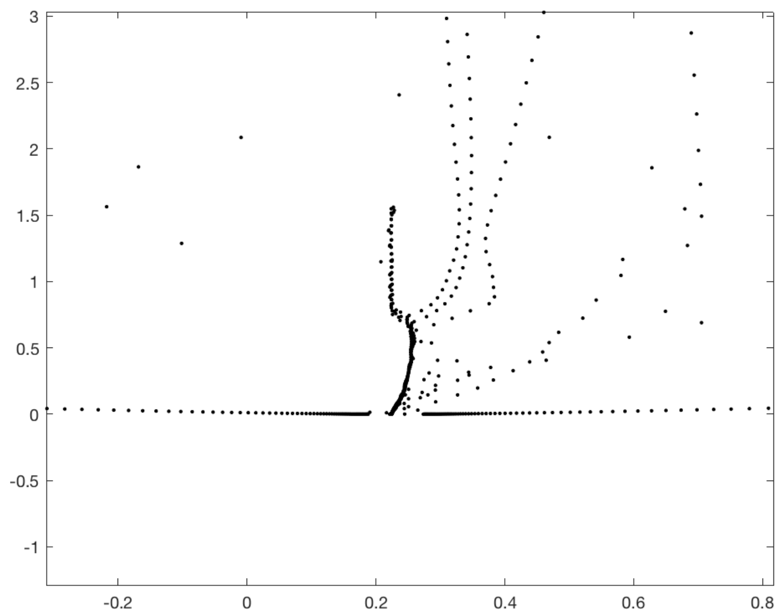

Figure 3.15: Eigenvalue spectrum plot zoomed in.

OpenMP, and is supported in Unix based systems. The buildlinear_Gaus.f95 source code file contains the discretized, linear PSE equations for mass, momentum, and energy to be solved which are passed into JoKHeR. The JoKHeR_MASTER_Lin.f95 file takes in the same Nx, Ny, and frequency values from LST. The Act_Nm and Nm parameters are set for the number of modes, which in the case of LPSE, is just one mode, its complex conjugate, and the mean flow distortion. Next, the desired initial amplitude is inputted. Then, buildlinear_Gaus.f95 and JoKHeR are compiled and linked using a Fortran compiler, and the program is ran. The program iterates performing Newton's method, integrating downstream. Very briefly summarizing, JoKHeR performs the following. An initial guess of the real (r) and imaginary (i) parts of $\Delta\alpha_{r,i}$ are made. Next, the system of equations is solved with $\alpha(j+1) = \alpha(j) + \Delta\alpha_r$ and $\alpha(j+1) = \alpha(j) + \Delta\alpha_i$. Then, normalization conditions are applied to determine the error sensitivity matrix. The matrix and the associated error is used to solve for the

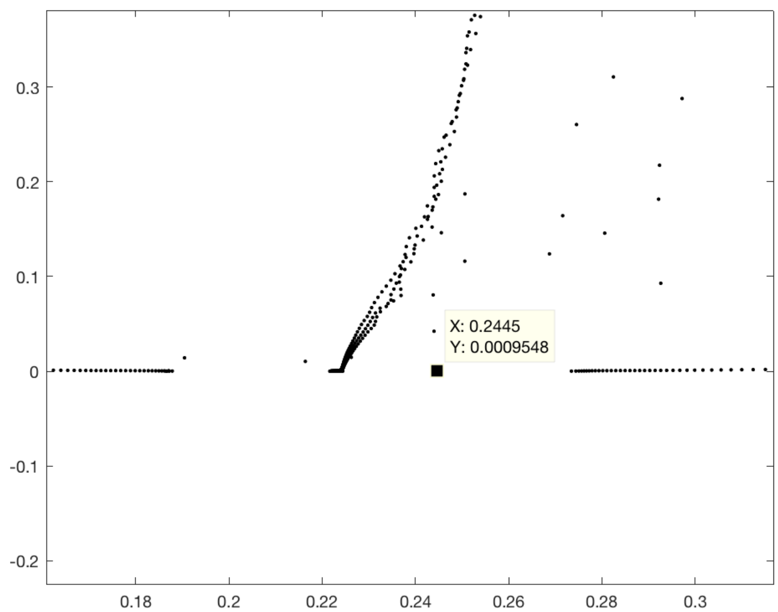

Figure 3.16: Eigenvalue spectrum zoomed in with eigenmode selected showing real and imaginary parts of α.

$\Delta\alpha_{r,i}$, and is repeated until the error is below a predefined tolerance. Finally, the program steps to the next streamwise location. This whole process is repeated until the last streamwise location is reached, or the solution diverges. In general, LPSE should march until the end, NPSE tends to diverge before the end because the amplitudes reach such large values. An example of a completed LPSE run is below.

```
converged =            0           1         299
NL Iteration =            1
NL Converge error =           1           1
NL U Value =    0.0000000000000000                            NaN
NL V Value =    0.0000000000000000                            NaN
NL T Value =    0.0000000000000000                            NaN
NL rho Value =    0.0000000000000000                            NaN
rlx =    1.0000000000000000
err =  (  2.7807773173970513E-014, -9.4225944897356837E-014) (
converged =            0           1         299
D error D alpha i r
                      NaN
```

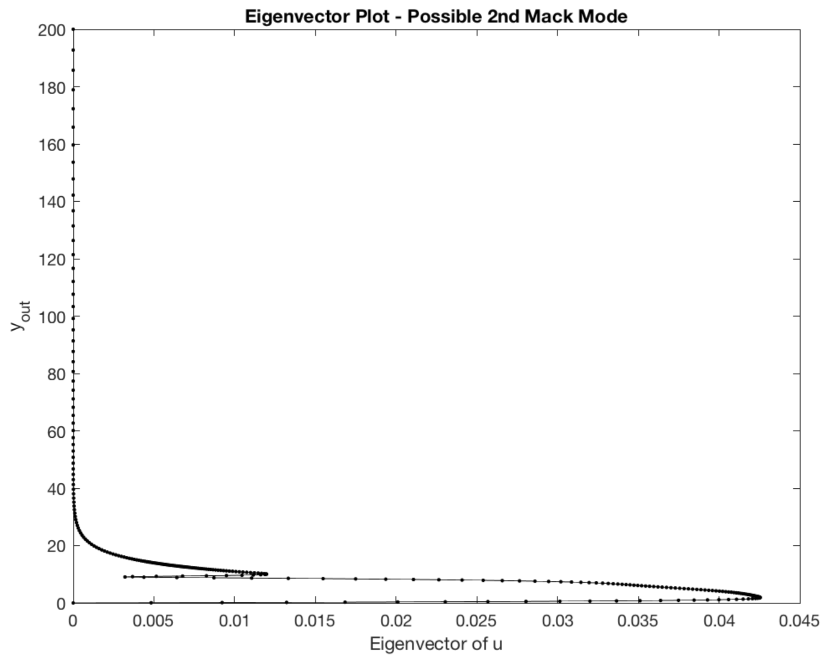

Figure 3.17: Proper shape function of eigenvector/eigenmode for the second-mode.

```
                      NaN
                      NaN
                      NaN
 New Dalpha_r =    0.0000000000000000                            NaN
 New Dalpha_i =    0.0000000000000000                            NaN
 Max (1,0) =    82068038.727231905
CPU Time =                439.667 seconds.
User Time =                232.805 seconds.
Armanis-MacBook-Pro:300khz_test2 revmac$
```

Once the LPSE has converged, the results are plotted as N-factors (denoted N):

$$N = ln\left(\frac{A}{A_0}\right) = -\int_{x_0}^{x} \alpha_i dx \tag{3.4}$$

where A is the amplitude at its respective streamwise location, and A_0 is the initial amplitude at the N1 neutral point [70]. An example is shown in figure 3.20. The growth rate shows how the disturbance grows linearly downstream. Since it is a log scale,

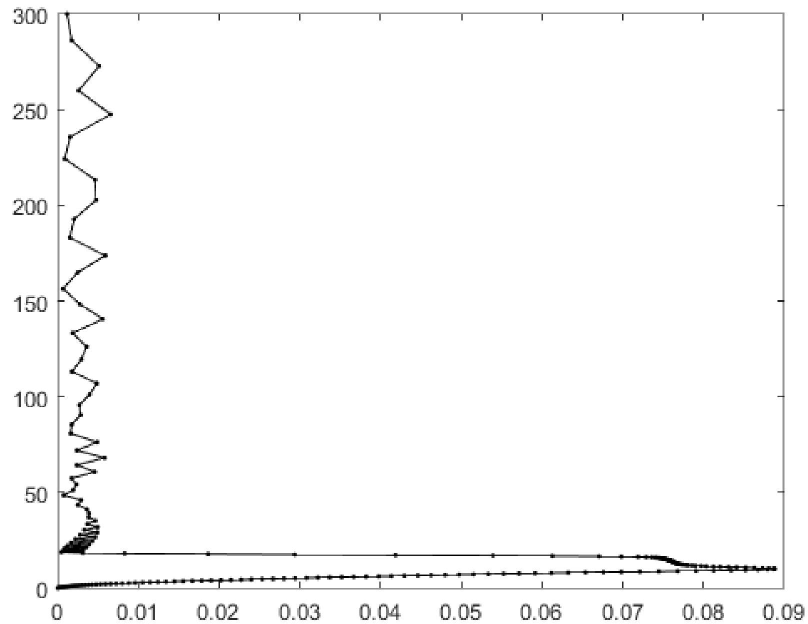

Figure 3.18: Incorrect/non-physical shape function example of eigenvector/eigenmode for the second-mode.

small N-factor increases, correspond to order of magnitude differences in the disturbance amplitude. If the disturbance decays as it traverses downstream, this means the disturbance is stable at its respective frequency, and does not contribute much overall to transition. Otherwise, a growing N-factor corresponds to an unstable frequency, with the largest N-factor(s) contributing the most to second-mode instability. Then, the LPSE process is repeated by spanning many frequencies, plotting their N-factors to see which modes grow the most. The results can then be compared to the experimental or other computational results.

3.3.3 NPSE

The NPSE setup is similar to LPSE, however, LST is first ran on multiple modes (frequencies) to create multiple initial conditions to be input into NPSE which are summarily saved using IC_multi.m. In addition to LPSE equations for mass, momentum,

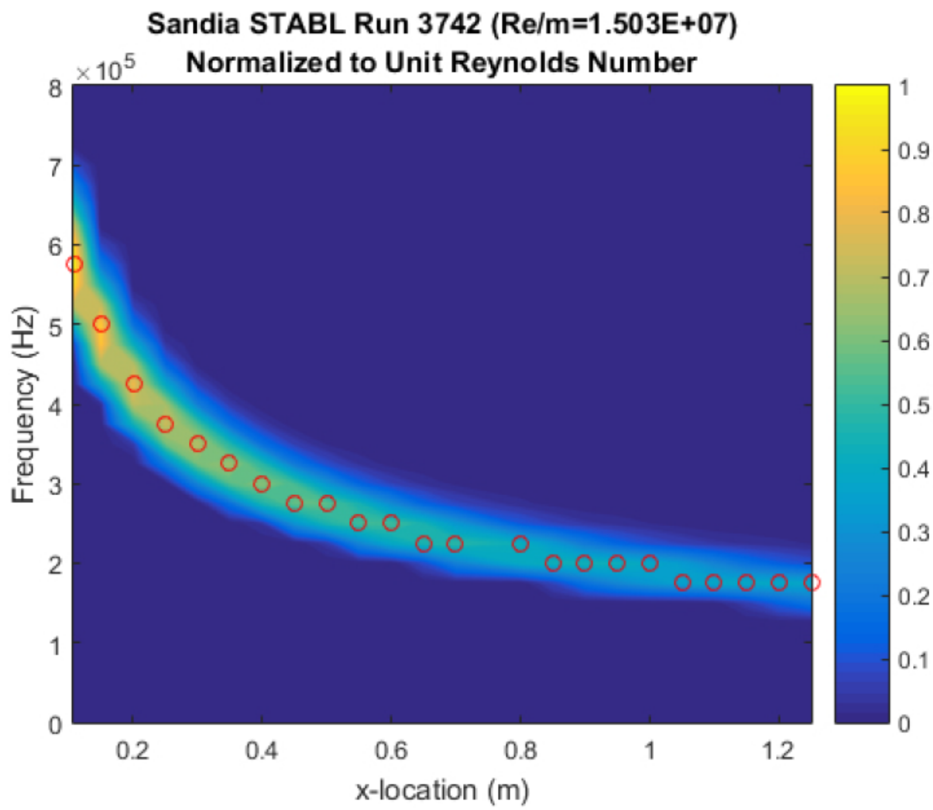

Figure 3.19: Mach 10 straight cone LST results: plot of frequency (ω) vs streamwise x location (used with permission) [69].

and energy defined in buildlinear_Gaus.f95, NPSE JoKHeR has the quadratic and cubic nonlinear terms specified in files: buildquad_Gaus.f95 and buildcubic_Gaus.f95. These are passed into JoKHeR_MASTER_Gaus.f95, along specifying the desired number of primary modes, harmonics, their complex conjugates, and the mean flow distortion. Next, all the frequencies are specified and the initial amplitudes, see table 3.3 for a 3-mode case example. For the initial amplitudes, the primary disturbance is set based on an amplitude which will grow sufficiently large downstream, yet not too high initially, otherwise it will cause the NPSE to diverge when calculating. Then, the harmonics are set as powers of the primary disturbance initial amplitude (ie. 1st harmonic is the primary's amplitude squared, the 2nd harmonic is the primary's amplitude cubed). Lastly,

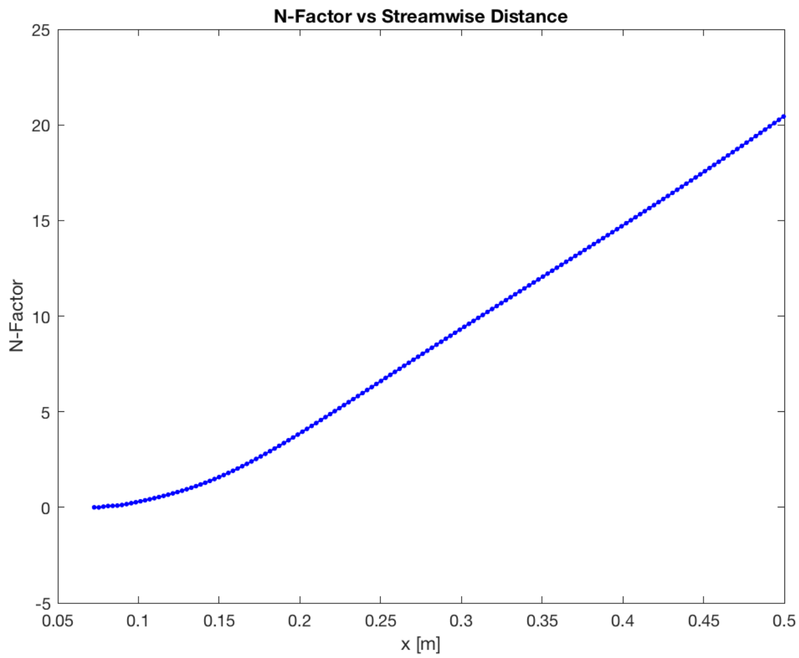

Figure 3.20: Example LPSE run results: N-factor vs x location along Purdue flared cone.

JoKHeR_MASTER_Gaus.f95, buildlinear_Gaus.f95, buildquad_Gaus.f95, and buildcubic_Gaus.f95 are all compiled, linked, then the program is ran (commands listed below).

```
1. Compiling the build source code files
1a. Required for both LPSE or NPSE:
gfortran -c buildlinear_Gaus.f95

1.2 Only required for compiling NPSE:
gfortran -c buildquad_Gaus.f95
gfortran -c buildcubic_Gaus.f95

2. Compile and link with JoKHeR main source code
2a. Linux/UNIX:
gfortran -fopenmp JoKHeR_MASTER_Gaus.f95 -o pse buildlinear_Gaus.o ...
buildquad_Gaus.o buildcubic_Gaus.o

2b. Mac OS X:
gfortran -fopenmp JoKHeR_MASTER_Gaus.f95 -o pse buildlinear_Gaus.o ...
buildquad_Gaus.o buildcubic_Gaus.o -framework Accelerate
```

```
3. Running LPSE or NPSE and redirecting output to a file:
./pse <frequency> >> <pse_output_file.txt> &
```

Table 3.3: 3-mode frequencies and initial amplitudes example

Primary Mode [kHz]	Low Frequency Side Lobe [kHz]	High Frequency Side Lobe [kHz]	Initial Amplitude Amplitude
300	270	330	1.0×10^{-7}
600	540	660	1.0×10^{-14}
900	810	990	1.0×10^{-21}

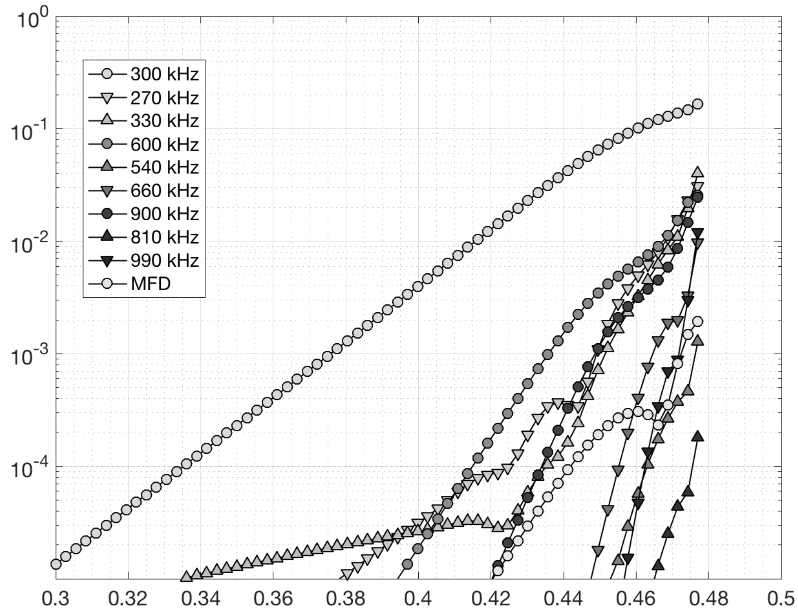

Figure 3.21: Example NPSE run results: root mean square (RMS) of disturbance pressure vs x location along Purdue flared cone for 3 primary modes, 1st and 2nd harmonics, and mean flow distortion.

Again, divergence of the solution for NPSE is common, due to the large disturbance growth or stronger nonlinearities. As such, a sufficiently far downstream march is required, and is compared to the streamwise disturbances measured from experiments. If the NPSE reaches these experimental distances, this divergence before the last data slice is acceptable, otherwise, the input parameters, the initial conditions, or even the source code must be edited to a more stable setup. Figure 3.21 shows an example result of the amplitude growth in root mean square of disturbance pressure vs streamwise location. This plot tells us how the primary disturbance, harmonics, and mean flow distortion grow and interact. Important disturbance aspects are identified: such as growth of the primary mode, side lobes, harmonics, spectral broadening for the wavepacket formulation NPSE (traditional delta function NPSE will not have this interaction), and amplitudes, or labeled as missing and changes would be made in order to better quantify the flow's disturbance growth behavior.

The PSE results are compared to experimental and/or DNS results, the input parameters are changed (ie. initial amplitude, side lobe bandwidth, number of modes, or harmonics), then re-ran and compared again. This is an iterative process, where additional physical phenomena, frequency bandwidths, disturbance mode types or interactions such as: oblique or k-type are tested and refined in the PSE in order to test and push its abilities further to quantify second-mode disturbances physical mechanisms to understand linear and nonlinear behavior, growth, interactions leading to instability and transition within the hypersonic boundary layer.

3.4 Resources

3.4.1 Computational

Since this dissertation is primarily computational research, the required resources are: a sufficiently powerful compute cluster to generate basic states flow fields, and computer workstations running a flavor of Linux, Unix, or Mac OS X with sufficient power to run LST and PSE. Experimental and DNS results were provided by collaborators.

3.4.2 University Collaborations

Experimental data and results from Purdue University's BAM6QT were provided by: Dr. Steven Schneider and Dr. Brandon Chynoweth. DNS results and data

were provided by: Dr. Carlo Scalo and Victor Sousa also of Purdue. Additional research collaborations were with: Dr. Herman Fasel and Christoph Hader of University of Arizona, Dr. Thomas Juliano of Notre Dame University, and Dr. Bradley Wheaton of Johns Hopkins University Applied Physics Laboratory are also acknowledged here.

3.4.3 Funding

This research was funded under the Air Force Office of Scientific Research (AFOSR) Grant# FA9550-15-1-0129.

Chapter 4

A MECHANISM FOR SPECTRAL BROADENING AND IMPLICATIONS FOR SATURATION AMPLITUDE ESTIMATES

The "wavepacket" formulation of the Nonlinear Parabolized Stability Equations (NPSE) [7] is applied to identify the mechanisms responsible for spectral broadening which is observed in hypersonic boundary layers. It has been suggested that the presence of low frequency "noise" is responsible for spectral broadening. The results presented here suggest that spectral broadening is a consequence of finite bandwidth frequency content, and a mismatch of spectral bandwidth between primary and first harmonic disturbances, not the presence of low frequency "noise". Indeed, our results suggest that low frequency noise is a consequence of the spectral broadening, not a driver of spectral broadening.

4.1 Basic State - Flared Cone

The Purdue flared cone geometry at Mach 6 is considered. A basic state (steady state) CFD solution was generated in US3D for each of the 4 cases listed in the table 4.2. The 'base' case corresponds to the experimental conditions run by Dr. Chynoweth [10]. The other three cases were perturbations about the basic state of +/- 10% to the Reynolds number (by increasing the flow velocity), and a 10.8×10^6 Re case by increasing the freestream density [46].

Table 4.1: BAM6QT Experimental Tunnel Conditions For Run 825 [10].

$P_{0,i}$ [kPa]	$T_{0,i}$ [K]	P_0 [kPa]	$Re \times 10^{-6}/m$	γ_{air}
8.9676	434.85	8.361	9.2	1.4

Table 4.2: US3D Run Conditions for Base and Basic State Perturbation Cases [46].

Run Case	Boundary	ρ [kg/m^3]	T [K]	u [m/s]
Base	Inflow	0.0355	51.9799	867.1092
Re +10%	Inflow	0.0355	51.9799	953.8201
Re -10%	Inflow	0.0355	51.9799	780.3983
Re/m = 10.8×10^6	Inflow	0.0417	51.6448	864.3102
All Above	Wall	N/A	300	N/A

The Mach contour plot of the basic state result is shown in figure 4.1. This contour was compared to the flared cone results by Fasel et al. [26]. Though not a quantitative comparison, the Mach contours showed good agreement and stability analysis was conducted.

4.2 Results

4.2.1 LST

A preliminary LST analysis was performed to determine the frequency range of the Mack mode disturbances and for the initial conditions of the PSE analysis. The LST results can be seen in figure 4.3. This preliminary LST was performed at the spatial location of 150mm downstream from the nose tip. The most unstable frequency was 285 kHz with an unstable bandwidth of roughly 100 kHz. This bandwidth is consistent with experimental results [41, 46, 71].

4.2.2 LPSE

With the LST results in hand, they were used to guide the linear PSE (LPSE) calculations. Selected frequencies starting at 285kHz were performed, then tested at higher and lower frequencies. For quantifying disturbance growth from LPSE, the N-factor is calculated: $N = ln(A/A_0)$ where A is the amplitude and A_0 is the initial amplitude. The N-factors were calculated for each frequency, and the results are shown in figures 4.4 and 4.5 below. Recall that the LPSE is integrating spatially downstream

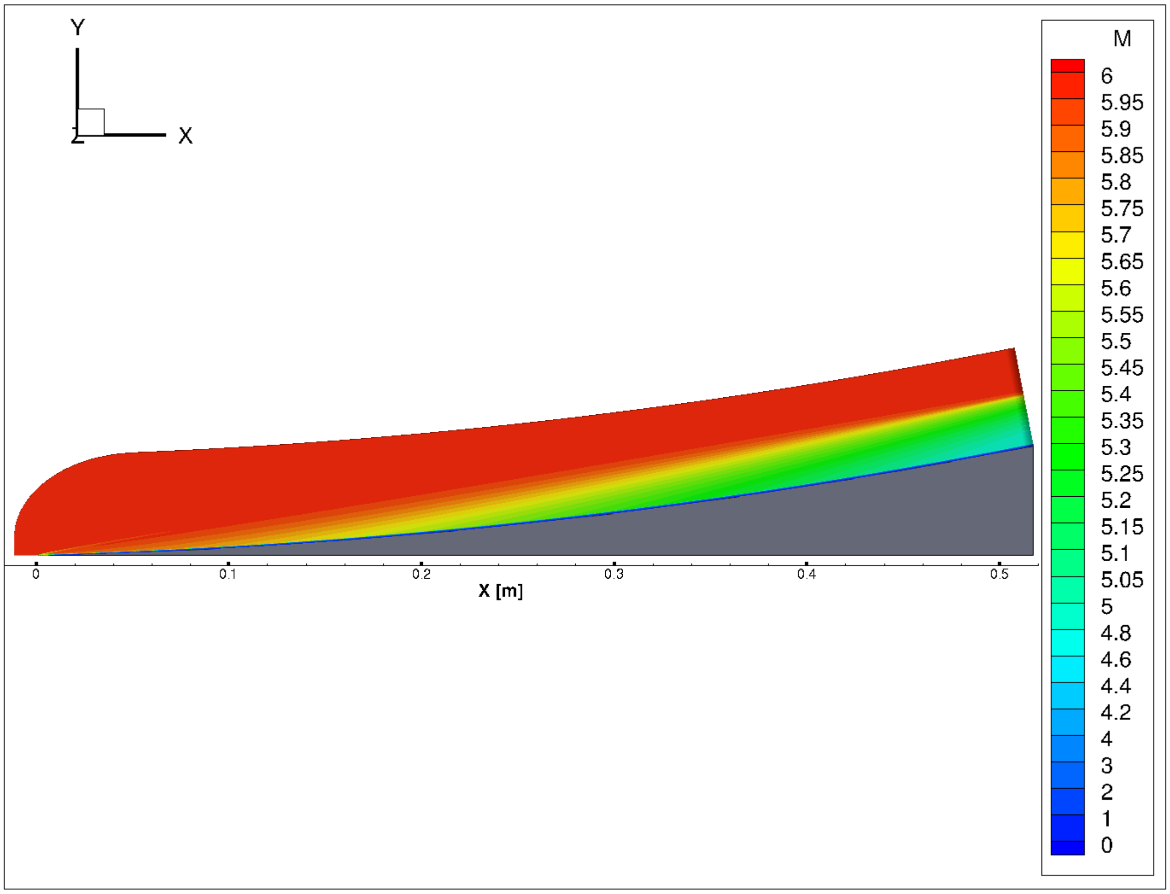

Figure 4.1: Mach contour plot of basic state solution of flared cone generated using US3D [46].

along the cone from 50mm to 500mm. The base case (Re-9.2) shows the N-factor with the greatest contribution of disturbance at frequencies of 270kHz to 275kHz. This shows the LST was a good first pass, and the LPSE homes in on which disturbances grow largest as they run their course.

Due to uncertainty prevalent in attempting to match computational results to numerical results, an LPSE sensitivity study was performed. Experimental data showed that the largest disturbance frequency should have been closer to 300kHz, not 270 kHz [10, 46]. The Re+10% and Re 10.8 cases show 295kHz as the most amplified, with 290kHz and 300kHz spanning it, but the Re 10.8 case had 300kHz N-factor almost as high as the 295kHz frequency. Lastly, the Re-10% case shows 250kHz to 255kHz as the

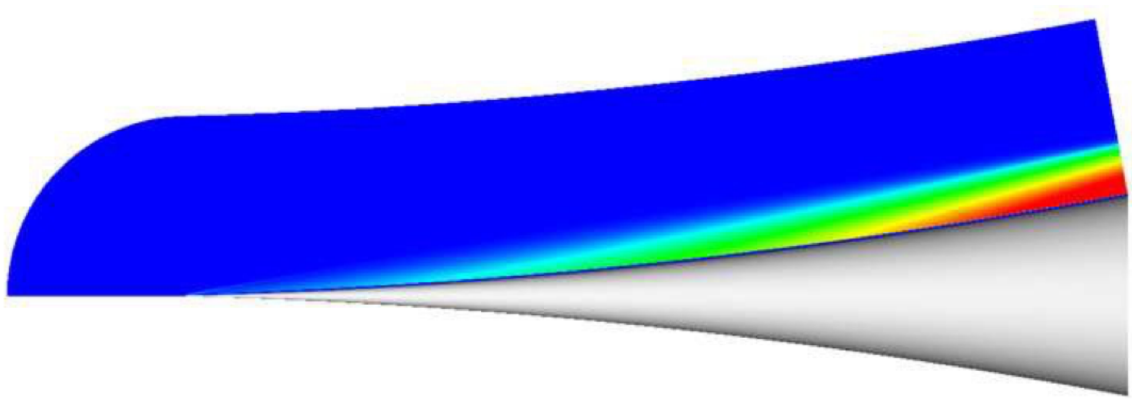

Figure 4.2: Contour plot of basic state solution benchmark (used with permission) [26].

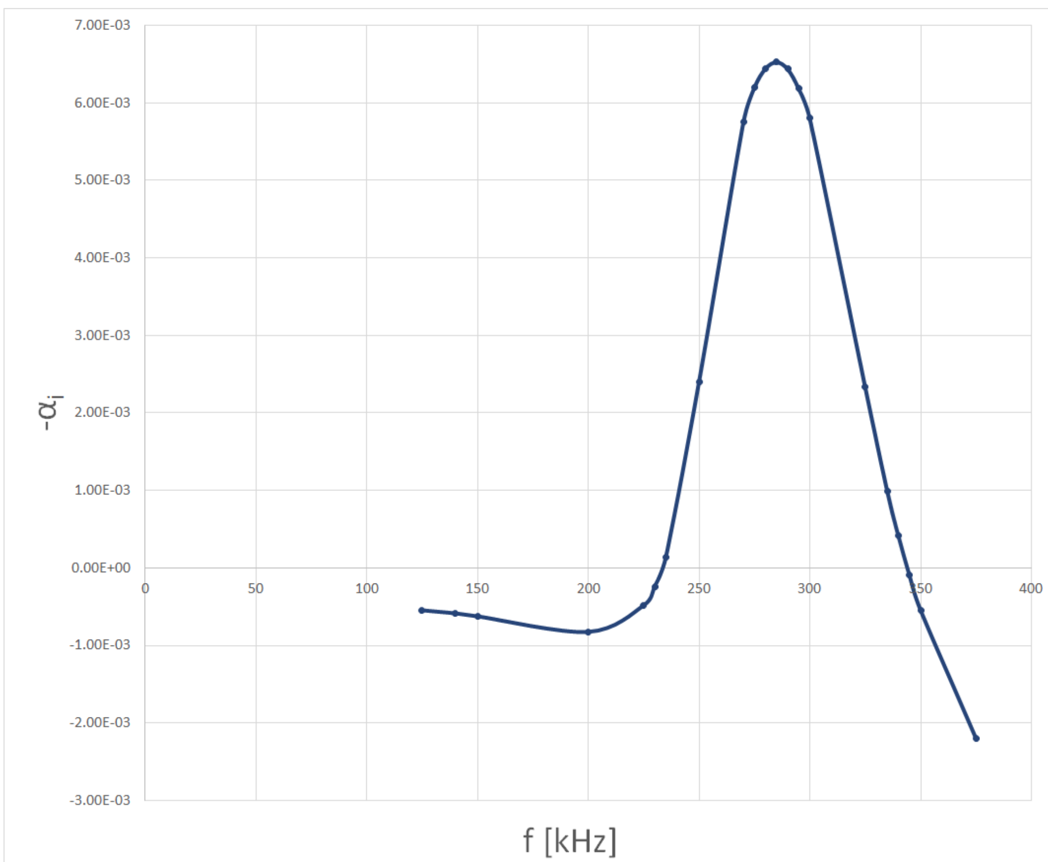

Figure 4.3: Linear Stability Theory (LST) results of the base case at 150mm downstream [46].

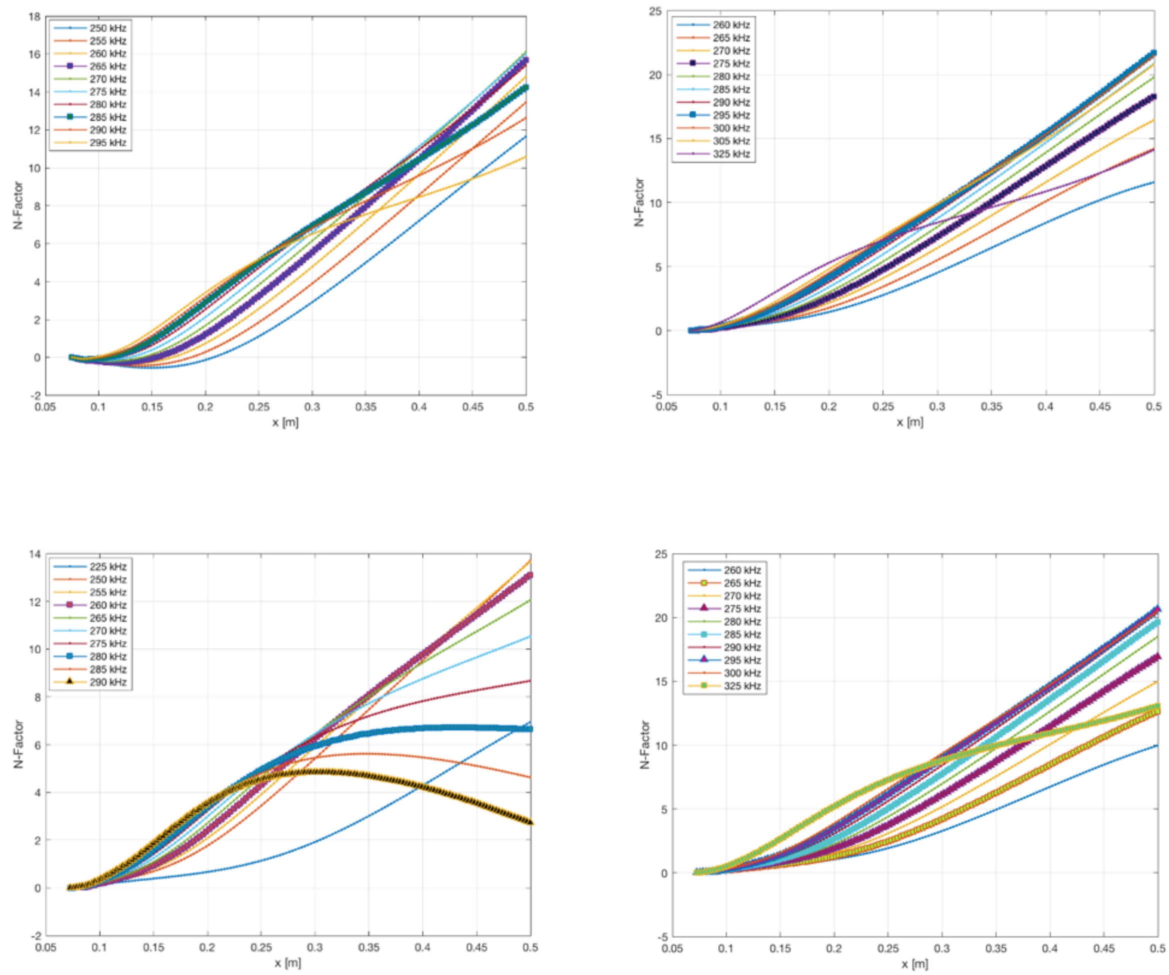

Figure 4.4: LPSE Results N-Factors vs streamwise distance cases: upper-left base, upper-right Re+10%, lower-left Re-10%, lower-right Re 10.8 (closest largest N-factor frequencies to experiments) [46].

most amplified. The trend of higher frequency with higher unit Reynolds number is consistent with standard theory that higher Reynolds numbers yield narrower boundary layers and thus higher frequency Mack modes [46]. However, the sensitivity of the most unstable frequencies is quite high [46]. Note that the experimental results, base case with Re 9.2, observe unstable Mack mode frequencies of approximately 300kHz. The LPSE calculations ran at the Re 10.8 case achieved sufficiently close frequency Mack modes. It was stated by the Purdue group that part of this discrepancy was caused by the test article not being exactly at an angle of attack of 0 degrees, along with potential

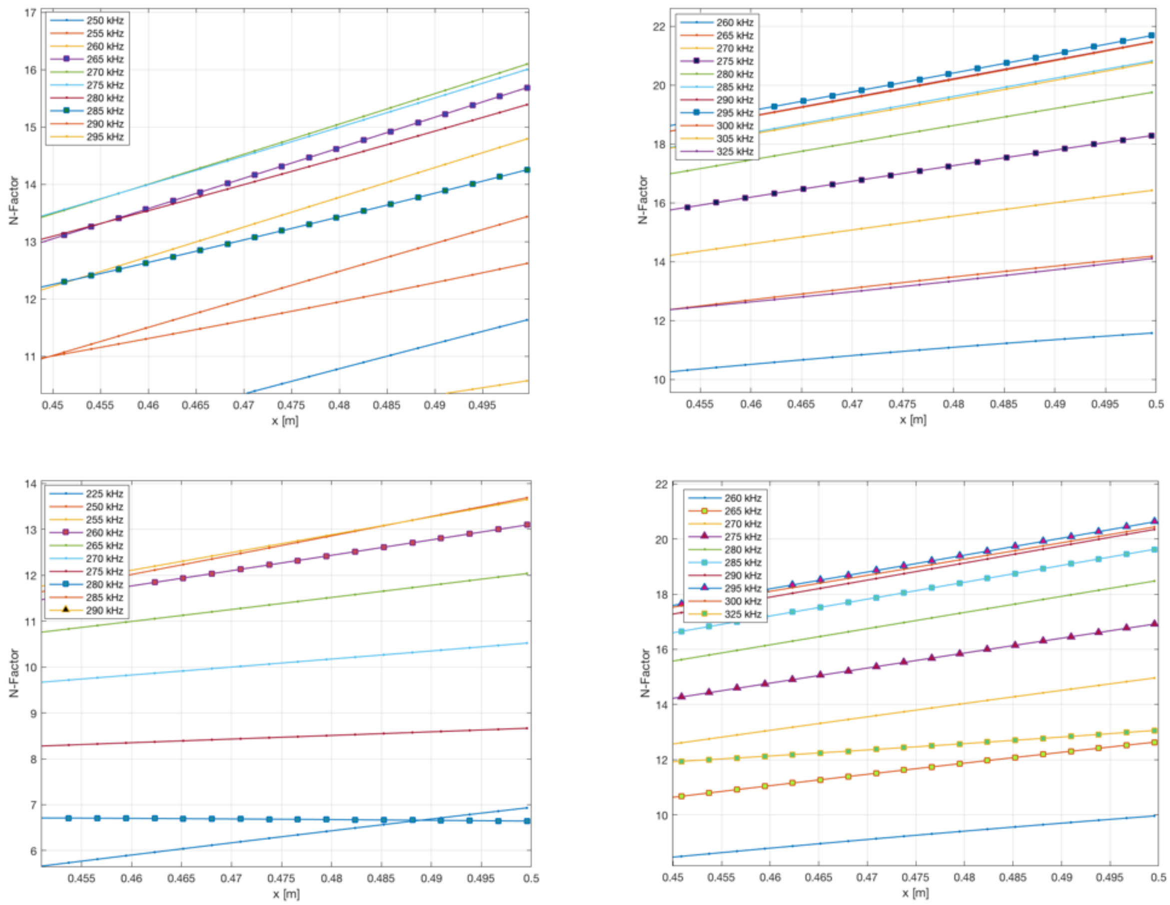

Figure 4.5: A zoom in of the LPSE results cases: upper-left base, upper-right Re+10%, lower-left Re-10%, lower-right Re 10.8 [46].

pressure concerns found within the BAM6QT tunnel at the time [46]. Furthermore, numerical investigations have inherent simplifications which can cause this Reynolds number to differ in order to achieve the same disturbance frequencies. Subsequently, the Re 10.8 case was chosen to investigate further for nonlinear analysis since it more closely matched the experimental results.

4.2.3 NPSE

Nonlinear (NPSE) calculations were carried out on the Re 10.8 basic state solution for the primary Mack mode frequency of 300kHz. The intent is to illustrate the effect of the new formulation on spectral broadening and disturbance amplitude

[46]. Two cases were considered: First, discrete mode (traditional delta function NPSE where $W(\omega) = \delta(\omega - \omega_0)$) representation of 300kHz, 250Kz, 350kHz and 50kHz Mack modes, plus harmonics, and second, Gaussian wave packet representation of 300kHz, 250Kz, 350kHz and 50kHz Mack modes, plus harmonics [46]. All disturbances were initialized with LST eigenfunctions and given initial amplitudes of 2.5×10^{-8} (normalized temperature disturbance based), just upstream of the 300kHz neutral point [46]. The 300kHz mode represents the primary disturbance wave packet, and the 250kHz and 350kHz disturbances represent the "side lobes" which along with their finite bandwidths, account for spectral broadening [46]. The 50kHz disturbance represents low frequency content or "noise" at a particular frequency as one might find inside a wind tunnel. It has been suggested that low frequency content is the cause of spectral broadening, via coupling with the primary mode [46]. Here, we address the mechanism of spectral broadening directly through comparison of the discrete and wavepacket cases [46]. Shown on the left-hand side of figure 4.6 is the discrete case, and on the right-hand side is the wavepacket case. Figure 4.7 shows the wavepacket case again, but with initial disturbance amplitudes of 5×10^{-8} for the primary disturbance and side lobes and 5×10^{-7} for the 50kHz low frequency content. In figure 4.8 the sum of the primary and side lobes RMS streamwise velocity disturbance amplitudes are compared to the primary disturbance alone for the wavepacket case. The left side shows calculations with an initial amplitude of 2.5×10^{-8} (normalized temperature disturbance based), and the right side shows a 5×10^{-8} initial amplitude calculation.

4.3 Discussion

The emphasis of this study was to peer into and apply the physical mechanisms which drive spectral broadening. Figures 4.6 and 4.7 show that the presence of low frequency noise does not provide a link between the primary disturbance and side lobes in the discrete (delta) mode formulation [46]. Thus, the discrete formulation does not result in spectral broadening, however, the wavepacket formulation does [46]. Consistent with Kuehl (2017), it is found that the mechanism driving spectral broadening is

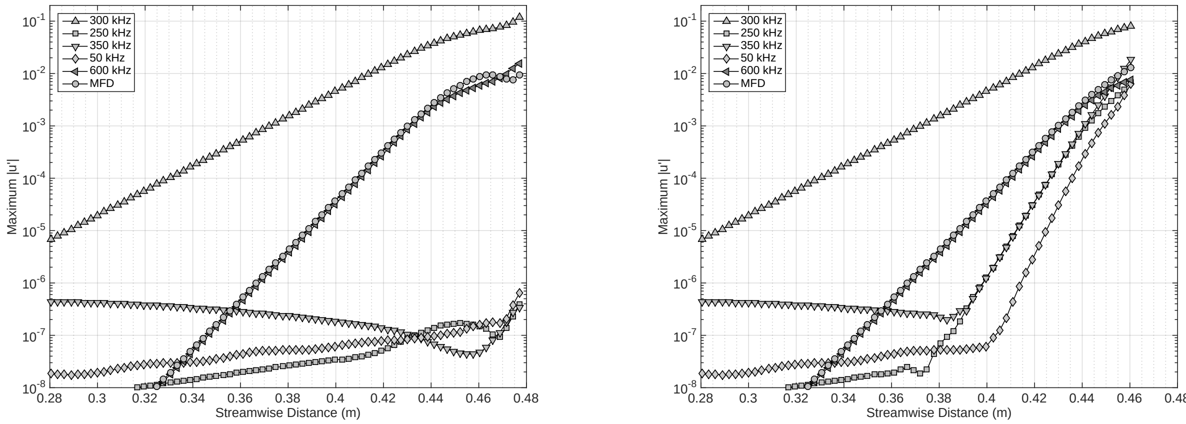

Figure 4.6: NPSE simulations of a Mach 6 Purdue flared-cone. Shown are maximum streamwise velocity disturbance amplitudes for a discrete mode case (left) and the wave packet formulation (right). Initial amplitudes are set to 2.5×10^{-8} for the primary disturbance, side lobes and for the 50kHz "noise" [46].

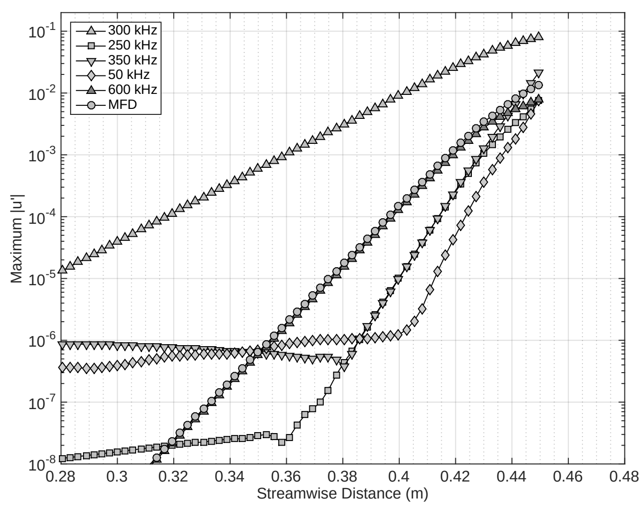

Figure 4.7: NPSE simulations of a Mach 6 Purdue flared-cone. Shown are maximum streamwise velocity disturbance amplitudes for the wave packet formulation (right) with initial amplitude of 5×10^{-8} for the primary disturbance and side lobes and 5×10^{-7} for the 50kHz "noise" [46].

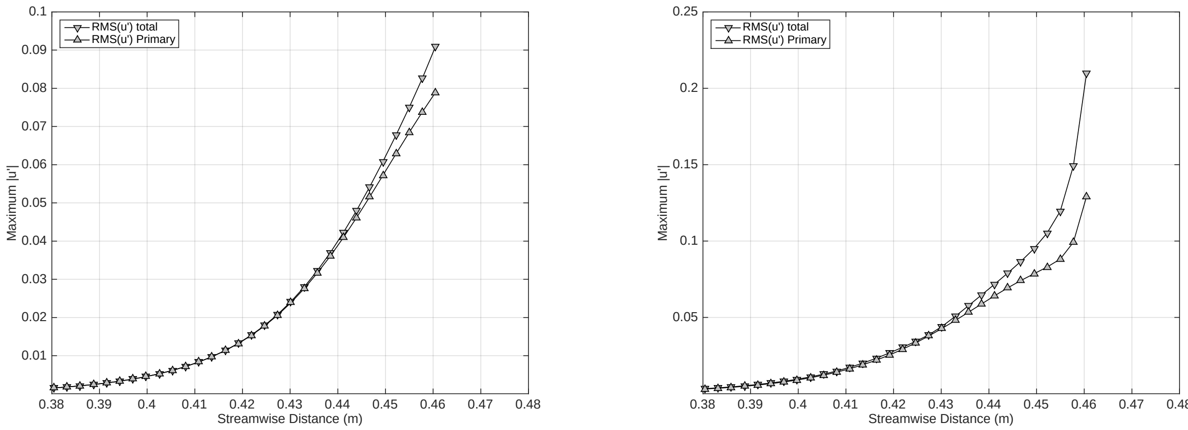

Figure 4.8: NPSE simulations of a Mach 6 Purdue flared-cone. Shown is the sum of primary and side lobe RMS streamwise velocity disturbance amplitudes compared to the primary disturbance alone, for the wave packet case. The left panel shows calculation with an initial amplitude of 2.5×10^{-8} (normalized temperature disturbance based) and the right panel shows a 5×10^{-8} initial amplitude calculation [46].

a mismatch in frequency bandwidth between primary disturbances and first harmonics, and therefore the traditional delta function approach cannot account for spectral broadening in its current form [7]. Therefore, there is a primary + complex conjugate first harmonic quadratic coupling that projects energy directly onto the side lobes [46]. Moreover, the low frequency content ("noise") is observed to grow, but only after spectral broadening has begun [46]. Even when the low frequency "noise" is given an order of magnitude larger initial amplitude, it does not grow until after the harmonic has been excited, see figure 4.7 [46]. Therefore, a scenario for spectral broadening that is consistent with experimental observations and theory, is [46]:

1. Finite bandwidth primary disturbances are initiated in the boundary layer and grow linearly.

2. As the primary disturbance amplitude increases, harmonics are generated with

wider spectral content ($\sqrt{2}\sigma_0$), indicating nonlinear growth.

3. Following the growth of the harmonics, nonlinear feedback between the primary disturbance and first harmonics (due to frequency bandwidth mismatch) drives slide lobe growth, ie. spectral broadening.

4. Once spectral broadening occurs, the side lobe and primary disturbance interactions drive the low frequency disturbances.

The affect of spectral broadening on disturbance amplitude prediction is illustrated in figure 4.8 [46]. It should be remembered that disturbance amplitude is calculated by integrating over the spectrum (approximated here by summing individual disturbance RMS amplitudes). While the primary mode saturates and detunes, the spectrum broadens, then, this broadening results in continued total disturbance growth [25, 46]. Such growth is important for nonlinear amplitude based transition and accurate disturbance amplitude predictions. Note, the approach adopted in this manuscript is idealized by targeting specific disturbance interactions to study spectral broadening mechanisms [46].

Chapter 5

A HISTORY AND PROGRESS OF RESEARCH ON BOUNDARY-LAYER TRANSITION ON A MACH 6 FLARED CONE

5.1 Introduction

This chapter represents two published review papers: one is the NATO paper published in the AIAA SciTech 2018 conference, and the other published in the Journal of Spacecraft and Rockets (JSR). This was a collaborative work on the Mach 6 Purdue flared cone conducted by researchers from Purdue University, University of Arizona, Notre Dame, John Hopkins Applied Physics Lab, and Baylor University / University of Delaware. A synergistic approach among experiment (section 5.2.1), DNS (section 5.2.2), and stability analysis was used to further understand the laminar-turbulent boundary layer transition on the flared cone. For the sake of brevity, the updated collaborative contributions from the conference and journal articles will be presented together in section 5.2, and the contributions from our research group will be presented in sections 5.3 and 5.4.

5.2 Collaborator Results Summary

5.2.1 Collaborator Experiments on Purdue Flared Cone [42, 43]

This section represents results and contributions by collaborators: Chynoweth, Schneider, Juliano, and Wheaton [42, 43]. The range of unit Reynolds numbers between 7.3×10^6/m and 12×10^6/m were tested of the flared cone with a smooth wall which were performed by Chynoweth. These experiments focused on two different aspects of the second-mode instability. First, the natural breakdown was studied to quantify as many aspects as possible of the non-linear growth, breakdown, and transition to turbulence of the second-mode wave on a smooth wall [42, 43]. The goal of the other set of experiments was to produce roughness elements which interact with the second-mode instability rather than tripping the boundary layer to control the observed heating pattern. It was found that when a roughness interacts with the instability, the second-mode is still the dominant transition mechanism [42, 43].

Figure 5.1 show the TSP results of the experiments. Also, the model was rolled by 30° between the tests. "The streamwise streaks of heating rolled by the same angle, showing that the vortices were body fixed" [42, 43]. When the asymmetric circumferential formation of the streamwise streaks was first observed, the cause was unknown [42, 43]. Willems (2015) showed that a small angle of attack (AoA) could lead to non-uniform transition on a 3° half-angle cone in a way that looked similar to the flared cone tests [42, 43, 72]. Willems used a specialized angle-of-attack adapter to make micro-adjustments to the pitch and yaw of the cone [42, 43]. As such, an adjustable angle-of-attack adapter was fabricated for the flared cone too.

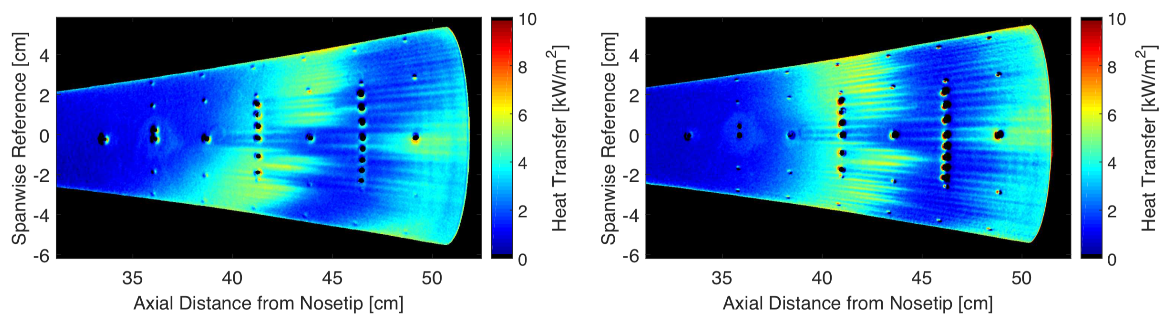

(a) Prior to AoA Adjustment

(b) After AoA Adjustments

Figure 5.1: (Left) Streamwise heat transfer profile before alignment with the streaks of heating. (Right) Streamwise temperature profile aligned with the streaks of heating (used with permission). [42, 43].

Figure 5.1(a) is a TSP image of the flared cone prior to adjustment at a unit Re of 9.7×10^6 /m. The streamwise streaks began almost 5 cm further on the bottom than on the top portion of the cone [42, 43]. Next, the model was pitched downward by roughly 0.1°, and yawed less than 0.1° towards the camera [42, 43]. The frequencies of the peak second-mode wave measured by 4 PCB pressure sensors spaced 90° apart at a streamwise distance of 39.0 cm from the nosetip [42, 43]. Once the sensors were measured to have similar frequencies, meaning each was less than 2% off from the mean, the model was deemed properly aligned to the incoming flow. Figure 5.1(b) shows that the beginning of the streaks happens more uniformly around the circumference starting near 39 cm from the nosetip [42, 43].

Increasing Re_∞ caused the heating pattern to move upstream on the surface of the model, and the frequency of the second-mode instability also increased as the boundary-layer thinned, but the main features of the growth and breakdown of the second-mode instability remained similar. For all experimental cases with a smooth wall, a second-mode wave was measured growing in the streamwise direction [42, 43]. Figure 5.2 (left) shows results of a typical power spectral density (PSD) of the second-mode growth and breakdown. During this process, the second-mode bandwidth broadens. On average, a maximum second-mode fluctuation magnitude of about 30% was measured prior to the decrease in the pressure fluctuations as breakdown occurred [42, 43]. After the second-mode wave broke down, the pressure fluctuations dropped to less than 10% of the mean surface pressure through the aft end of the model [42, 43]. PSE calculations in section 5.3 seek to explain the underlying physics which appear to be responsible for this broadening.

Figure 5.2 (right) compares the location of the second-mode pressure features with an average heat-transfer profile extracted along streamlines through the streaks of heating at a $\mathrm{Re}_\infty \approx 11 \times 10^6/\mathrm{m}$. This is similar to the conditions to the direct numerical simulation (DNS) of fundamental breakdown on the flared cone performed by Hader at the University of Arizona [42, 43]. The maximum pressure fluctuations and heat transfer both occur within a laminar boundary layer. Once breakdown begins and the heating rate decreases, the first increase in intermittency occurs indicating that transition to turbulence has begun [42, 43]. Around 5 cm downstream from where the first increase in intermittency occurred, an almost fully turbulent boundary layer is measured and heating rates have increased to similar values as the upstream set of streaks. Lastly, the azimuthal wavenumber was found to be 78 for both the upstream

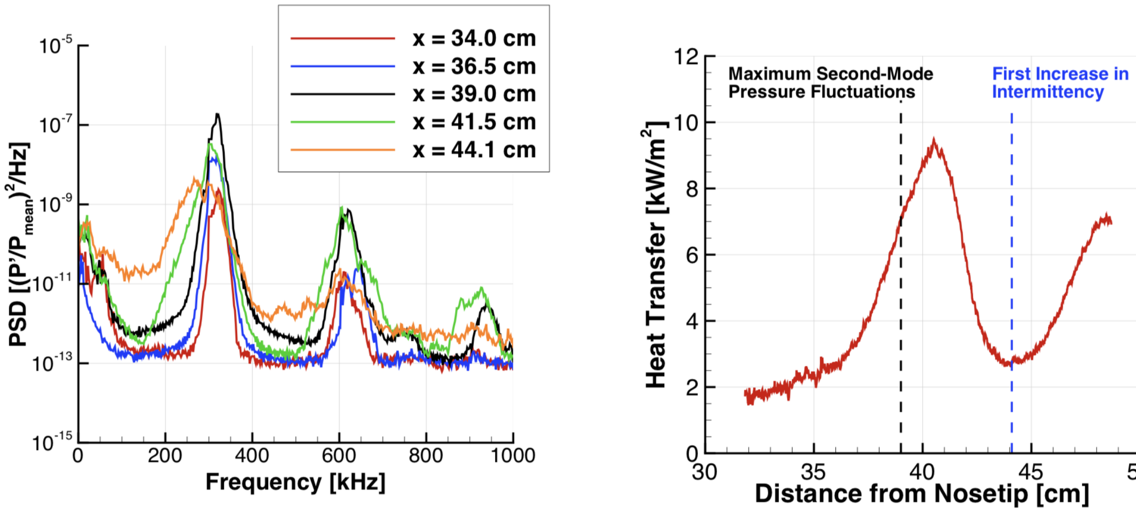

Figure 5.2: (Left) PSDs in the streamwise direction showing the non-linear growth of the second-mode instability. (Right) Streamwise heat transfer profile aligned with the streaks of heating (used with permission) [42, 43].

and downstream sets of streaks [42, 43].

5.2.2 Collaborator DNS Analysis [42, 43]

This section represents results and contributions by collaborators: Hader and Fasel [42, 43]. High-quality direct numerical simulations (DNS) were conducted to investigate the underlying behavior of the streak pattern observed the cone's surface. For DNS analysis, the mode is defined as: (n,m) is used for shorthand notation of (n$\cdot f_{primary}$,m$\cdot k_{c,domain}$), where $f_{primary}$ is the primary instability or wave frequency and $k_{c,domain}$ is the azimuthal domain wave number [42, 43]. The primary wave frequency is chosen as the frequency leading to the highest N-factors in the linear regime. For breakdown simulations only, a spanwise section of the cone is considered in the azimuthal direction.

A "controlled" set of disturbances were introduced into the computational domain through a blowing and suction slot in the wall [42, 43]. Therefore, these simulations are referred to as controlled breakdown simulations, as opposed to the natural

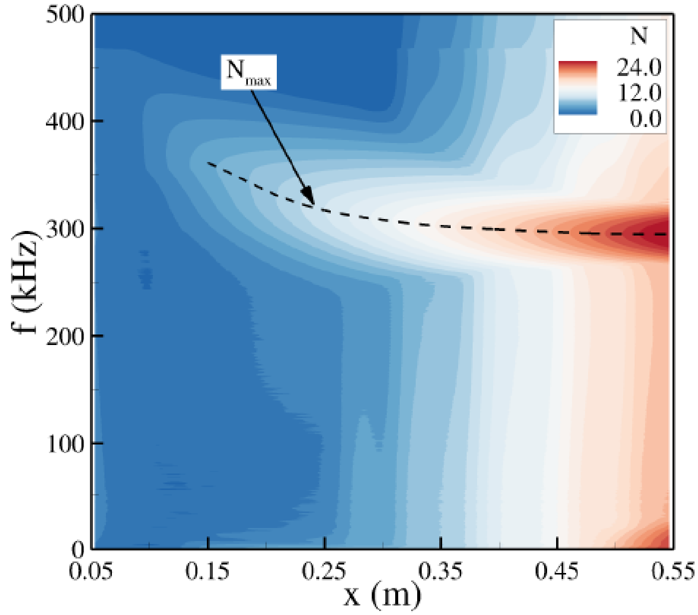

Figure 5.3: N-Factors plotted on frequency vs streamwise location, M = 6, P_0 = 965.27kPa, T_0 = 420K (used with permission) [42, 43].

breakdown observed in the BAM6QT experiments. Furthermore, previous simulations have shown that the fundamental breakdown is a surmised to be a route to transition [42, 43]. This type of breakdown is initiated by forcing a large amplitude, two-dimensional primary wave, mode (1,0), and a small amplitude, three-dimensional secondary wave, mode (1,1), with the same frequency ($f_{primary}$) as the primary wave [42, 43]. So, in order to initiate a controlled breakdown DNS, the primary wave frequency and the azimuthal wave number of the secondary wave have to be determined apriori [42, 43].

The primary wave frequency is determined by mapping out the primary instabilities using short duration pulse simulations. Next, experimental results corresponding to: p_0 = 965.27kPa, T_0 = 420K were used for the controlled breakdown simulation [42, 43]. Then, N-factors for these conditions, are shown in figure 5.3 on the right hand side where the maximum N-factor is at 300kHz [42, 43]. The azimuthal wave number of the secondary wave was chosen based on a parametric study of the secondary instabilities [42, 43]. Hader & Fasel 2017 showed that for BAM6QT conditions, the fundamental resonance is stronger compared to the subharmonic resonance [73]. In order to determine the azimuthal wave number (k_c) leading to the strongest fundamental resonance onset, low resolution, azimuthal direction DNS were carried out.

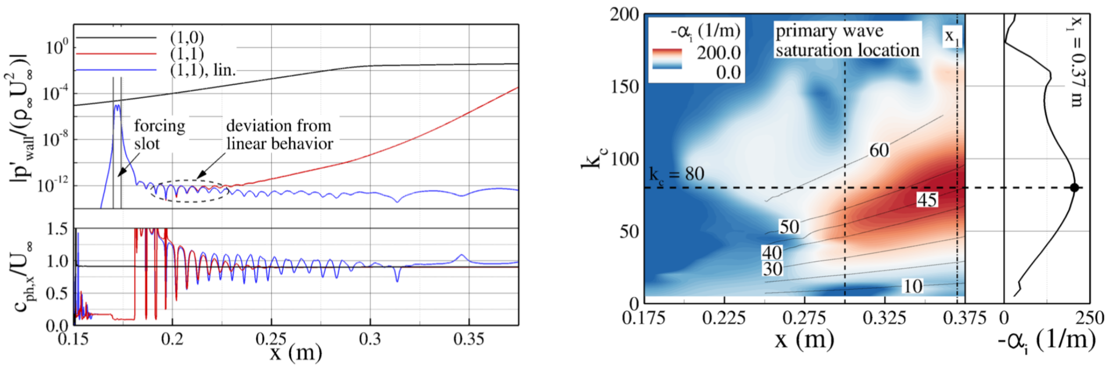

Figure 5.4: (Left) Wall pressure disturbance amplitude and phase speed development for a fundamental resonance scenario. (Right) Spatial growth rate of the secondary disturbance wave in downstream direction for varying azimuthal wave numbers (k_c) for the fundamental resonance onset (used with permission) [42, 43].

In order to understand wave resonance consider the following. When the primary wave resonates, it grows exponentially until it reaches a sufficiently large amplitude, then it saturates as shown in figure 5.4 (left) [42, 43]. Next, phase-speed locking occurs between the primary and the secondary waves which causes the secondary ones to deviate from their linear behavior. In controlled breakdown simulations, the nonlinear breakdown of the disturbance waves that are dominant in the resonance onset is captured by the azimuthal wave number of the most amplified secondary disturbance wave.

Next, fundamental resonance onset calculations were conducted for the range of azimuthal wave numbers: $k_c = 5$ to $k_c = 200$ with $\Delta k_c = 5$ [42, 43]. As such, the spatial growth rate and the wave angle are shown in figure 5.4 (right), with strong resonance observed at distance of 0.3m corresponding to the strongest fundamental resonance at azimuthal wave numbers of $k_c \approx 80$. This wave number will shift to larger values moving downstream for which the resonance onset is at its strongest. Nonetheless, the secondary wave angle remains nearly constant at $\psi \approx 45°$. Thus, the parameters for DNS were as follows: frequency: f = 300kHz was chosen for primary and secondary waves, the azimuthal wave number of $k_c = 80$ for the secondary wave. Continuing, the grid points used were: $n_x = 4750$ in the streamwise, $n_y = 350$ in the wall normal, and $n_z = 95$ in azimuthal directions [42, 43].

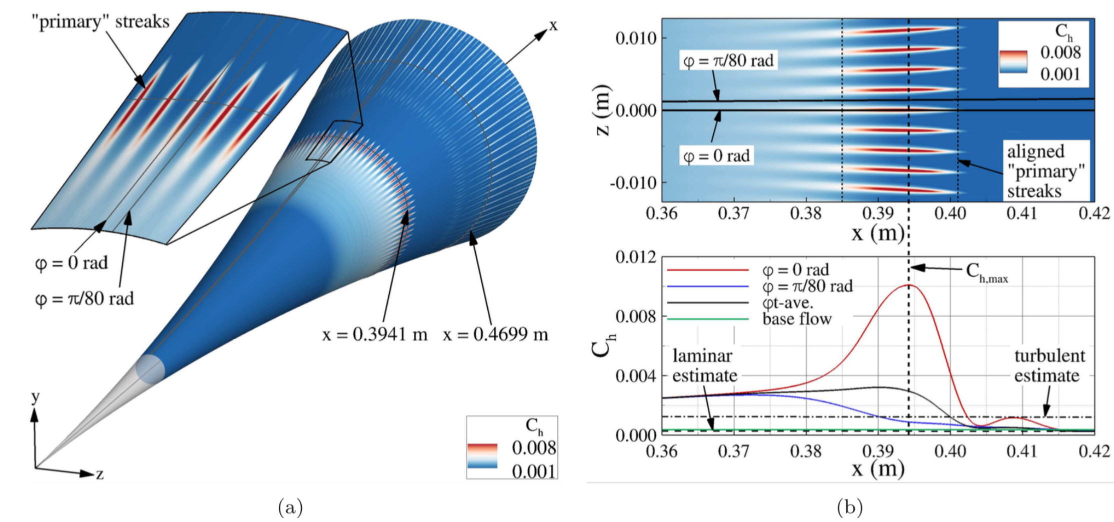

Figure 5.5: (a) Time-averaged Stanton number on the surface of the cone surface and location markers indicating data extraction locations for further analysis. (b) Zoom-in of “primary” streaks including overshoot for the turbulence estimation of the Stanton number at ≈ 0.3941m. (used with permission) [42, 43].

Next, the time-averaged Stanton number results were determined to show the heating streaks. 5.5 through 5.7 [42, 43]. At first, the Stanton number on the cone's surface is mostly uniform just before the appearance of the primary streaks. This is the numerical analogy to the hot-cold-hot streak pattern observed in the experiments [42, 43]. A relatively small variation of the azimuthal Stanton number was observed until the primary streaks appeared. Then, the primary streaks disappeared and the Stanton number became uniform again in azimuthal direction before the flow began to break down and a secondary streak pattern appeared, see figure 5.5(a). The secondary streaks are weaker than the primary streaks, consequently, the peak surface heating of the secondary streaks where breakdown occurs, was much smaller than the upstream primary streak region [42, 43]. In figure 5.5(b) a zoom-in of the primary streaks are shown in the upper half, and in the lower half the time-averaged streamwise development of the Stanton number. Curves depicting a laminar and a turbulent estimate are included per White (2006) [12]. Before the primary streaks appear, the curves for the Stanton number develop for different azimuthal locations. Further, the azimuthally averaged Stanton number is nearly idential. Once the primary streaks begin to appear, the curves diverge from one another, yet converge again further downstream when the streaks disappear. This behavior indicates that the appearance, disappearance, and reappearance of the streaks is linked to three-dimensional modes [42, 43].

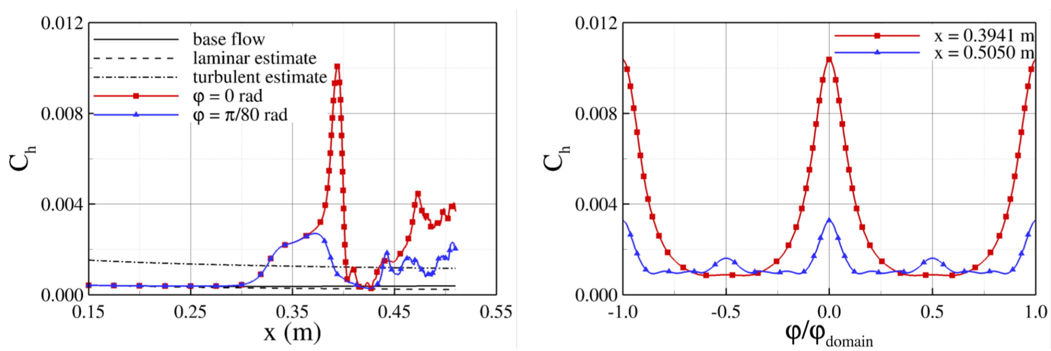

(a) (b)

Figure 5.6: (a) Stanton number coefficient vs streamwise distance along cone. (b) Stanton number coefficient vs azimuthal angle around cone (used with permission) [42, 43].

Figure 5.6 shows the downstream development of the time-averaged Stanton number, with the variations of the normalized azimuthal direction are shown periodically [42, 43]. The data for $\varphi = 0$ radians shows a very high peak at ≈ 0.39m, and a smaller peak at ≈ 0.5m downstream, and for $\varphi = \pi/80$ radians does not peak as high as the 0 radian case. Furthermore, the secondary streak location at 0.5m does not have as high of a Staton number as the primary streak location. In figure 5.7, cross-sections of the primary (figure 5.7(a)) and secondary (figure 5.7(b)) streaks locations

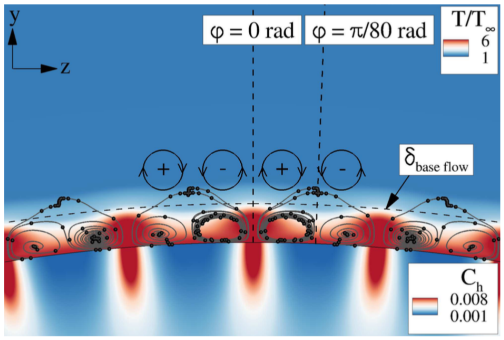

(a)

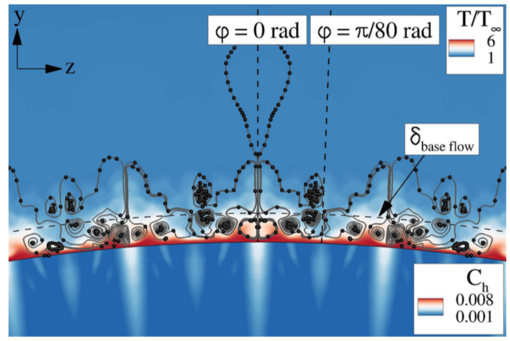

(b)

Figure 5.7: (a) Time averaged temperature, Stanton number on the surface of the cone, and streamlines contour plot at 0.3941m downstream. (b) At 0.4699m downstream (used with permission) [42, 43].

are shown [42, 43]. Seen were counter-rotating vortices which pulled cooler air from the freestream and trapped it next to the wall between the vortices heating it up right above the streak location. Subsequently, it was shown by Hader and Fasel that when these vortices detach from the wall, the primary streaks fade where the cold region is, and the Stanton number returns to the laminar amounts [74]. Then, the disturbance nonlinearities reattached the streamwise vortices, and the streaks reappear, hence the hot-cold-hot streak pattern observed [42, 43].

5.2.3 Collaborator Comparison of Experiments and DNS [42, 43]

This section represents results and contributions by collaborators: Chynoweth, Schneider, Juliano, Wheaton, Hader and Fasel. The aforementioned experimental and DNS results were compared in order to better understand the hot-cold-hot streak formation on the flared cone. Figure 5.8 shows an overlay of the time-averaged Stanton number DNS ($Re = 10.8 \times 10^6/m$) and the TSP image from the experiment ($Re = 11.0 \times 10^6/m$) with good qualitative comparison [42, 43]. Moreover, the DNS produced 80 streaks, and an extrapolated count of 78 streaks were found from the experiment. Figure 5.9 shows quantitative comparisons of the DNS and experimental results. The left hand side figure shows Stanton number vs streamwise distance. The

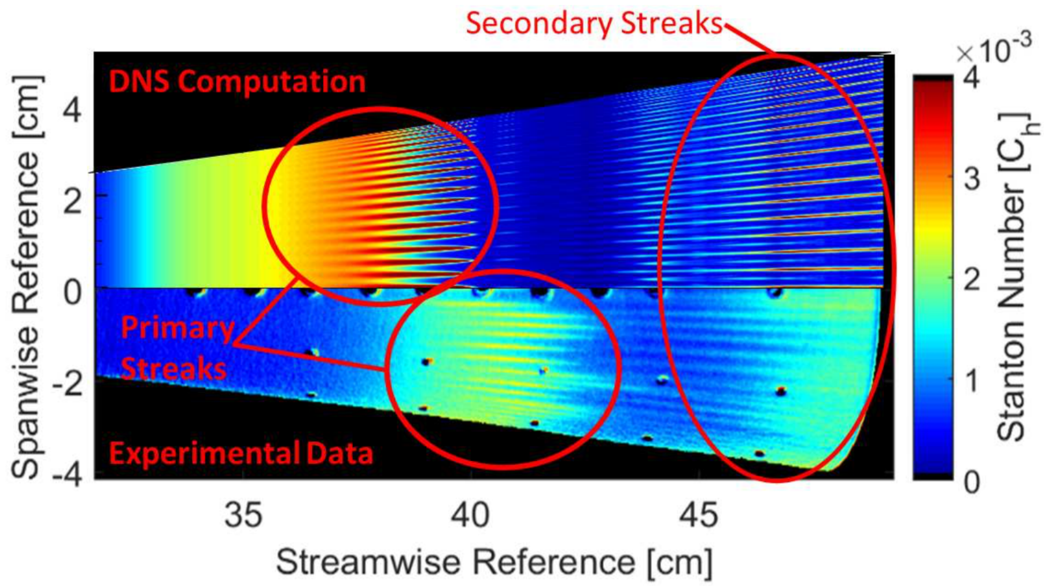

Figure 5.8: Stanton number of DNS compared to experimental TSP results of streaks (used with permission) [43].

DNS starts to deviate from the experiment at roughy 30cm, and has the very high overshoot at roughly 39cm, whereas the experiment does not have such an overshoot. After the overshoot, the DNS trend drops to levels much closer to the experimental data. The right hand figure shows pressure fluctuation vs streamwise distance. Again, there is a high overshoot in the DNS compared to the experiments, and the trend matches again starting about 40cm downstream. The reason for the overshoots is that in order to force the DNS to transition, the controlled disturbance is forced as described in the earlier section which is fundamentally different than the natural transition process in the experiment [42, 43].

5.3 Stability Analysis Results - NATO AIAA SciTech 2018 [42]

5.3.1 Comparison of Experiments and NPSE

As noted by Kuehl (2017), the wave packet formulation accounts for proper re-distribution of energy between finite-bandwidth disturbances that the traditional

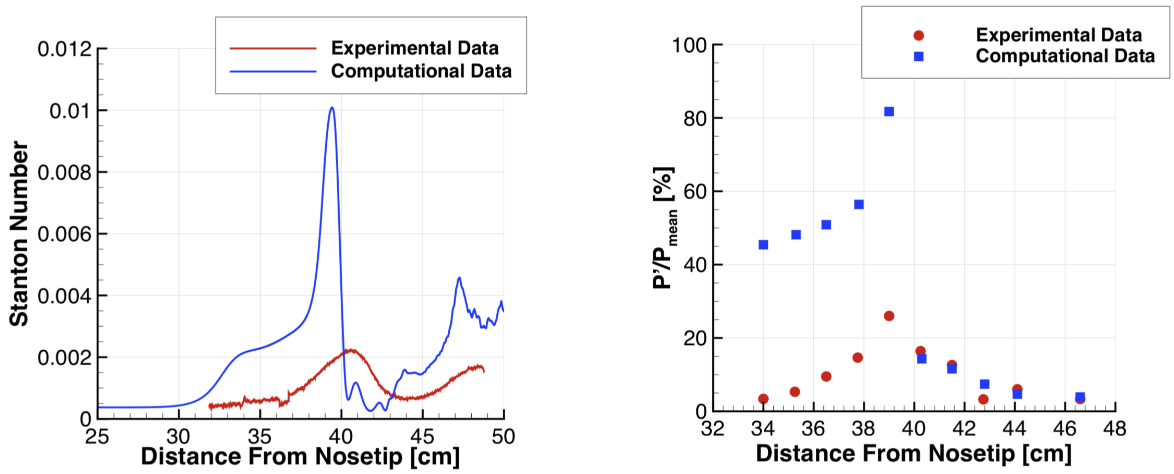

Figure 5.9: (Left) Stanton number vs streamwise distance, DNS vs experimental results; (Right) Pressure fluctuation differences vs streamwise distance, DNS vs experimental results (used with permission) [43].

PSE approach does not [7, 42]. The redistribution of energy onto the side-lobes results in larger total disturbance amplitudes than those predicted by traditional PSE [42]. Figure 5.10 shows calculations for 2-D second-modes initialized with amplitudes of 1×10^{-6} (upper), 1×10^{-7} (middle) and 1×10^{-8} (lower) based on normalized temperature disturbance amplitude [42]. Unlike experiment and to a lesser extent in DNS analysis, PSE is an approximate method in which assumptions are made with the intent to isolate and study specific physical processes [42]. In this case, the wave packet methodology has been utilized to account for energy redistribution into side-lobes, to model spectral broadening [42]. In the traditional PSE case, the 275 and 325 kHz side-lobes are trivially amplified [42]. However, notice that due to the wave packet energy redistribution, those side-lobes grow to significant amplitude [42]. These side-lobes model the spectral broadening observed in experiment [42]. Spectral broadening is found to begin between 0.38 - 0.4m downstream from the cone tip in the 1×10^{-6} case, between 0.41 - 0.44m in the 1×10^{-7} and between 0.44 - 0.47m in the 1×10^{-8} case [42].

The experimental results suggest spectral broadening begins between 0.4 - 0.44m

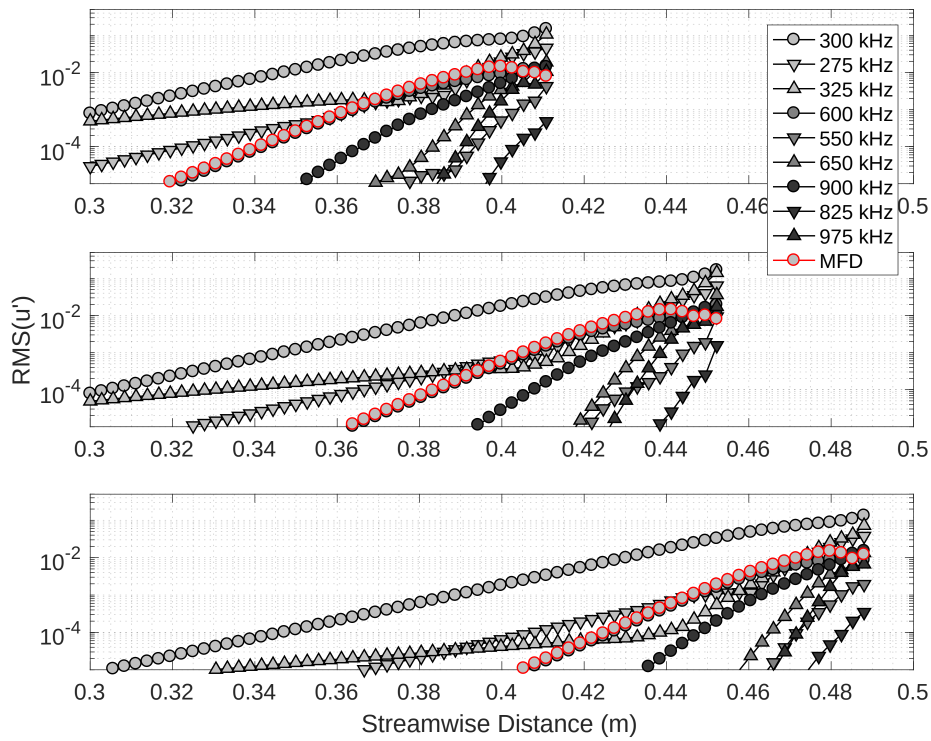

Figure 5.10: NPSE calculations of second-mode growth on the Purdue flared cone for initial disturbance amplitudes of 1×10^{-6} (upper), 1×10^{-7} middle and 1×10^{-8} (lower).

downstream of the cone tip, which appears consistent with initial disturbance amplitude of 1×10^{-7} or slightly larger [10, 42]. Figure 5.11 provides a closer look at this case. The left panels show non-dimensional RMS streamwise velocity and pressure disturbances for individual PSE modes, while the right panels show total amplitude of the primary 300 kHz mode plus the side-lobes. The primary mode reaches around 16% (4% pressure) amplitude based on disturbance streamwise velocity with side-lobes near 15% and 7% (4% and 1% pressure), resulting in a total disturbance amplitude of 38% (9% pressure). The trends in these results appear to be roughly consistent with the experimental results: First, weak spectral broadening is initiated around 0.41m. Next, averaged heat flux (or skin friction coefficient), which is associated with the mean flow distortion mode peaks and then begins to decay (in this case around 0.44m). Finally, side-lobes reach amplitudes comparable with the primary disturbance.

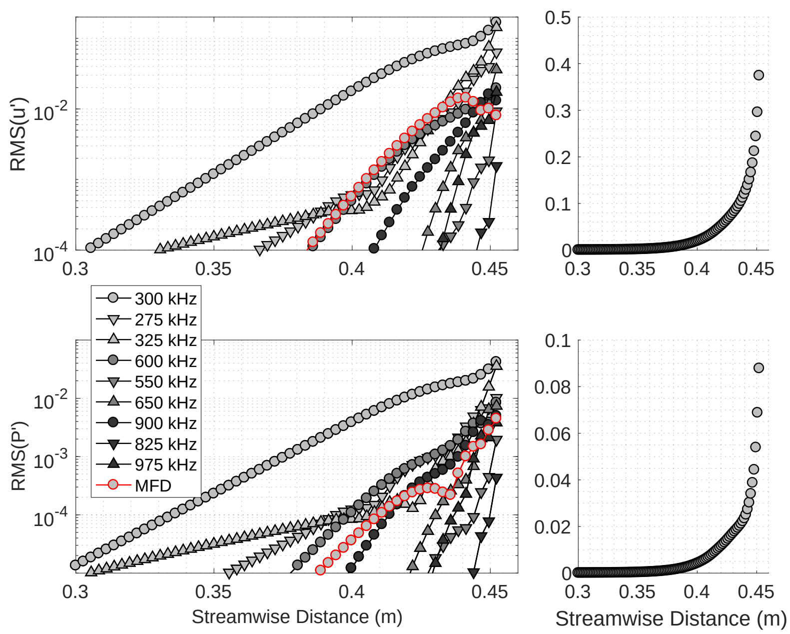

Figure 5.11: NPSE calculations of second-mode growth on the Purdue flared cone for initial disturbance amplitude of 1×10^{-7}. Plotted in the left column are disturbance mode RMS amplitudes of streamwise velocity (top) and pressure (bottom). The right column shows total disturbance amplitude of the primary mode plus both side-lobes.

The agreement between these PSE trends and experimental results is encouraging and suggest PSE is a viable tool for studying the nonlinear pre-transitional zone. However, PSE is an approximate method and at the current level of approximation uncertainly remains. Most notably in the total disturbance amplitude estimates. Based on Chynoweth (2015), the PSE estimates are roughly 50% of the experimental values [10, 42]. The results of Kuehl et al. (2014) suggest the total disturbance amplitude will be sensitive to number of modes utilized to represent the disturbance and preliminary results suggest sensitivity to the choice of side-lobe frequencies [24]. However, resolution of this inconsistency will require further research, however in the present case, it is likely that the neglect of vortical and oblique disturbances has affected the energy transfer associated with the K-type breakdown. In the traditional PSE case, inclusion of oblique and vortical disturbances is straight forward, however, in the wave packet formulation their inclusion has not yet been achieved but is ongoing research. Evidence for the importance of vortical disturbances, beyond the K-type energy transfer, was provided by Kuehl and Parades [22, 42]. It was shown that vortical modes distort the mean flow and fundamentally alter the second-mode behavior from 1-D disturbances to fully 2-D by modifying the acoustic waveguide in which the second-modes travel.

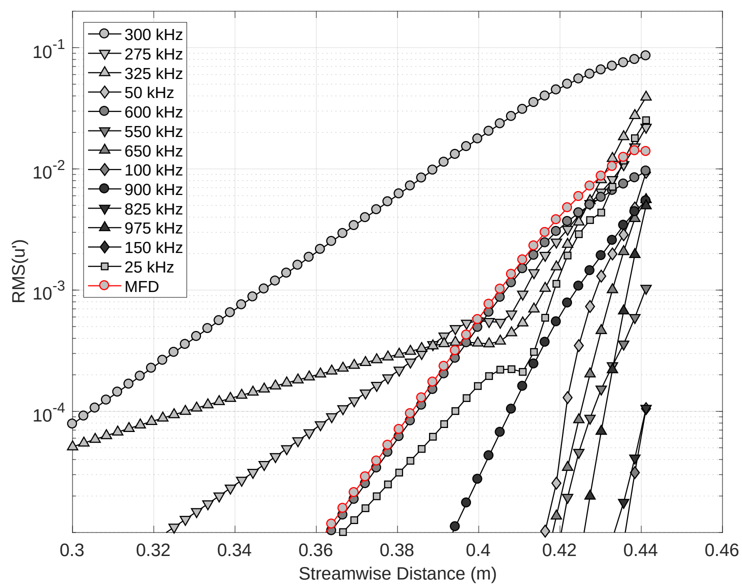

Figure 5.12: NPSE calculations of second-mode growth on the Purdue flared cone for initial disturbance amplitude of 1×10^{-7} with the inclusion of a low frequency disturbance.

Figure 5.12 illustrates a PSE calculation that includes a low frequency disturbance corresponding to the difference between the primary disturbance frequency and the side-lobe frequencies. Again, it is observed that after the spectrum broadens (after side-lobes emerge), that the low frequency disturbance experiences significant growth. In this case, the low frequency disturbance exceeds 2% amplitude. In fact, these result suggest the opposite: that low frequency content is the result of the spectral broadening which precedes the transition to turbulence.

5.4 Stability Analysis Results - AIAA Journal of Spacecraft and Rockets [43]

5.4.1 Comparison of Experiments and NPSE

The results as published in this article were an improvement upon the conference publication results. Similar to figure 5.10, figure 5.15 shows the results of another PSE run, but with 270 and 330 kHz side-lobes, and a between initial amplitude case of 5×10^{-7}. Spectral broadening is now indicated by the shaded region enclosed by the vertical dashed lines, and is found to begin between 0.4 - 0.42m downstream from the cone tip in the 1×10^{-6} case, between 0.42 - 0.44m in the 5×10^{-7}, and between 0.44 - 0.46m in the 1×10^{-7} case [43].

Peak disturbance amplitudes of approximately 30% based on normalized pressure experimental results were found as shown in figure 5.14 as shared by Purdue [11, 43]. This is consistent with the NPSE calculated amplitudes which reached into the 20-40% range for those initial amplitude cases that exhibit a similar onset of spectral broadening (figure 5.16, left panel). Another useful comparison between the experimental and numerical data is to consider the amplitude ratio between the primary disturbances (primary mode and side lobes) and the first harmonics of those modes (i.e. primary/harmonic). Similar to the consideration of spectral broadening onset, this comparison provides information regarding the proper distribution of energy between modes in the numerical scheme.

Figure 5.13 and table 5.1 from streamwise locations of roughly 36.5 to 39 cm indicate an estimate for the onset of spectral broadening experimentally [11]. The experimental results also suggest spectral broadening begins between 0.4 to 0.41.5 m downstream of the cone tip, which appears consistent with initial disturbance amplitudes between 1×10^{-6} and 5×10^{-7} [11]. By calculating from experimental data

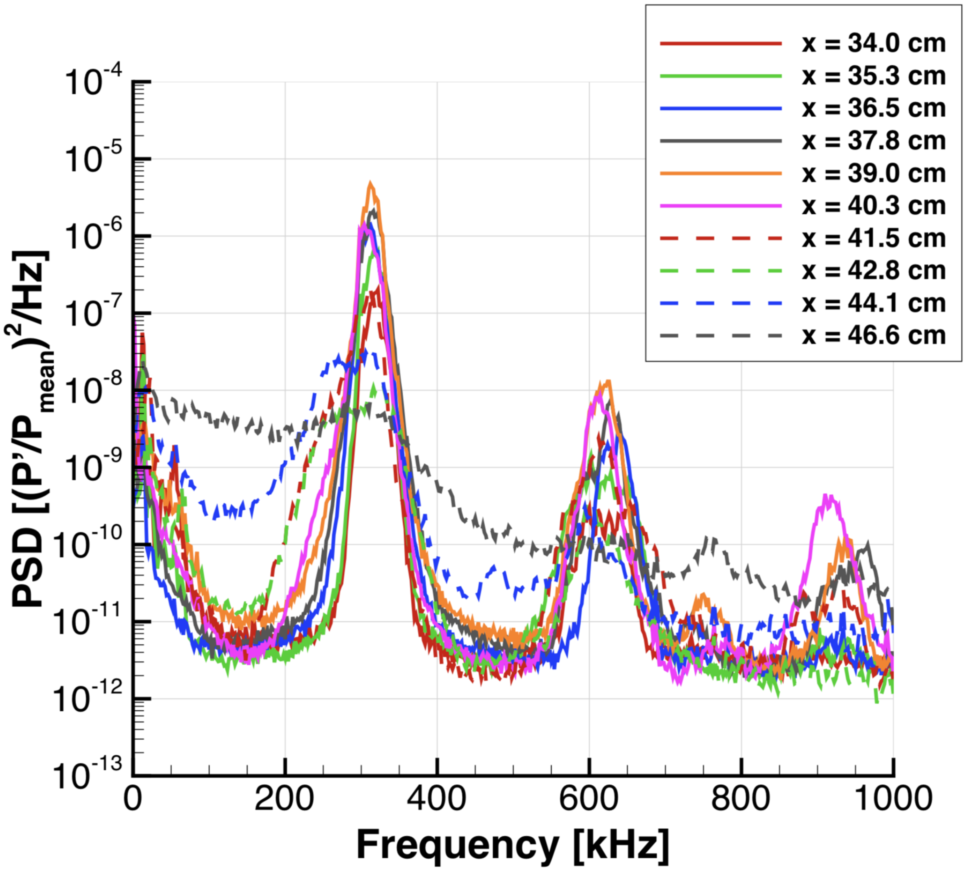

Figure 5.13: Power spectral density (PSD) of Purdue flared cone showing growth frequency range nonlinearities/harmonics, and spectral broadening and onset locations at $Re = 11 \times 10^6$ m^{-1} (used with permission) [11].

shared by Schneider and Chynoweth (see table 5.1) the primary to first harmonic amplitude ratios of approximately mid to low 20s prior to the onset of spectral broadening, dropping to mid to low teens during spectral broadening and entering the single digits shortly afterwards. As seen in figure 5.16 (right panel), the NPSE calculations recover similar amplitude ratio trends.

The agreement between these PSE trends (disturbance amplitude, onset of spectral broadening and primary to harmonic amplitude ratio) and experimental results is encouraging and suggest that PSE is a viable tool for studying the nonlinear pretransitional zone. However, PSE is an approximate method and at the current level

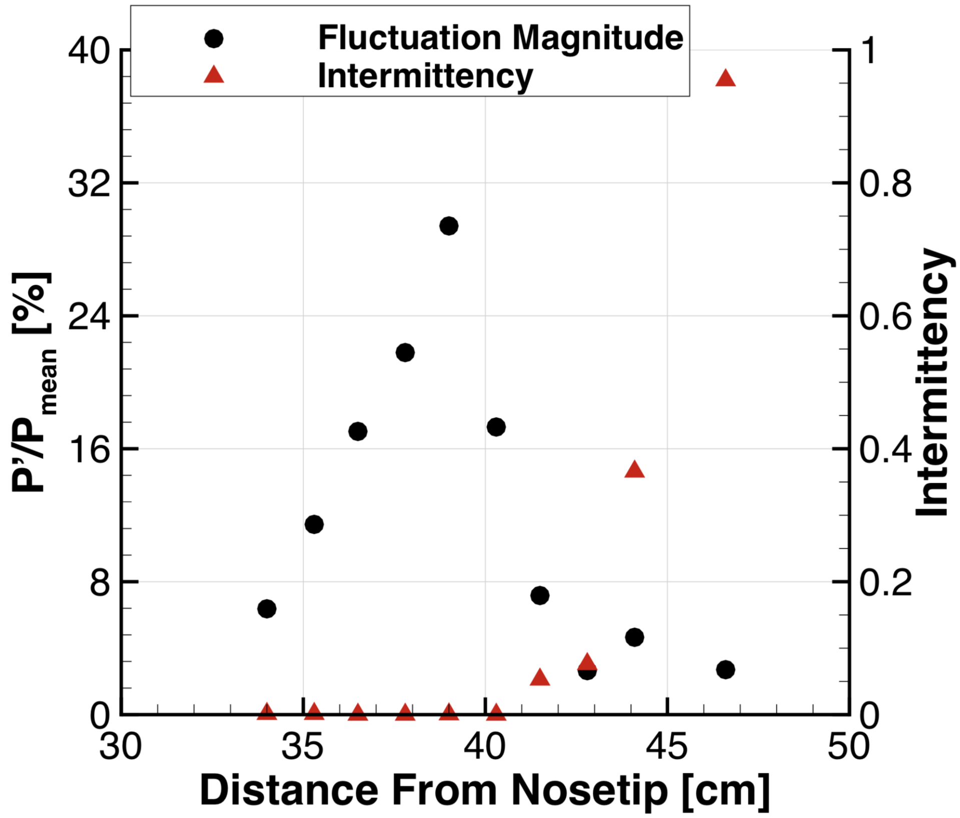

Figure 5.14: Second-mode peak amplitudes and intermittency estimated at roughly $Re = 11 \times 10^6\ \text{m}^{-1}$ (used with permission) [11].

Table 5.1: Primary Divided by 1st Harmonic Amplitude Ratio Re-tabulated by Experimental Data Shared by Schneider and Chynoweth from Purdue.

Sensor Distance [cm]	Primary / 1st Harmonic Amplitude Ratio
34	9.7
35.3	7.7
36.5	22.1
37.8	17.5
39.0	13.1
40.3	7.8
41.5	6.8
42.8	7.2

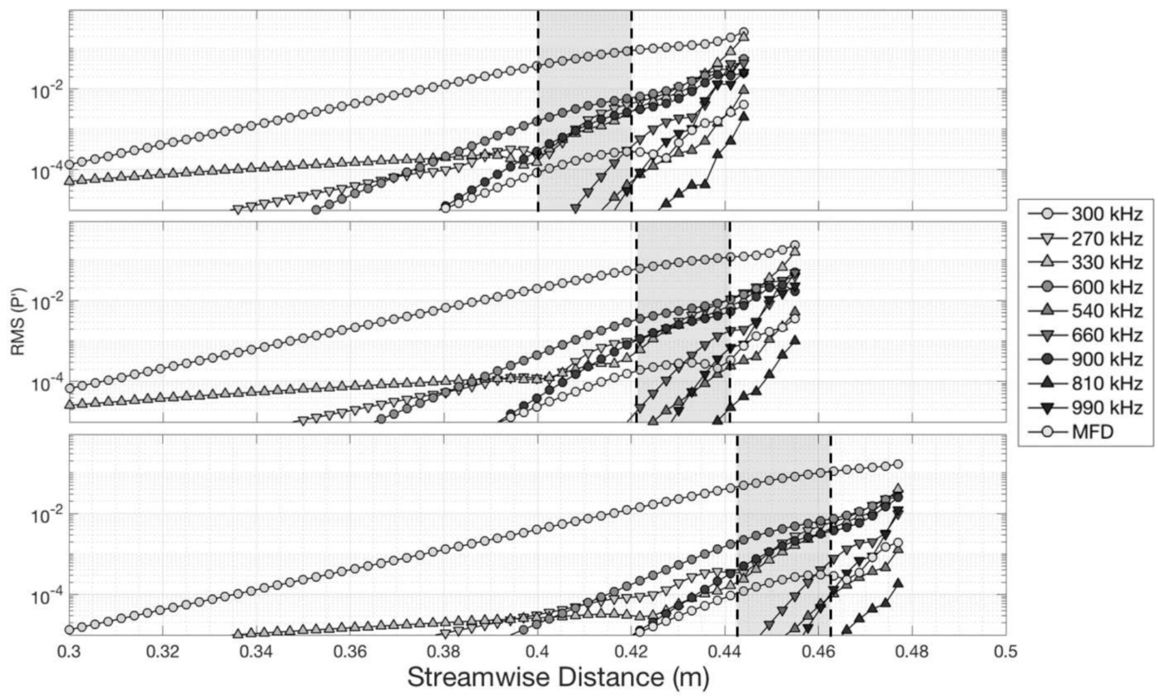

Figure 5.15: NPSE calculations of second-mode growth on the Purdue flared cone for initial disturbance amplitudes of 1×10^{-6} (upper), 5×10^{-7} middle and 1×10^{-7} (lower). The grey shaded region indicates the onset of spectral broadening.

of approximation uncertainty remains. The results of Kuehl et al. suggest the total disturbance amplitude will be sensitive to the number of modes utilized to represent the disturbance and preliminary results suggest sensitivity to both the number of side-lobes and their chosen frequency distribution [24]. This can be seen in figure 5.17 where different distributions of side-lobes are considered. Notice that despite the total disturbance amplitude being the same in each case, variations in both amplitude and distribution remain. The resolution of these uncertainties will require further research, however in the present case, it is likely that the neglect of vortical and oblique disturbances has the most significant effect on numerical-experimental comparison via the energy transfer associated with the K-type breakdown scenario. In the traditional PSE case, inclusion of oblique and vortical disturbances is straight forward. In the wave packet formulation, their inclusion is ongoing research. In addition, evidence for the

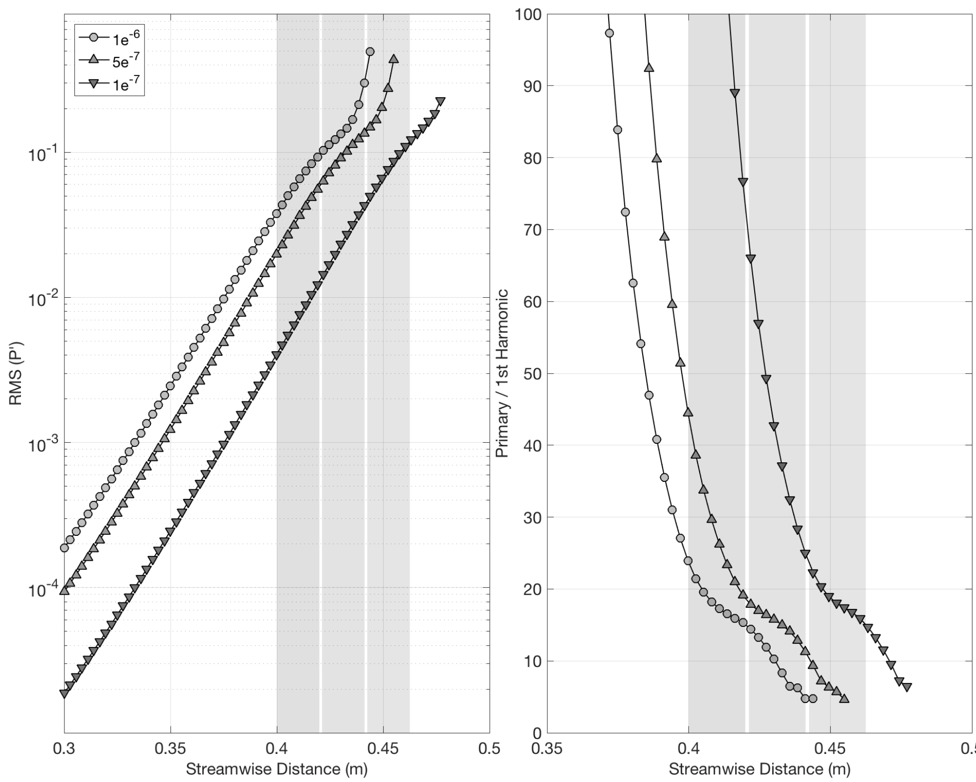

Figure 5.16: NPSE calculations for 1×10^{-6}, 5×10^{-7} and 1×10^{-7} initial disturbance amplitudes. Left: Total primary disturbance amplitude (primary plus side-lobes). Right: Primary to first harmonic amplitude ratio. Grey shaded region indicates the onset of spectral broadening.

importance of vortical disturbances beyond the K-type energy transfer was provided by Kuehl and Parades [22]. It was shown that vortical modes distort the mean flow and fundamentally alter the second-mode behavior from 1-D disturbances to fully 2-D by modifying the acoustic waveguide in which the second-modes travel. This result is consistent with the recent thermoacoustic interpretation of second-mode instability provided by Kuehl [8].

Similar to the Scitech results, figure 5.18 illustrates a PSE calculation that includes a low-frequency disturbance. These results again suggest that the emergence of low-frequency content in boundary layer transition measurements is not a result of

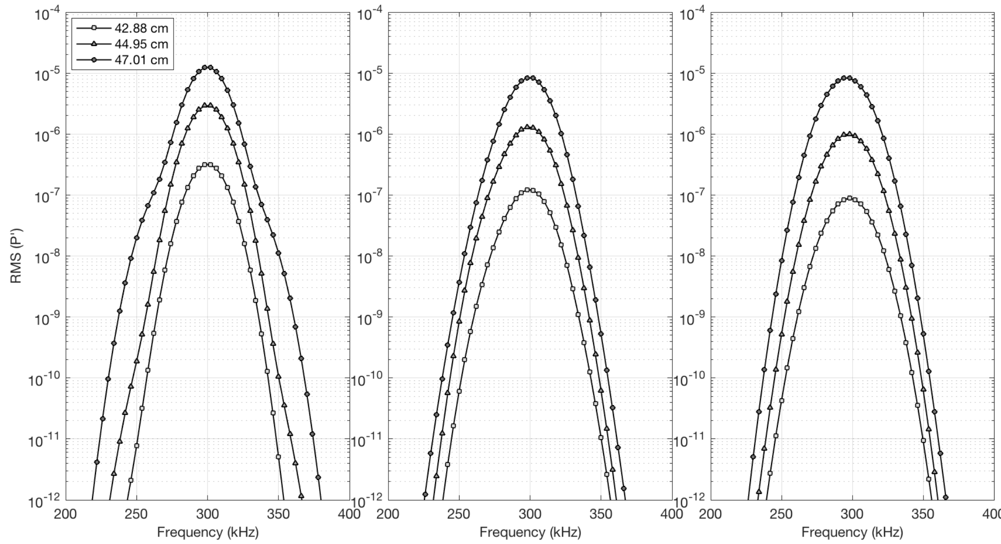

Figure 5.17: NPSE calculated disturbance spectrum at three different locations spanning the onset of spectral broadening for initial disturbance amplitude of 5×10^{-7}. Left: 3 modes separated by 30kHz. Middle: 5 modes separated by 15kHz. Right: 7 modes separated by 10kHz. Total disturbance amplitude (primary plus side-lobes) is the same in each case.

"tunnel noise", but instead are a fundamental consequence of finite-bandwidth primary mode disturbances and spectral broadening, which precedes transition.

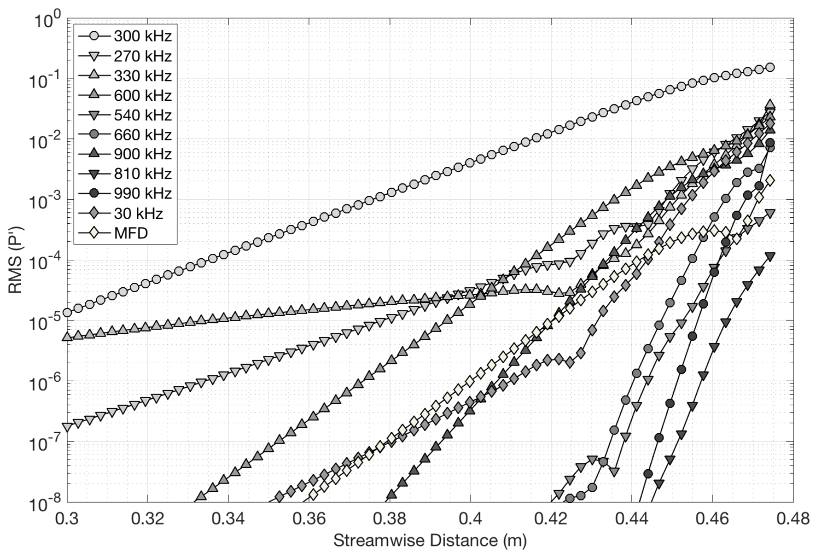

Figure 5.18: NPSE calculations of second-mode growth on the Purdue flared cone for initial disturbance amplitude of 1×10^{-7} with the inclusion of a low-frequency disturbance.

Chapter 6

NONLINEAR DYNAMICS OF SECOND MODE WAVES ON A HYPERSONIC FLARED CONE

6.1 Introduction & DNS Basic State [45]

In collaboration with Victor Sousa and Dr. Carlo Scalo of Purdue, this chapter presents a comparison of acoustic DNS results they calculated using CFDSU at Purdue, and the JoKHeR PSE solver at University of Delaware. Again, the Purdue flared cone is considered at Re/m $= 10.8 \times 10^6$. The details are listed in table 6.1. CFDSU solves the Navier-Stokes equations using a sixth-order compact finite difference scheme [45]. A basic state solution is generated with no perturbations, see figure 6.1. Then the DNS is fed this basic state with a perturbation, which is generated by wall suction or blowing, and the evolution of the perturbation is calculated with CFDSU. A comparison of velocity and temperature profiles are shown in figure 6.2 from the basic state solution generated by US3D and the high order solution by CFDSU.

Table 6.1: US3D Run Conditions for Basic State [45].

Run Case	Boundary	ρ_∞ [kg/m^3]	T_∞ [K]	u_∞ [m/s]	T_{wall} [K]
Re/m $= 10.8 \times 10^6$	Inflow	0.0417	51.6448	864.3102	300

6.2 Results [45]

6.2.1 NPSE and DNS Comparison

We compared the results obtained in the DNS simulations with NPSE calculations as shown in figure 6.3. The DNS was initialized with disturbance pulse amplitude

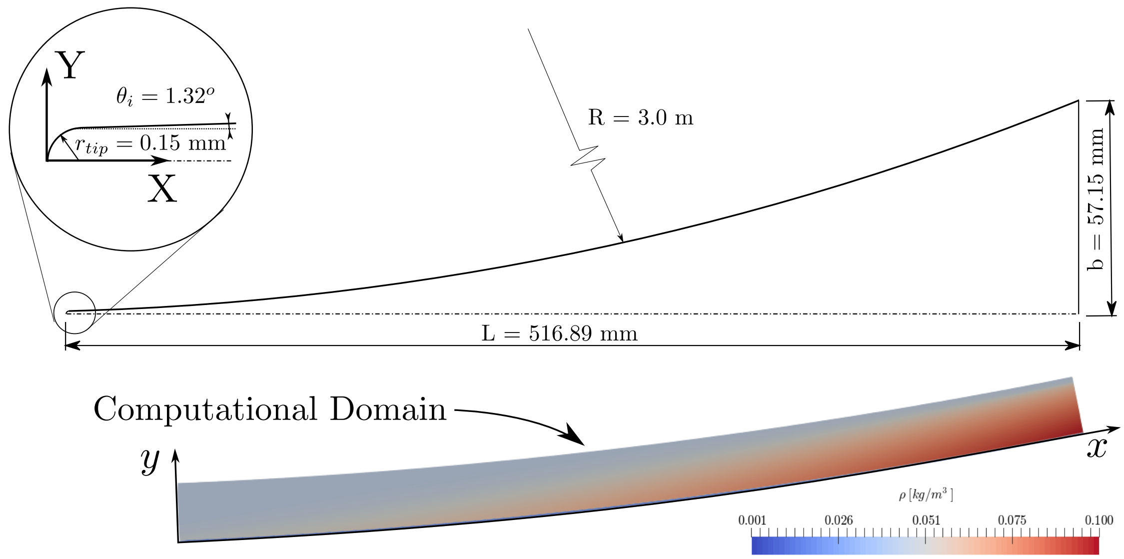

Figure 6.1: Flared cone geometry and computational domain contour plot (used with permission) [45].

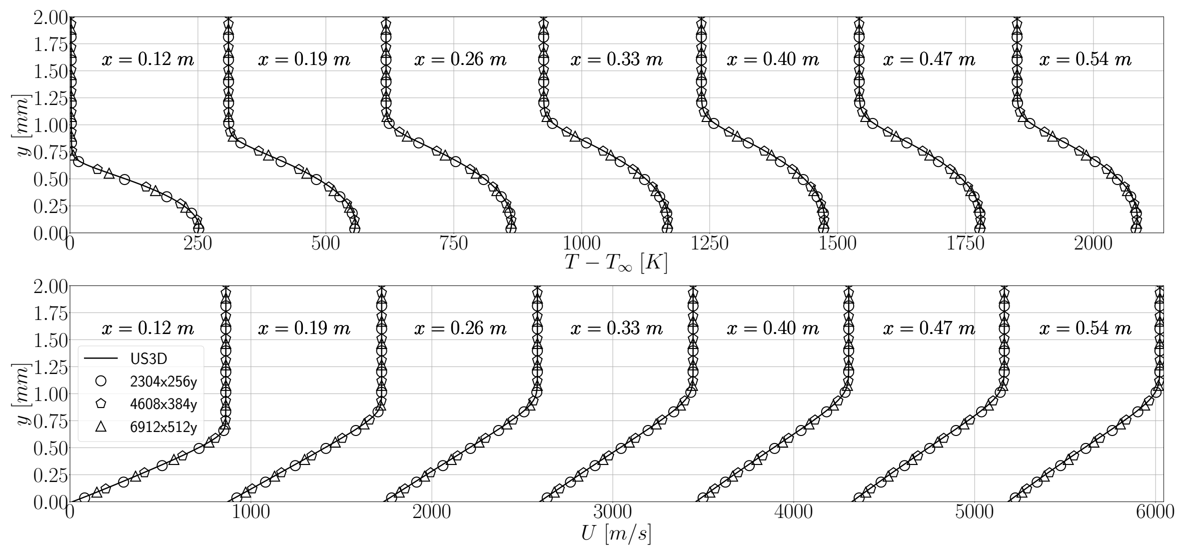

Figure 6.2: Boundary layer profiles height above the wall (y) vs temperature difference and streamwise velocity at different streamwise locations along the cone surface for the precursor and high order calculations. The solid line is US3D, and the symbols are from CFDSU simulations (used with permission) [45].

of 1.0×10^{-6} m/s for 1.67 μs. The results show that for all grids simulated, the growth rate of the primary frequency is in good agreement [45]. As the grid is refined, the estimated growth rates for the higher harmonics also start to exhibit agreement with NPSE trends. In order to capture the growth rates of the 900 kHz mode, a grid resolution of at least $n_x = 9216$ and $n_y = 640$ was required [45]. However, there is disagreement in the spatial region where harmonics become important, and in the region where saturation of the wave occurs. This is consistent with the fact that disturbances of higher frequencies need more points to be accurately resolved with a minimum numerical dissipation, and is therefore the expectation that increasing the grid resolution would produce closer matching of the results. Finally, It is worth noting that the noise floor decreases monotonically as the grid was refined.

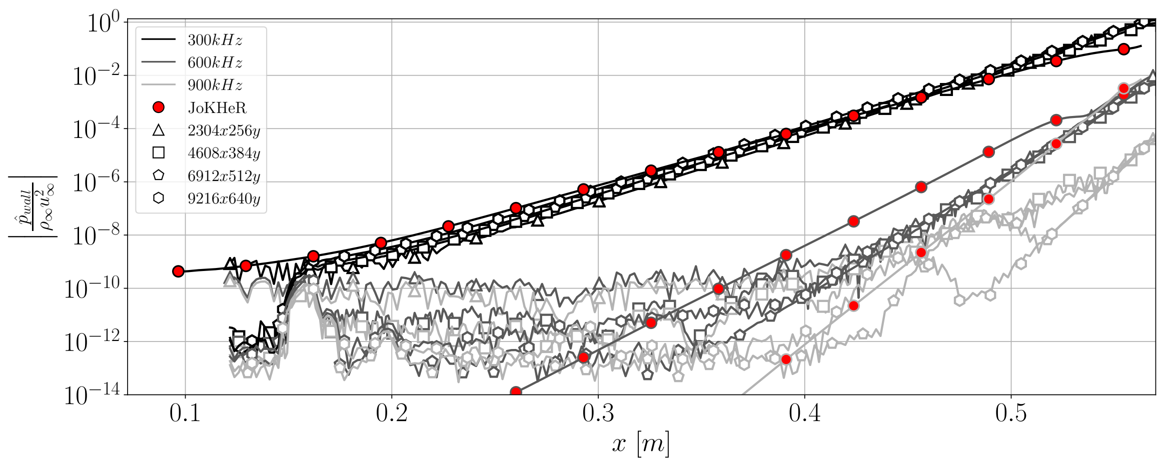

Figure 6.3: Comparison of the DNS and nonlinear PSE results (used with permission) [45].

6.3 Collaborators Results On Spectral Broadening [45]

This section represents results and contributions by collaborators: Sousa and Scalo [45]. The DNS was run again with an initial amplitude of 1×10^{-4} m/s. This was to test the moderately to highly nonlinear disturbance evolution region [45]. Figure 6.4 shows the PSD results of this case. Notice the presence of strong harmonic amplitudes, which indicates how reliant upon nonlinear effects this disturbance is [45]. Figure 6.5 shows the disturbance amplitudes vs frequency at 3 different streamwise locations. Both figures show spectral broadening as a consequence of the nonlinearities [45]. Lastly, Sousa and Scalo show a simulated Schlieren of the rope waves within this highly nonlinear disturbance region in figures 6.6 and 6.7. These rope waves appear in experimental Schlieren images, and are comparable. Note, the wavelength is roughly twice the boundary layer thickness, which is consistent with experimental results [45, 75]. Figure 6.7 shows the rope waves transformed into streamwise and wall normal components.

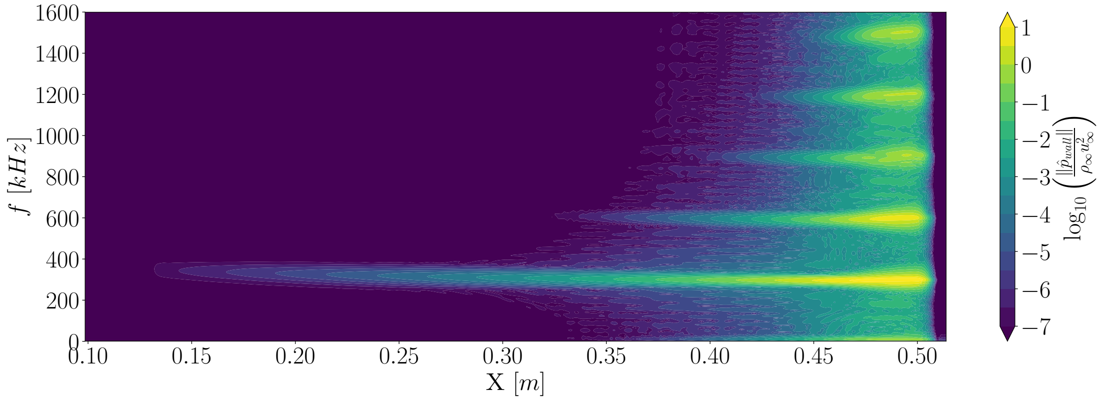

Figure 6.4: Amplitude spectrum of the pressure disturbance at the wall caused by advection with an initial amplitude of 1.0×10^{-4} m/s on a flared cone (used with permission) [45].

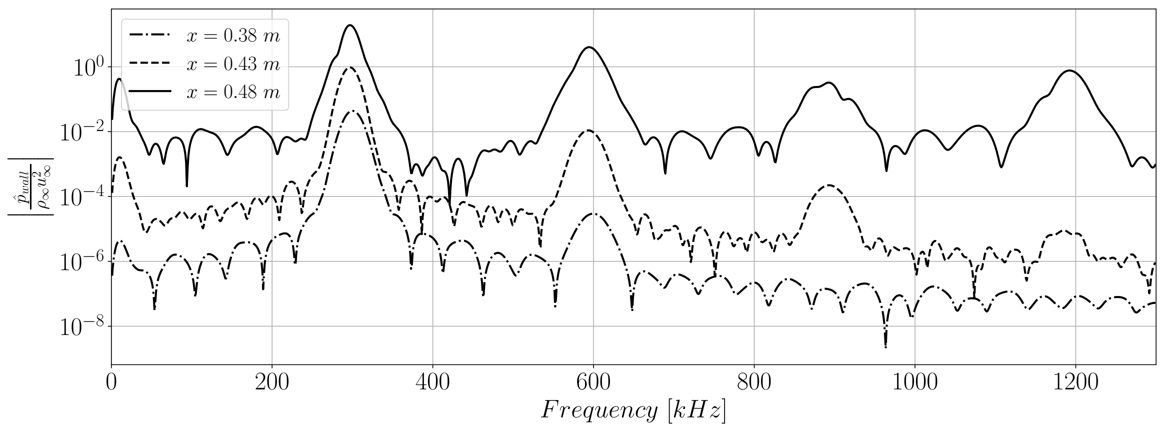

Figure 6.5: Disturbance pressure amplitude vs frequency for various streamwise positions with amplitude of 1.0×10^{-4} m/s (used with permission) [45].

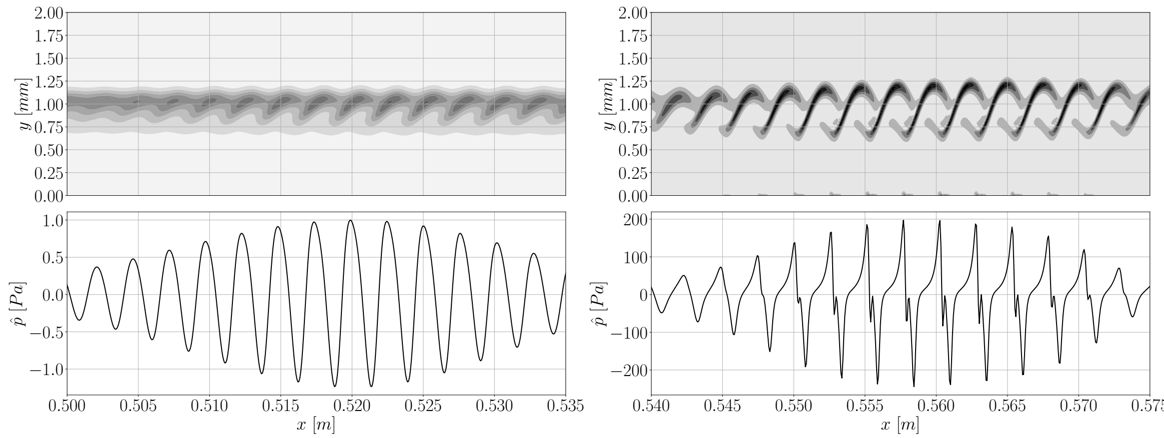

Figure 6.6: Numerical Schlieren showing "rope waves" caused by non-linear interactions between second-mode waves of high amplitude (used with permission) [45].

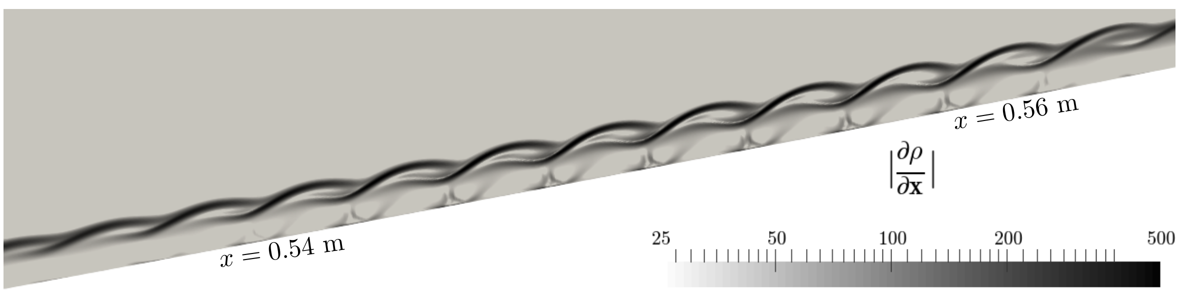

Figure 6.7: "Rope waves" at boundary layer edge towards the end of the computational domain as transformed into physical coordinates (used with permission) [45].

Chapter 7

ON THE MECHANISM BY WHICH NOSE BLUNTNESS SUPPRESSES SECOND-MODE INSTABILITY

7.1 Introduction

Recalling from section 2.3.1.3, we return to the "blunt body paradox" described by Reshotko and Tumin (2000) [29]. In this chapter, the laminar-to-turbulent transition delay with increasing nose bluntness is addressed. Specifically, the physical mechanism by which nose bluntness alters second-mode growth is addressed before attempting to understand the entire "blunt body paradox". This work represent a first step in towards understanding the critical nose bluntness at which the transition front jumps forward, which is a subject of future work. We know that the delay in transition is associated with the suppression of second-mode growth, and not associated with larger transitional N-factors as shown by Tufts and Kimmel (2017) and Juliano et al. (2015)) [34, 35]. This is because Stetson showed second-mode growth is suppressed within the entropy layer swallowing length, while outside of the entropy layer, second-mode growth was found to be unaffected by the bluntness [36] .

Further, recall that second-mode instabilities behave as resonant thermoacoustic waves trapped in an acoustic impedance well [8]. Figure 7.1 illustrates such trapping. Several phases of wall normal velocity disturbance (v', red line) and pressure disturbance (p', blue line) are shown for a second-mode oscillating within an acoustic impedance well (green line), where homogeneous acoustic impedance is given as the square root of basic state density field ($\sqrt{\bar{\rho}}$). Note, acoustic impedance in the figure has been shifted for clarity. It is clearly seen that the second-mode wave is contained within the acoustic impedance well formed between the density gradient and the vehicle wall. Further, by adopting a Lagrangian frame of reference for the inviscid acoustic energy equation, Kuehl was able to show (with the rather limiting inviscid and 1D restrictions) that this resonance is driven by thermoacoustic Reynolds stresses $\left(\left\langle \frac{d}{dy}\left(\bar{\rho}T'v'\right)\right\rangle \text{ and } \left\langle \frac{d}{dy}\left(\bar{T}\rho'v'\right)\right\rangle\right)$, where $\langle\rangle$ represent cycle averaging, over-bar indicates basic state quantities, prime indicates disturbance quantities, and y is the wall normal direction. Here this new theory will be applied to the blunt nose problem to understand the physical mechanism by which nose bluntness is able to suppress second-mode growth.

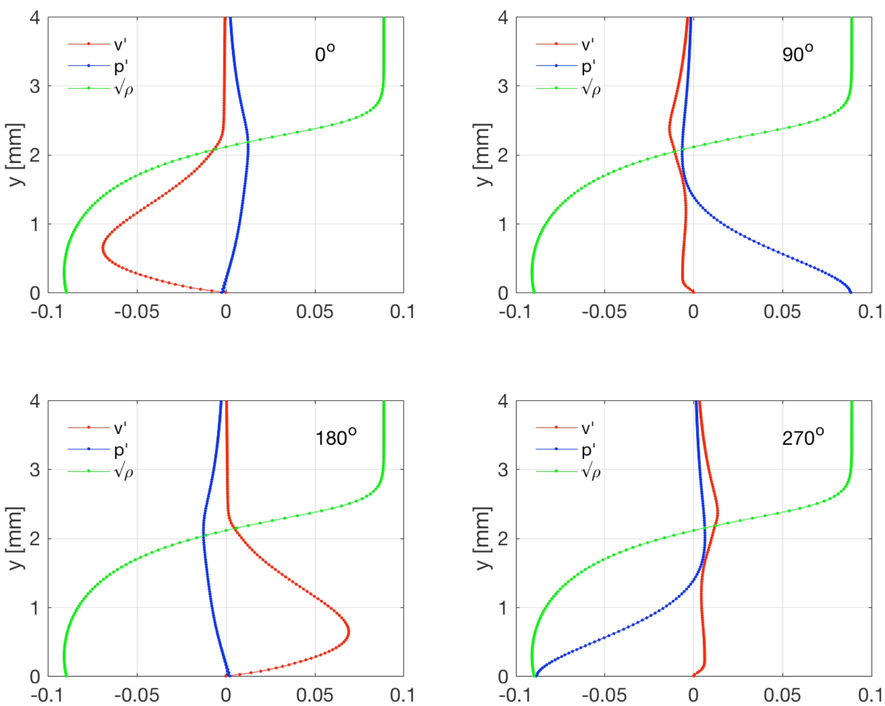

Figure 7.1: An example of second-mode wall normal velocity (v', red) and pressure (p', blue) disturbances at different phases of oscillation. Modes are calculated at 1.1m from the sharp nose tip, where the most unstable second-mode is approximately 130kHz. Superimposed on the background is the acoustic impedance ($\sqrt{\bar{\rho}}$, green) which has been shifted for clarity.

7.2 Basic State

Following the protocol established by Stetson (1983, and later Marineau et al. 2014), 7 degree half-angle, straight cone geometries of different nose bluntnesses are considered [36, 32]. The cone walls were modeled as a single, smooth body. The nominally sharp nose cone has a length along its axis of 1.6m, which is used as the reference length for the remaining cones. With a 7 degree half-angle, the base half-width is 196.45mm which was held constant in each case. The nose radii considered are: 0.15mm (sharp), 3.556mm, 5mm, 9.525mm, 12.7mm, and 25.4mm (figure 7.2). Steady, laminar basic state solutions were obtained with US3D. US3D is a CFD software package specifically designed for high-speed flows which uses the finite volume method to solve the compressible Navier-Stokes equations. Moreover, US3D incorporates high order solving schemes, various viscosity and gas properties, and other physical aspects which help to create high accuracy solutions [66, 67, 68].

Our hypersonic CFD process consists of: creating the geometry in Solidworks, meshing in Pointwise, running US3D to produce the steady state solutions (basic states), and visualizing the flow field in Tecplot. The wall normal data of the basic state was extracted using a combination of Tecplot and in-house developed scripts. The mesh dimensions are as follows, 1600 streamwise points, one degree rotation in the azimuthal direction, and test-driven convergence to determined the number of wall normal points (shown in table 7.1). The flow conditions are representative of the AFOSR-Notre Dame Large Mach 6 Quiet Tunnel conditions at a unit Reynolds number of 11.0×10^6 [76].

In US3D, the inputs and boundary conditions for the freestream and the isothermal wall were calculated by using the isentropic flow relations and unit Reynolds number. The inflow conditions and wall temperature are listed in table 7.2. The other boundary conditions were defined as an outflow at the downstream end of the domain, and symmetry conditions on both azimuthal sides. Additional settings included non-reacting, laminar, viscous flow. Using CFL ramping, the calculation was run until a converged, and a steady state solution was reached [44]. Figure 7.3 shows Mach contour plots of the flow field for each nose bluntness. In each plot, a bow shock is present at the nose of each cone which shifts to an oblique shock sufficiently downstream of the nose region.

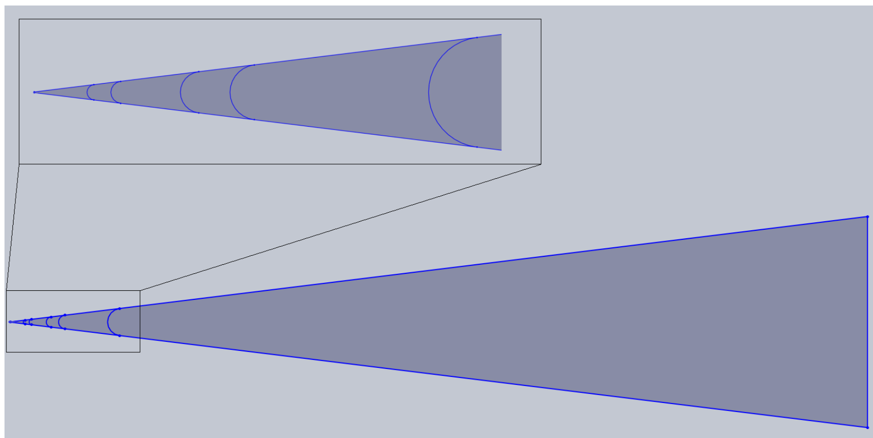

Figure 7.2: Schematic of cone geometries illustrating nose bluntness variations.

Table 7.1: Test Models

R_n (mm)	R_n (in)	Wall Normal Points
0.15	0.006	781
3.556	0.14	681
5.0	0.197	681
9.525	0.25	961
12.7	0.5	1061
25.4	1.0	2716

7.3 Results

As discussed above, it has been well established that the presence of a strong entropy layer suppresses second-mode growth. In figure 7.4, the entropy layer for

Table 7.2: Test Conditions

Re/m	ρ_∞ [kg/m^3]	T_∞ [K]	u_∞ [m/s]	T_{wall} [K]
11.0×10^6	0.0432	53.0488	875.9795	300

US3D inflow free-stream conditions for Re/m $= 11.0 \times 10^6$, corresponding to AFOSR-Notre Dame Large Mach 6 Quiet Tunnel conditions.

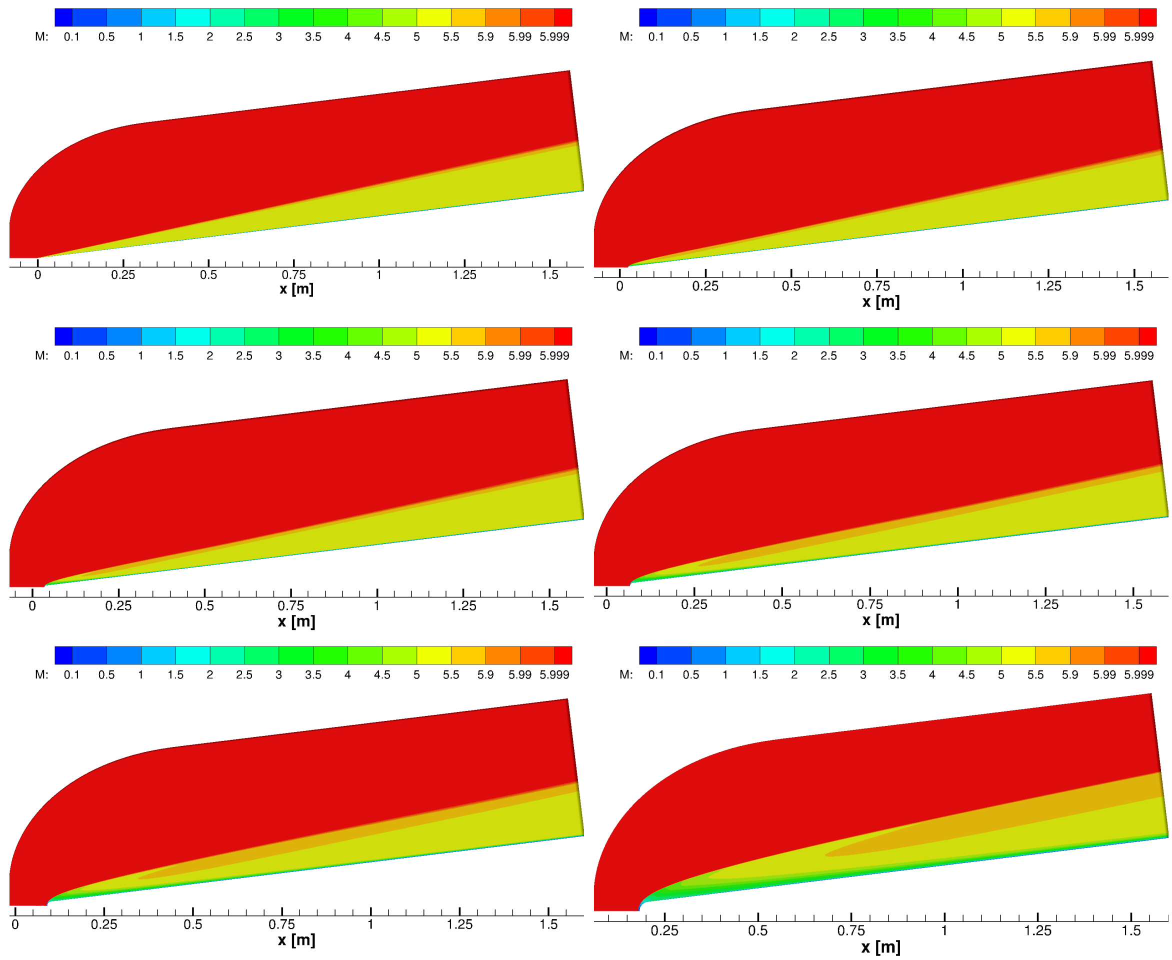

Figure 7.3: Mach contours for: Upper left: 0.15mm (sharp nose). Upper right: 3.556mm nose. Middle left: 5mm nose. Middle right: 9.525mm nose. Lower left: 12.7mm nose. Lower right: 25.4mm nose.

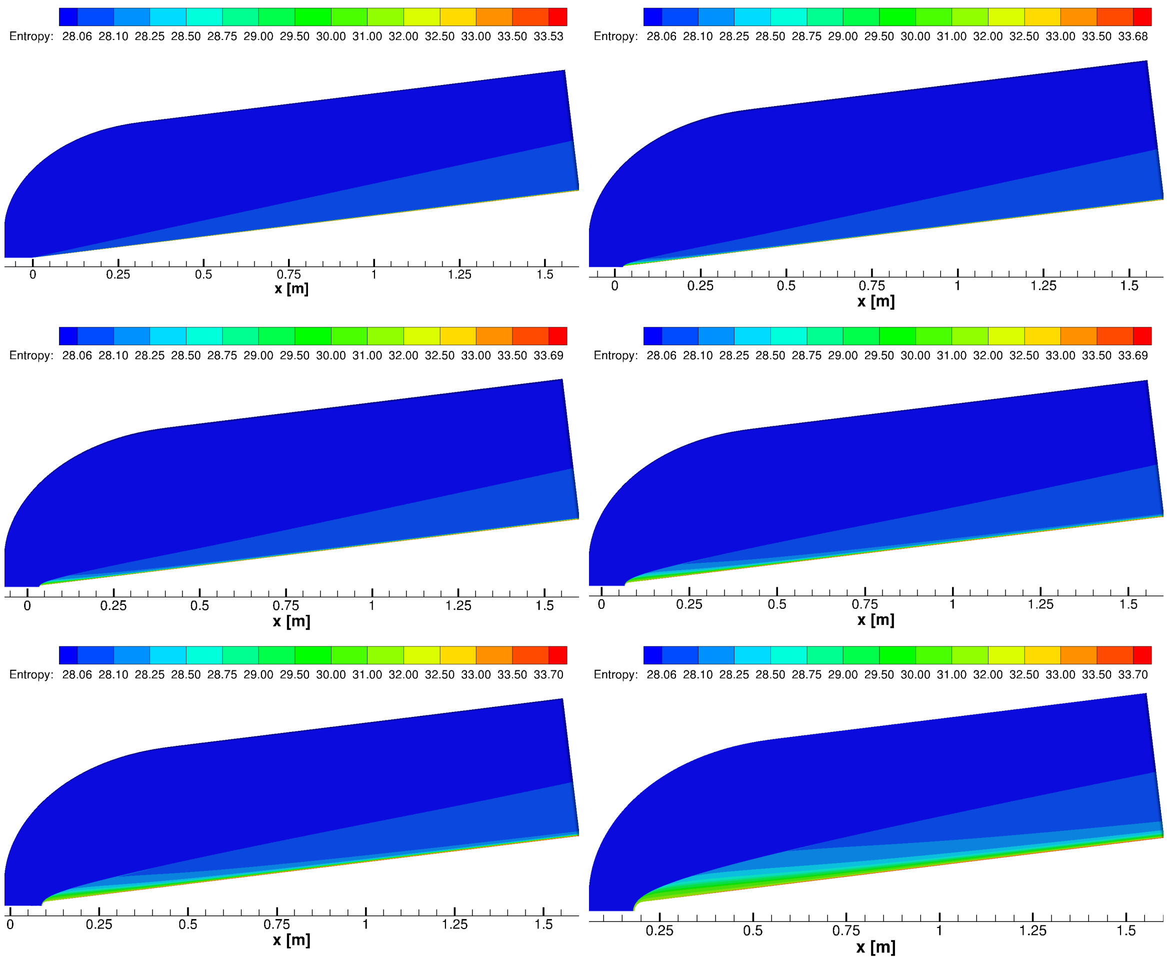

Figure 7.4: Entropy contours [J/K], $s = c_v ln\left(\frac{p}{p_\infty}\right) + c_p ln\left(\frac{\rho_\infty}{\rho}\right)$, for: Upper left: 0.15mm nose. Upper right: 3.556mm nose. Middle left: 5mm nose. Middle right: 9.525mm nose. Lower left: 12.7mm nose. Lower right: 25.4mm nose.

each case can be seen and it is clear that little or no entropy layer is present for the sharpest-nose cases (0.15mm), a small entropy layer is formed for the 3.556mm case that is swallowed after 0.3m, a slightly stronger entropy layer is formed for the 5mm nose bluntness that is swallowed around 0.5m, a robust entropy layer is formed for the 9.525mm case that is swallowed near 1.1m, and for the two bluntest-cases (12.7mm and 25.4mm) a strong entropy layer is not swallowed on the body for the cone. These results agree well with LPSE calculations (figure 7.5, left column). In those regions with no (or a weak) entropy layer, the boundary layer is susceptible to second-mode instability. In those regions with a robust entropy layer, second-mode instability is significantly diminished or not present at all. Our calculations are consistent with the expectation that modal growth is not present within the entropy layer, though an exhaustive search of oblique mode was not conducted. This is consistent with the idea that some form of non-modal growth is responsible for the blunt body paradox.

Recalling from chapter 2, the thermoacoustic interpretation of second-mode dynamics posits that second-modes behave as thermoacoustic resonators in a thermoacoustic impedance well [8]. The acoustic impedance of a homogenous medium is proportional to the square root of the basic state density ($\sqrt{\bar{\rho}}$). Figure 7.5 (right column) shows profiles of acoustic impedance at different locations along the cone for the various nose bluntnesses considered. For the sharpest-nose case (0.15mm), we observe a well-defined acoustic impedance well with a sharp gradient in impedance (density) at all locations along the cone. Comparing the impedance profiles with the stability calculations (figure 7.5), we notice that when moving downstream the acoustic impedance well widens (peak density gradient is further from the wall) and correspondingly the most unstable second-mode frequency decreases. This behavior is consistent with the thermoacoustic resonance interpretation. Next, consider the intermediate bluntness case (5mm) (figure 7.5 middle row). In this case, we observe that the entropy layer has modified the acoustic impedance well for the first few streamwise locations. Comparing with the corresponding stability results, we see that second-mode growth is suppressed at these 'modified' streamwise locations, but growth resumes once the modification has "died out" (i.e. the entropy layer has been swallowed). Finally, it is observed that for yet larger nose radii, the entropy layer extends over the entire length of the cone and significantly alters the acoustic impedance well. Considering the associated stability results, it is observed that second-mode growth is significantly suppressed along the length of the 9.525mm and 12.7mm cones. Again, these results are consistent with the thermoacoustic interpretation, which posits that the second-mode instability relies on the existence of a well-defined acoustic impedance well in which it can resonate. If this well is interfered with, for example modified by an entropy layer or some other form of disturbance, Kuehl and Paredes 2016 showed similar effects with small amplitude Görtler modes on a flared cone), then the resonance is interfered with and subsequently the second-mode dynamics are altered [22].

At this point, a final question remains: How much modification to the impedance well is required to 'detune'/destroy the second-mode resonance? To address this question, we return to the classic inflection point criteria that: $(\rho U')'$ must change sign (Lees and Lin 1946). Note from hereon, $'$ denotes wall normal derivative (d/dy). We can determine an estimate for the strength of the acoustic impedance gradient required for second-mode growth by expanding $(\rho U')' = \rho U'' + \rho' U'$. The condition that $(\rho U')'$ must change signs leads to $\rho' U' = -\rho U''$, at the generalized inflection point zero crossing. It is clear from figure 7.6 (left column) that the generalized inflection point criteria is satisfied in all cases and that to satisfy the criteria, the $\rho U''$ term must be balanced by a combination of density or velocity gradients. For the criterion to be dominated by velocity gradients, we defined $\hat{U}' = -\frac{\rho U''}{\rho'}$. For the criterion to be dominated by density gradients, we define $\hat{\rho}' = -\frac{\rho U''}{U'}$.

Figure 7.6 show profiles of the generalized inflection point, $(\rho U')'$, and components ($\rho U''$, $\rho' U'$), and the basic state density and velocity gradients ($\bar{\rho}'$, $\bar{U}'$) along with $\|\hat{U}'\|$, $\|\hat{\rho}'\|$, respectively, at five different streamwise locations which span the entropy swallowing length for the 5mm nose bluntness case. Note that despite the generalized inflection point criteria being satisfied at all locations (and that at the generalized inflection point criteria zero crossing we find $\|\hat{U}'\| = \bar{U}'$ and $\|\hat{\rho}'\| = \bar{\rho}'$), those streamwise locations upstream of approximately 0.5m do not exhibit second-mode instability, while those locations downstream do. It is also observed that for those streamwise locations upstream of approximately 0.5m (i.e. within the entropy layer), the generalized inflection point criteria is satisfied based on the strength of the basic state velocity gradients. This means that within the entropy swallowing length the criterion is indicating that velocity gradients are dominant, or $\|\hat{U}'\| > \|\hat{\rho}'\|$ at the zero crossing, where second-mode suppression is observed. Whereas, at those locations downstream of approximately 0.5m (i.e. downstream of the entropy swallowing length), the generalized inflection point criteria is satisfied based on the strength of the basic state density gradients, or $\|\hat{\rho}'\| > \|\hat{U}'\|$ at the zero crossing, where second-mode growth is observed. More specifically, consider in figure 7.6 the right column. For the 0.11m upstream location (top image), at the zero point crossing of the generalized inflection point we observe that $\|\hat{U}'\| = \bar{U}'$ is much greater than $\|\hat{\rho}'\| = \bar{\rho}'$. With each step further downstream (successive figures down the column), we see that $\|\hat{U}'\| = \bar{U}'$ becomes smaller, while $\|\hat{\rho}'\| = \bar{\rho}'$ gets larger, until they swap places, and $\|\hat{\rho}'\| = \bar{\rho}'$ dominates at a sufficiently downstream position. This implies that second-mode growth is suppressed by the entropy layer 'detuning'/destroying the basic state density gradient.

Therefore, we find that nose bluntness suppresses second-mode growth via entropy layer modulation of the basic state density gradients, which is consistent with the thermoacoustic resonance interpretation of second-modes. In other words, the entropy layer destroys the thermoacoustic impedance well required to sustain thermoacoustic resonance.

7.4 Discussion

The mechanism by which nose bluntness suppresses second-mode instability has been investigated by studying 7 degree half-angle straight cones with nose bluntnesses of 0.15mm, 3.556mm, 5mm, 9.525mm, 12.7mm and 25.4mm at tunnel conditions relevant to the AFOSR-Notre Dame Large Mach 6 Quiet Tunnel. As expected, our results are consistent with previous studies which find that within the entropy layer, second-mode instability is suppressed. However, here we have explicitly shown that the physical mechanism by which this suppression is achieved is via entropy layer modulation of the basic state density gradient. This is consistent with the thermoacoustic resonance interpretation of second-mode dynamics, i.e. second-mode waves behave as resonant thermoacoustic waves trapped in a thermoacoustic impedance well formed between strong basic state density gradient and the vehicle wall. We have shown that the entropy layer weakens the basic state density gradient sufficiently enough to destroy this resonance, and thus stabilize the second-mode waves. Furthermore, we provided a metric for determining when a second-mode instability will be present by considering the generalized inflection point criteria: $(\rho U')' = \rho U'' + \rho' U'$, noting that at the zero point crossing: $\|\hat{U}'\| = \bar{U}'$ and $\|\hat{\rho}'\| = \bar{\rho}'$. Specifically, second-mode instability is present when at the generalized inflection point zero crossing: $\|\hat{\rho}'\| > \|\hat{U}'\|$, and is suppressed when at the generalized inflection point zero crossing: $\|\hat{U}'\| > \|\hat{\rho}'\|$. That is, when basic state density gradients dominate the generalized inflection point criteria, second-mode instability is present (i.e. the acoustic impedance well is strong enough to support resonance), and when basic state velocity gradient dominates the generalized inflection point criteria, second-mode growth is suppressed.

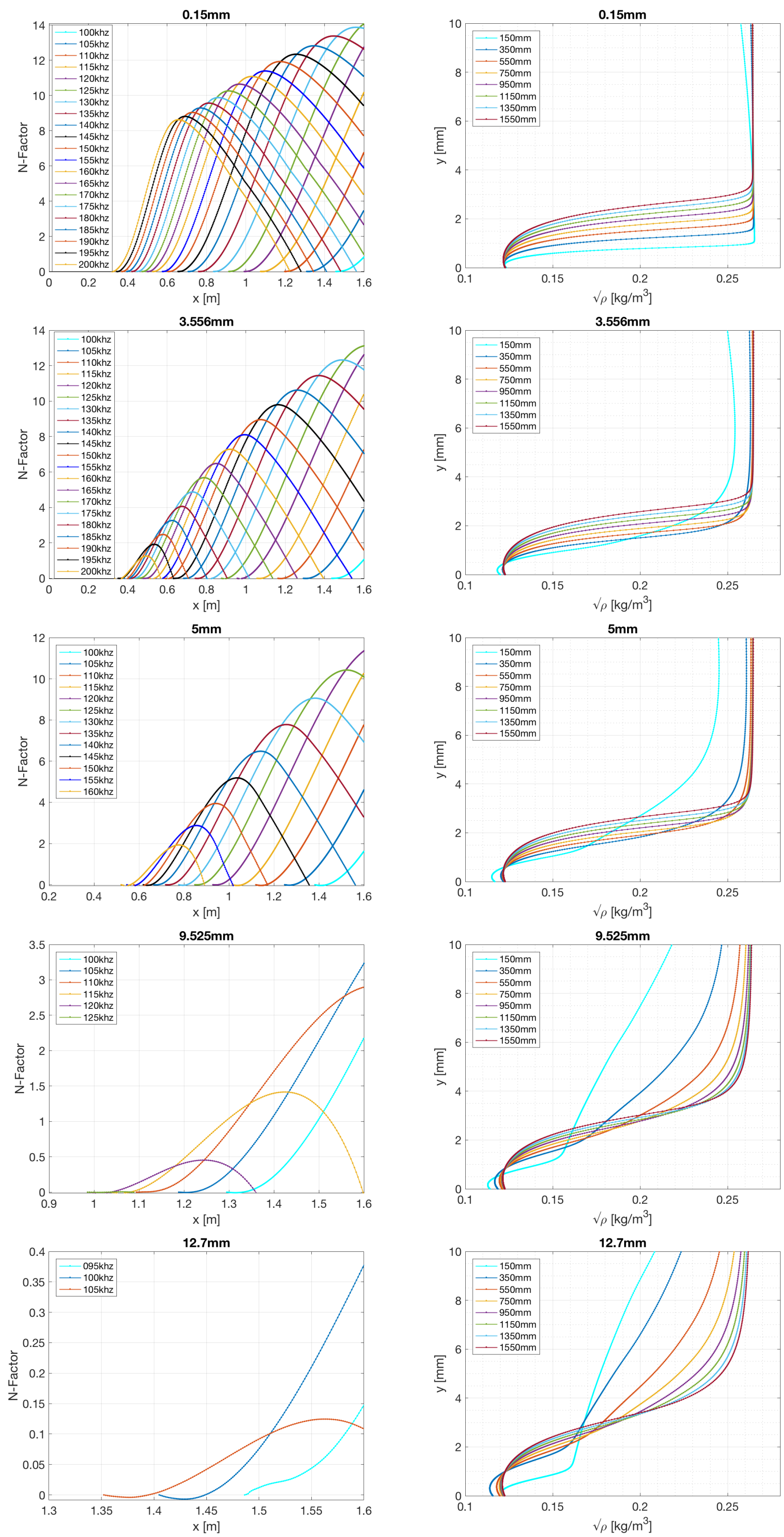

Figure 7.5: Shown starting from top to bottom nose radii of: 0.15mm, 3.556mm, 5mm, 9.525mm, and 12.7mm. Left column: N-factors. Right column: acoustic impedance profiles ($\sqrt{\overline{\rho}}$) at various streamwise locations.

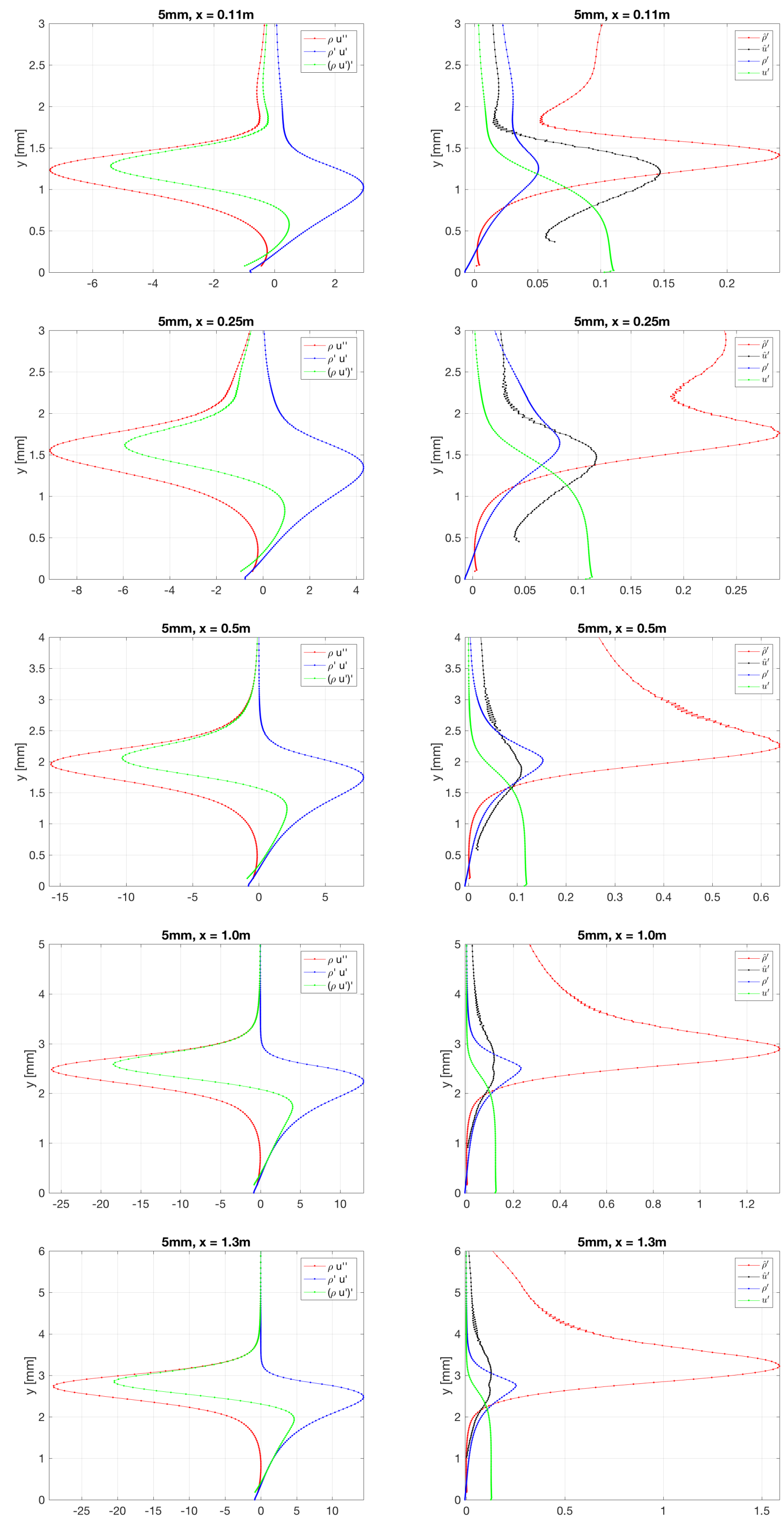

Figure 7.6: Shown are results for 5mm nose bluntness at various streamwise locations. Left column: generalized inflection point criteria. Right column: density and velocity gradients ($\bar{\rho}'$, $\bar{U}'$, $\|\hat{\rho}'\|$, $\|\hat{U}'\|$).

Chapter 8

IMPLICATIONS OF LOCAL WALL TEMPERATURE VARIATIONS ON SECOND-MODE INSTABILITY

8.1 Introduction

In this chapter, wall temperature variations were numerically tested using LST and linear PSE along the Purdue flared cone at Mach 6 BAM6QT conditions. The purpose of this research was to determine the viability of localized temperature controlled regions to control second-mode instability. Such temperature variation could be generated by thermocouples or, perhaps, through choosing vehicle materials with different degrees of thermal conductivity or insulation. It is generally understood that wall heating suppresses second-mode growth, while wall cooling enhances growth. Cooling and heating affect the acoustic impedance well by altering the density gradient and thereby altering disturbance growth.

This also leads to a potential physical explanation for the results of Fong et al. (2015) in which sufficiently large 2D surface roughness were capable of suppressing second-mode growth [77]. It is also known that changes in the vehicle wall temperature can alter the second-mode dynamics [19]. In general, evidence shows that wall cooling dampens first-mode disturbances, while heating the wall dampens second-mode disturbances [19]. However, to the author's knowledge, the affect of 2D heating/cooling bands (similar to the 2D roughness of Fong) on second-mode instability have not been investigated [77].

In this chapter, heated/cooled wall temperature segments, denoted as "heat strips" or "cool strips", are numerically analyzed to study their effect on second-mode instability. Also, in the context of the thermoacoustic resonance interpretation, the physical mechanism through which such strips modify second-mode dynamics is address. Such heat/cool strips may serve as potential active or passive controls strategies for second-mode instability. The result of this study may also prove insightful for hypersonic vehicle designers concerning material selection via natural thermal properties of various materials.

8.2 Basic States

The Purdue flared cone geometry was used once again for the various basic states which were generated. The flow conditions are representative of the Purdue Boeing/AFOSR Mach-6 Quiet Tunnel (BAM6QT) conditions at a unit Reynolds number of 10.8×10^6 [11, 38, 40, 41, 46]. This corresponds to a maximum second mode disturbance frequency occurring at roughly 300kHz which is consist with experimental and DNS results [42, 43, 45, 46]. In US3D, the inputs and boundary conditions for the freestream and the isothermal wall were calculated by using the isentropic flow relations and unit Reynolds number (equations, 8.1). The inflow conditions for the base case are listed in table 1, and the corresponding wall temperatures for each basic state ran are listed in table 2. Additional boundary conditions include an outflow at the downstream end of the cone, and symmetry conditions on both azimuthal sides. The settings included non-reacting, laminar, viscous flow at the inflow boundary. Using CFL ramping, the simulation was ran until a converged, and a steady state solution was reached [44]. Figure 4.2 shows a Mach contour plot of the flow field for the Base case. A weak, oblique shock is visible towards the middle of the plot, becoming more pronounced moving further downstream which again is consistent with the results of Fasel et al. (2015) [26].

$$\frac{P_0}{P} = \left(\frac{\rho_0}{\rho}\right)^{\gamma} = \left(\frac{T_0}{T}\right)^{\frac{\gamma}{\gamma-1}}$$
$$\frac{T_0}{T} = 1 + \frac{\gamma - 1}{2} M^2 \tag{8.1}$$

Boundary	BAM6QT Re/m	US3D Re/m	ρ_∞ [kg/m^3]	T_∞ [K]	u_∞ [m/s]	Mach
Inflow	11.0×10^6	10.8×10^6	0.0355	51.9799	867.1092	6

Table 1: US3D Free-stream conditions corresponding to second-mode 300kHz disturbance matching of Purdue BAM6QT conditions.

Table 8.1: Table 2: US3D wall boundary conditions for Re/m = 10.8×10^6.

Case	T_{wall} [K]	Cooled/Heated Region(s)
BASE	300	Entire Wall
BASE350	350	Entire Wall
BASE250	250	Entire Wall
HS35015	350	0.15m - 0.20m
HS35020	350	0.20m - 0.25m
HS35025	350	0.25m - 0.30m
HS35030	350	0.30m - 0.35m
HS35035	350	0.35m - 0.40m
HS35040	350	0.40m - 0.45m
HS35045	350	0.45m - 0.50m
CS35005	250	0.05m - 0.10m
CS35010	250	0.10m - 0.15m
CS35015	250	0.15m - 0.20m
CS35020	250	0.20m - 0.25m
CS35025	250	0.25m - 0.30m
CS35030	250	0.30m - 0.35m
CS35035	250	0.35m - 0.40m
CS35040	250	0.40m - 0.45m
HS350V10	350	0.10m width
HS350V15	350	0.15m width
HS350V20	350	0.20m width
CS250V10	250	0.10m width
CS250V15	250	0.15m width
CS250V20	250	0.20m width
CHCHALF	250 & 350	0m - 0.25m & 0.25m - 0.517m
CHC0550	250 & 350	0m - 0.05m & 0.05m - 0.517m
CHC1050	250 & 350	0m - 0.10m & 0.10m - 0.517m
CHC1550	250 & 350	0m - 0.15m & 0.15m - 0.517m
CHC2050	250 & 350	0m - 0.20m & 0.20m - 0.517m
CHCOPT1010	250 & 350	0.05m - 0.15m & 0.25m - 0.35m
CHCOPT1015	250 & 350	0.05m - 0.15m & 0.25m - 0.40m
CHCOPT1020	250 & 350	0.05m - 0.15m & 0.25m - 0.45m
CHCOPT1515	250 & 350	0.05m - 0.20m & 0.25m - 0.40m
CHCOPT1520	250 & 350	0.05m - 0.20m & 0.25m - 0.45m

8.3 Results

It is well known that wall heating or cooling will affect second-mode growth [6]. Figure 8.1 shows the affect of varying wall temperature (uniform over the entire body) from 250K to 300K (our base case) to 350K on growth of a 300kHz second-mode. Notice that wall cooling enhances second-mode amplification, while wall heating reduces second-mode amplification, as expected. However, it is observed that a region encompassing the N1 neutral point (where instability begins), that these effects are reversed. That is, near the N1 neutral point, wall cooling locally reduces second-mode growth while wall heating amplifies second-mode growth. This is in agreement with Zhao et al (2018) which showed that placing a heating strip upstream or a cooling strip downstream of the synchronization point respectively would amplify second-modes [78].

This behavior can be understood by considering the stability diagram (figure 8.2) for the 300K wall temperature case. The affect of wall heating is to expand the thermal boundary layer (details shown later) and thus, based on the thermoacoustic interpretation, shifts the stability diagram downward towards lower frequencies. This would have the affect on the 300kHz mode to initially amplify the instability, relative to the base 300K wall temperature case, near the front of the cone, but ultimately reduce the overall disturbance growth. The opposite happens for wall cooling. However, when one particular frequency is detuned (amplitude reduced), another frequency could become tuned (amplitude increased). This effect is shown in the two lower panels of figure 8.1 where 25kHz variations (about the most amplified 300kHz case) were tested. The 275kHz test (bottom left plot) shows that heating the wall at this frequency increased N-factors to higher than the base case. In the bottom right plot, 325kHz was tested, and now cooling the wall resulted in significantly higher N-factors.

8.3.1 Heat/Cool Strip Streamwise Location Variation

To better understand the tuning/detuning of different frequencies by wall heating/cooling, additional frequencies were tested to determine the new largest N-factor frequency for heated and cooled walls respectively. Figure 8.3 shows the results. The

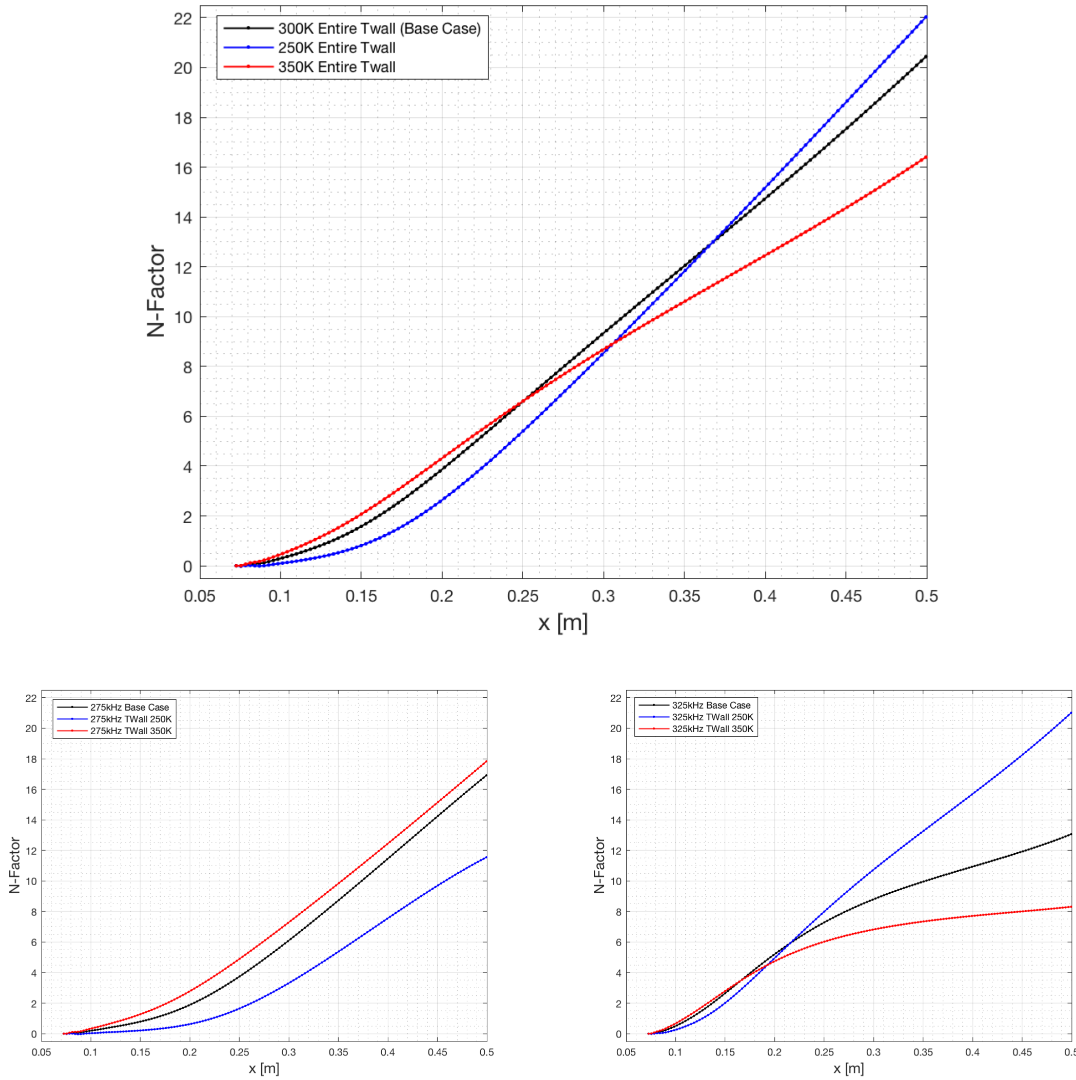

Figure 8.1: LPSE N-factor results - Total wall temperature varied (Twall) tests, 300kHz (top), 275kHz (bottom left), 325kHz (bottom right).

largest N-factors (just above 23) for the cooled wall occurred at 310kHz. Whereas, the largest N-factors for the heated wall occurred at 285kHz, but were slightly lower than the base case at just below 18.5. Note, at 275kHz the highest N-factors achieved, above the base case, for a heated wall were just below 18. It is also noteworthy that neither the 275kHz nor the 285kHz cases have N-factors which reach higher than the 300kHz base case (N-factor of 20.5). However, the 310kHz and even the 325kHz cooled wall

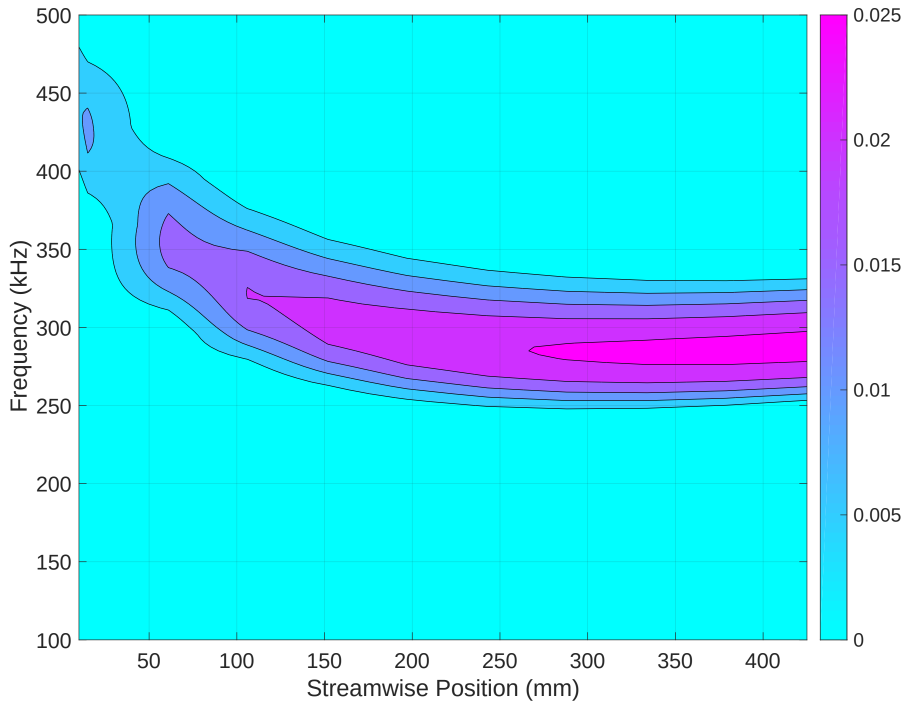

Figure 8.2: LST Stability Diagram.

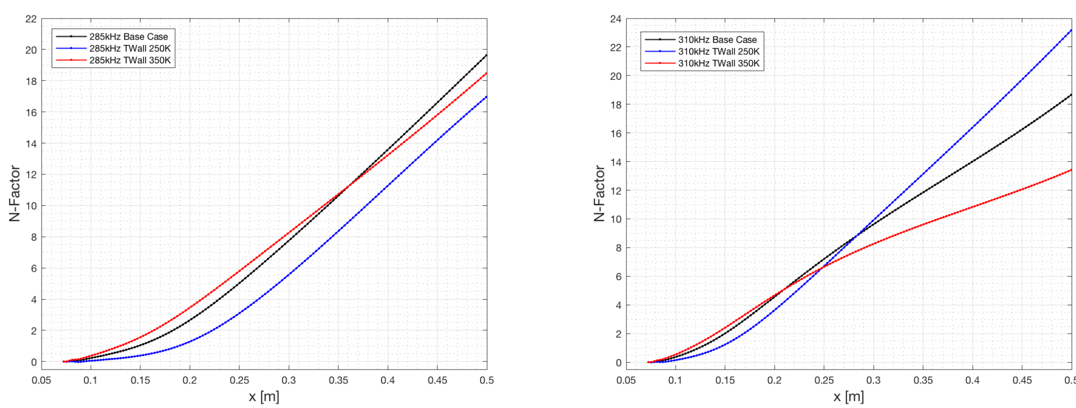

Figure 8.3: LPSE N-factor results - Total wall temperature varied (Twall) tests, N-factor frequency 285kHz (left), 310kHz (right).

case achieved N-factors above 20.5, so this test provided a good guide for performing the optimization tests which will be discussed later on.

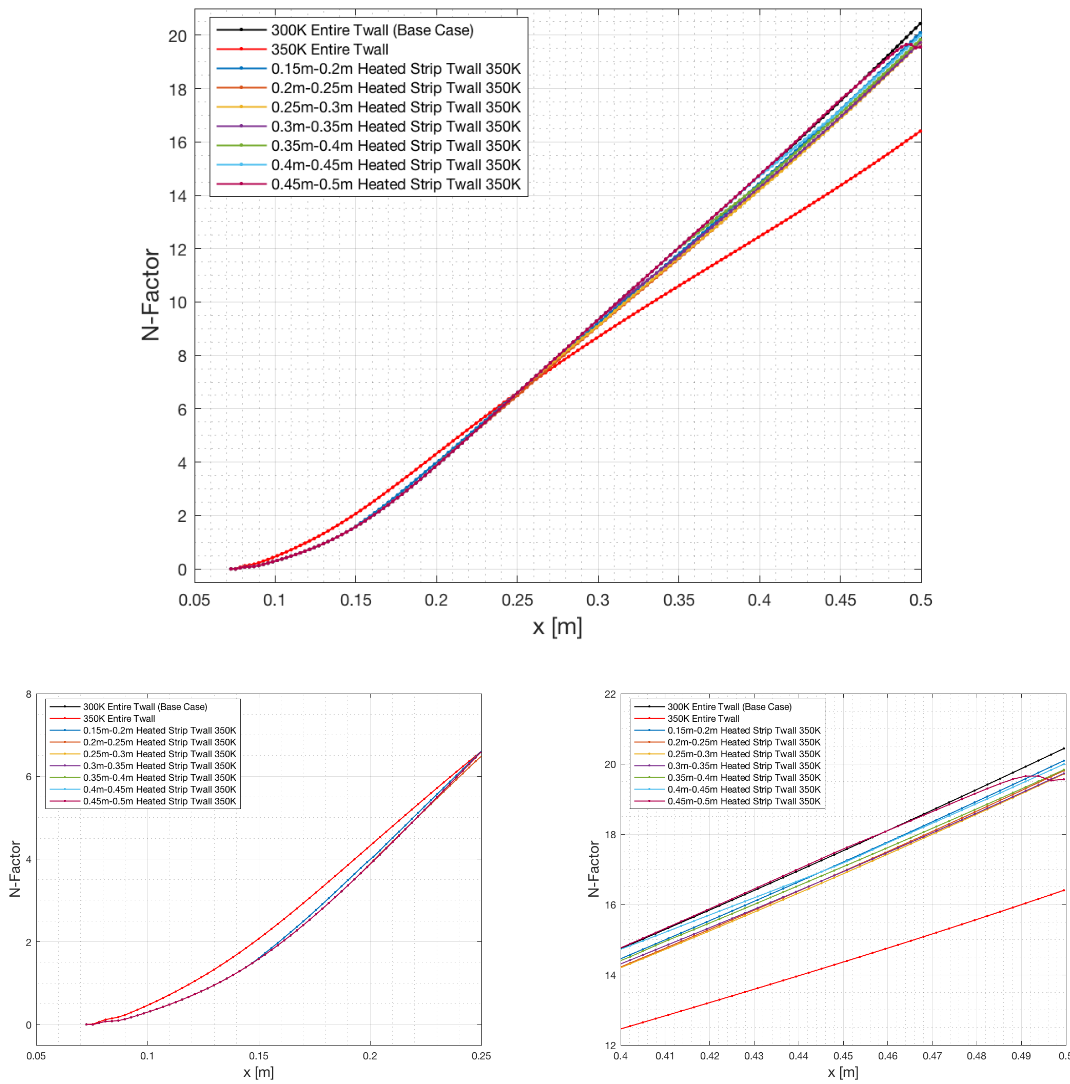

Figure 8.4: LPSE N-factor results - Heated wall varied spatial 5cm strip length tests, 0.05m - 0.5m (top), 0.05m - 0.25m section (bottom left), 0.4m - 0.5m section (bottom right).

To understand the spatial sensitivity of second-mode growth to localized wall heating, a series of tests were ran in which a 5cm heat strip was placed at different locations along the cone (figure 8.4). It is observed that the optimal location for such

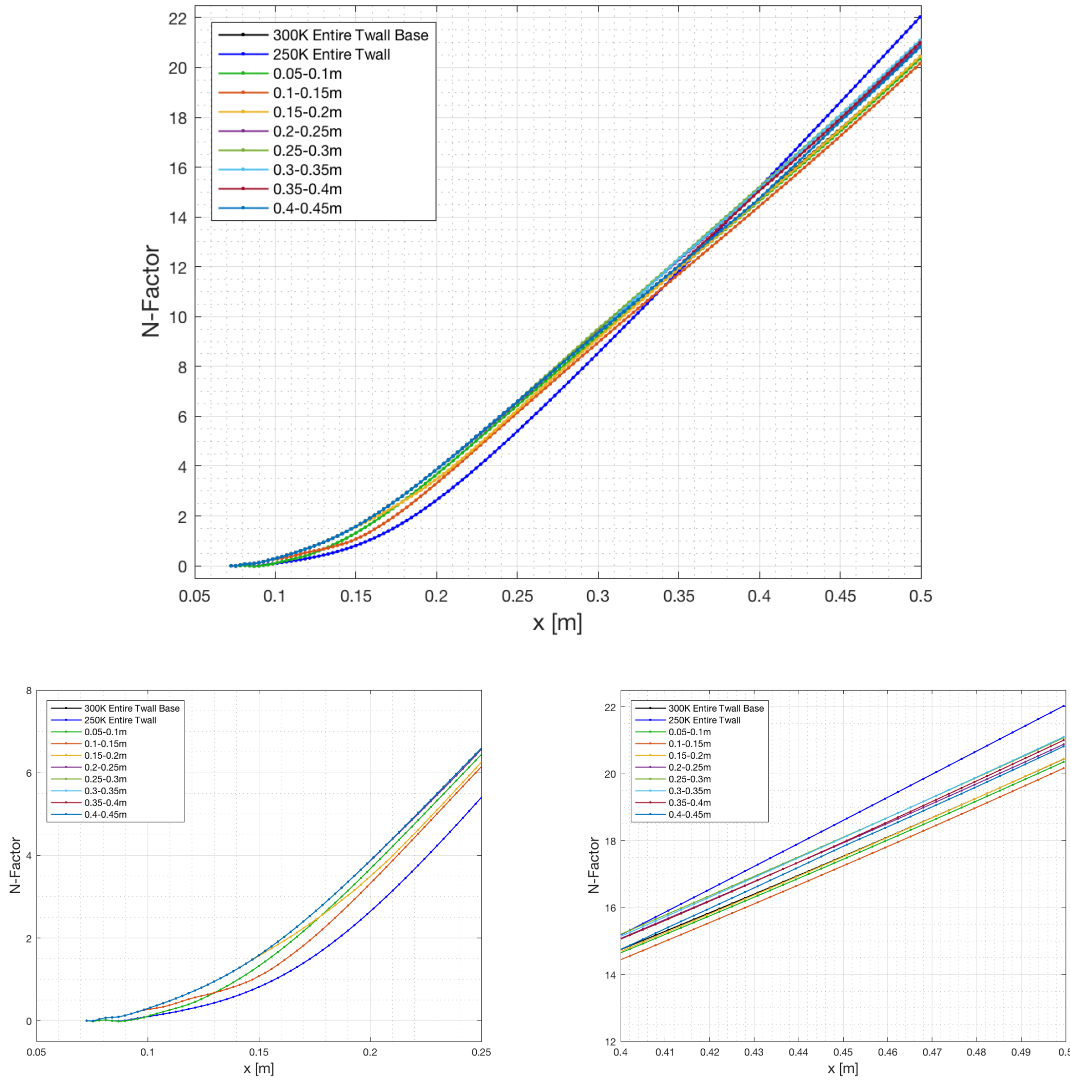

Figure 8.5: LPSE N-factor results - Cooled wall varied spatial 5cm strip length tests, 0.05m - 0.5m (top), 0.05m - 0.25m section (bottom left), 0.4m - 0.5m section (bottom right).

a heat strip to control second-mode growth, is between 0.25 and 0.30 meters from the nose tip. This results in an N-factor reduction of approximately 0.75 (a 50% reduction in amplitude). With the optimal location for localized wall heating identified, we will now consider the optimal location for wall cooling. A region of localized wall cooling was spatially varied, similarly to the heated wall region spatial variation case, and the corresponding stability results are shown in Figure 8.5. The strongest initial dampening occurred for the cooled wall strip located at 0.05 - 0.10 meters and the location which resulted in the lowest overall N-factors was 0.10 - 0.15 meters.

The initial wall heating/cooling results (figures 8.1, 8.3, 8.4, and 8.5) indicate that wall cooling will be more effective closer to the N1 neutral point's location than where wall heating was found to be optimal. These results showed that the downstream amplification can be avoided where cooling is performed sufficiently upstream, compared to the total cooled wall cases. This is also in agreement with results from Zhao et al. which showed that an efficient way to stabilize growth is to cool upstream or heat downstream [78]. These results also led us to believe, perhaps a combination of upstream cooling and downstream heating may lead to improved disturbance damping compared to cooling and heating alone. Figure 8.6 shows the LPSE N-factors when a cool strip has been placed in front of the heat strip. Using the optimal cooling and heating locations determine from the spatial variations, the cool-heat strip combo was found to be most effective. It is found that the optimal locations of $\pm$50K temperature variation strips result in a reduction of N-factor by about 1 (ie. almost a 3-fold reduction in disturbance amplitude). While this is not a particularly large amplitude reduction, it does confirm that passive wall heating/cooling can be employed to modify second-mode growth. More important than the amplitude reduction found in this preliminary study, is an understanding of how wall heating/cooling achieves second-mode control.

8.3.2 Physical Control Mechanism

To understand the affect of wall heating/cooling on second-mode growth, we again refer to the thermoacoustic resonance interpretation provided by Kuehl [8]. Recall, this interpretation posits that second-modes behave as resonant thermoacoustic instabilities oscillating in a thermoacoustic impedance well. The particular frequency (or frequency bandwidth) that resonates is determined by the height associated with

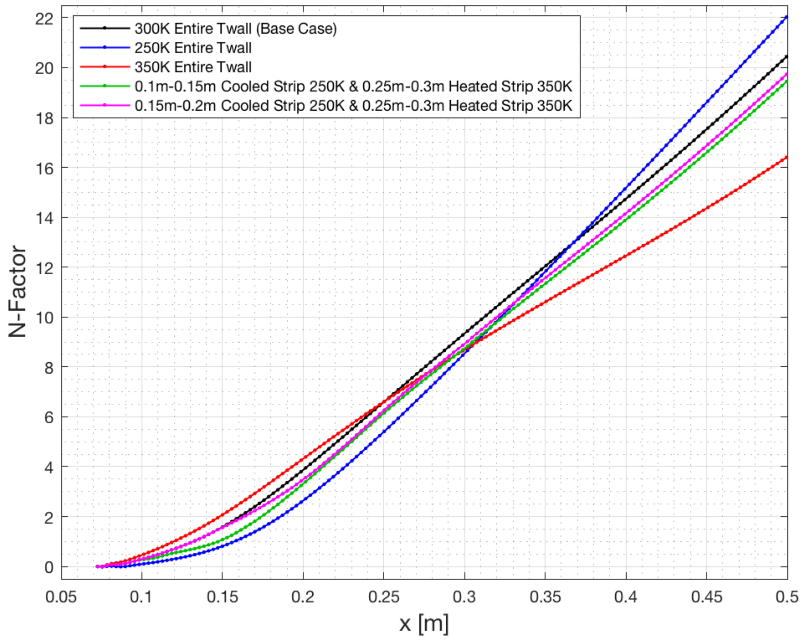

Figure 8.6: LPSE N-factor results - 5cm strip length upstream cooled, downstream heated wall combination tests.

the acoustic impedance well. The larger the height, the lower the frequency, and vice-versa. Physically, because it takes a sound wave longer to traverse a longer distance. The affect of localized wall heating/cooling is shown in figure 8.7. Profiles are shown of acoustic impedance ($\sqrt{\overline{\rho}}$) and streamwise velocity difference from the basic flow states. It is seen that wall cooling has the affect to decrease the impedance well height, while heating has the affect to increase the height. These trends are consistent with the prior explanation of 'tuning' or 'detuning' of a particular frequency second-mode. Moreover, it can be seen that just after cooling or heating, the density and velocity plots begin to re-normalize to the base case similarly to the results of Zhao et al. [78].

8.3.3 Heat/Cool Strip Length Variation

The aforementioned results provided motivation to conduct further study of heat/cool strip control potential, particularly as the results in figure 8.1 suggest this to be possible. The next step in these efforts was to vary the length of localized cooling

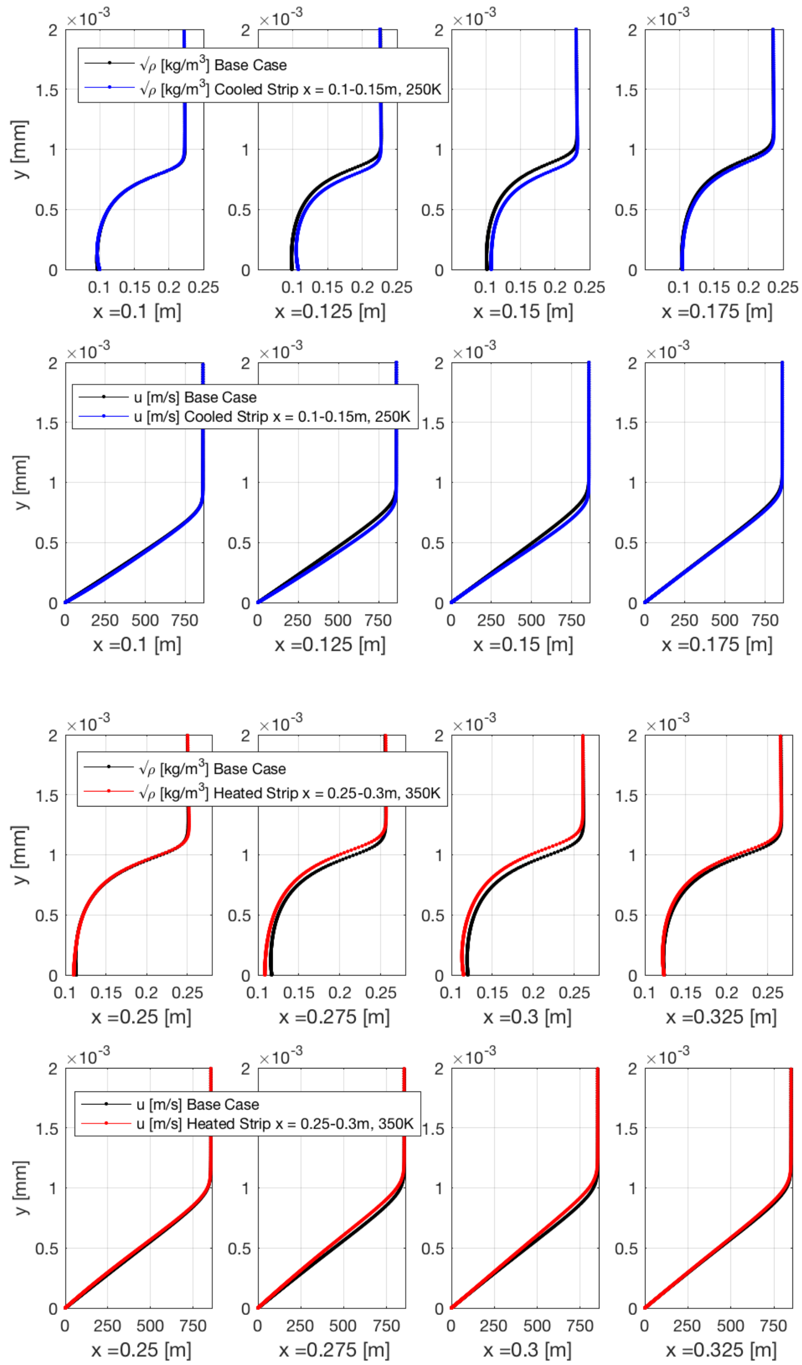

Figure 8.7: Top: Cooled wall impedance ($\sqrt{\overline{\rho}}$) and velocity profiles. Top: Heated wall impedance ($\sqrt{\overline{\rho}}$) and velocity profiles.

and heating. Figure 8.8 shows the results of varying the length of the strips. The results show that the overall trend of increasing the length of the temperature varied region dampens the second-mode growth with one exception, the 200mm length cooled strip. This is because the length of the cooled strip extended into the region where the previous results show wall heating should be applied to dampen second-mode growth. A range of frequencies were tested to see how lengthening the strips would alter the most amplified/suppressed frequency by tuning/detuning the boundary layer. All three heated lengths only slightly increased N-factors at 275kHz. At 285kHz all cases were dampened from the base. At 310kHz the cooled lengths of 150mm slightly increased, 200mm increased, while at 325kHz all cooled lengths increased N-factors. However, these N-factors are still substantially lower than the 300kHz case, and extending the length of the upstream cooled wall is acceptable so long as one does not insert too long of a cooled strip.

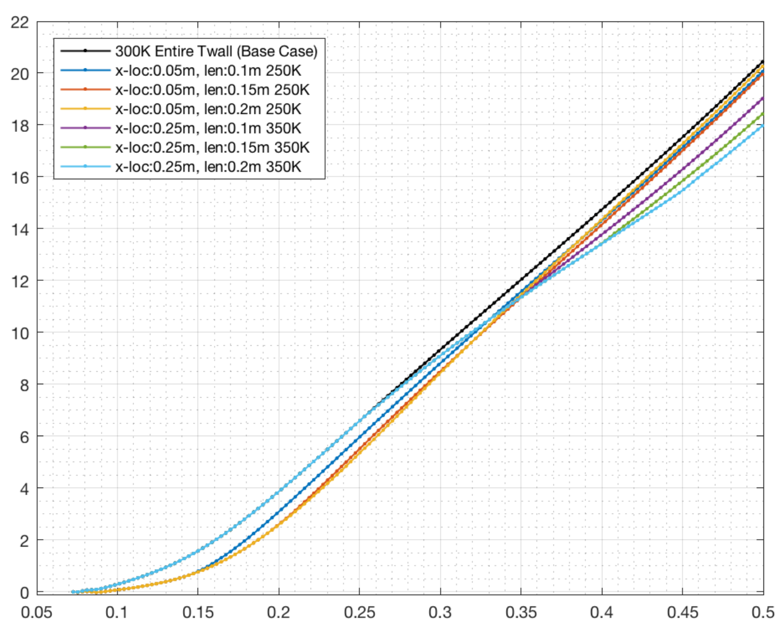

Figure 8.8: LPSE N-factor results - Varied strip length tests at 300kHz, 'x-loc' is the streamwise x location the beginning of the strip was placed, 'len' is the length of the strip.

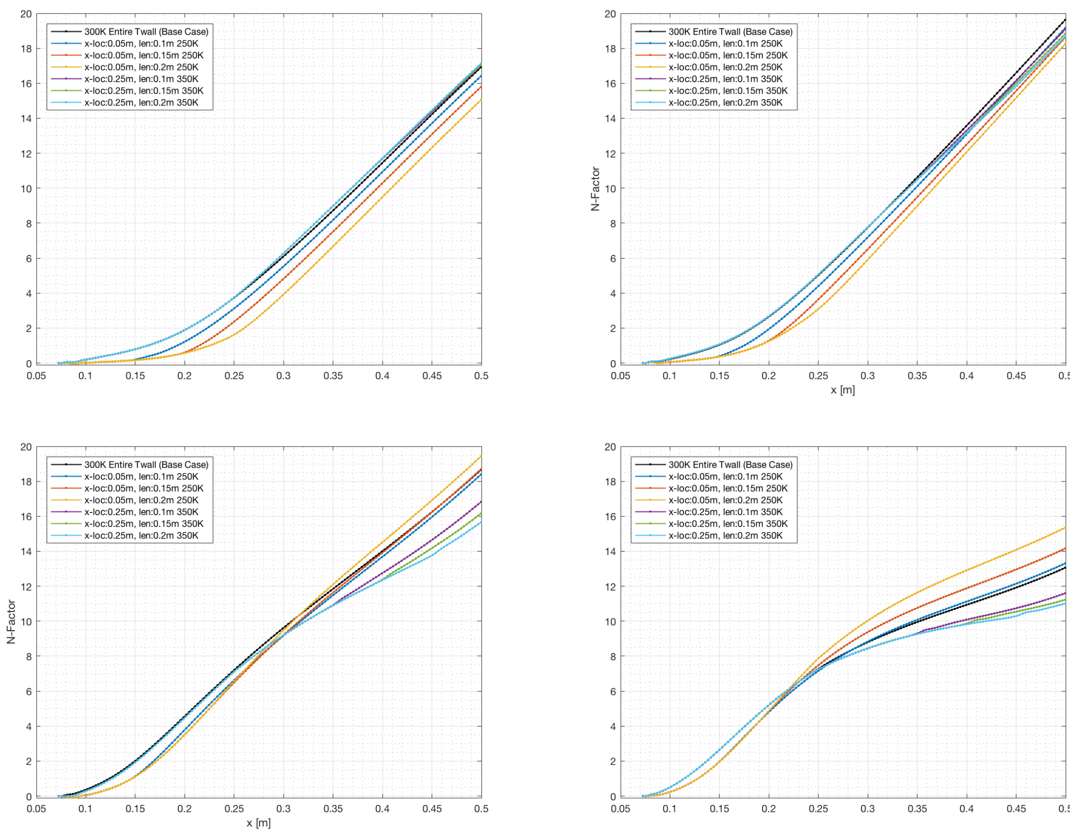

Figure 8.9: LPSE N-factor results - Varied strip lengths tests at 275kHz (top left), 285kHz (top right), 310kHz (bottom left), and 325kHz (bottom right), 'x-loc' is the streamwise x location the beginning of the strip was placed, 'len' is the length of the strip.

8.3.4 Ideal Heating and Cooling Combinations

Thus far, it has been shown that the location, length and combination of heated and cooled wall temperature strips can be utilized to suppress second-mode growth. The best case ('ideal' or 'limiting' case) for second-mode damping would be to cool the entire upstream portion of the wall and heat the downstream portion. This led to testing "half & half" heating/cooling combination variations where the first part of the wall is cooled to a certain streamwise distance, then heated thereafter until the end of the cone. To determine the optimal location at which cooling should transition to heating, a systematic test was conducted. The results of this test are shown in figures 8.10 and 8.11. Figure 8.10 considers the 300kHz second-mode (most unstable in the base case) and shows second-mode damping for all cases. However, this half-cooled and half-heated combination (cooled 0-0.25m; heated 0.25m-end of cone) was not found to be optimal, particularly when a range of frequencies is considered. When comparing figures 8.10 and 8.11, it was found that the optimal case for 300kHz second-mode damping (cooling to 0.15m and heating beyond, resulting in an N-factor of about 16.5) was not optimal for the 285kHz second-mode (resulting in an N-factor of about 18). The reason for this behavior is that in addition to a reduction of second-mode N-factors, there is also a shifting in the spectrum of the most unstable frequency. That is, the primary 300kHz second-mode may no longer be the most unstable, and one must consider a range of frequencies to determine the ideal case.

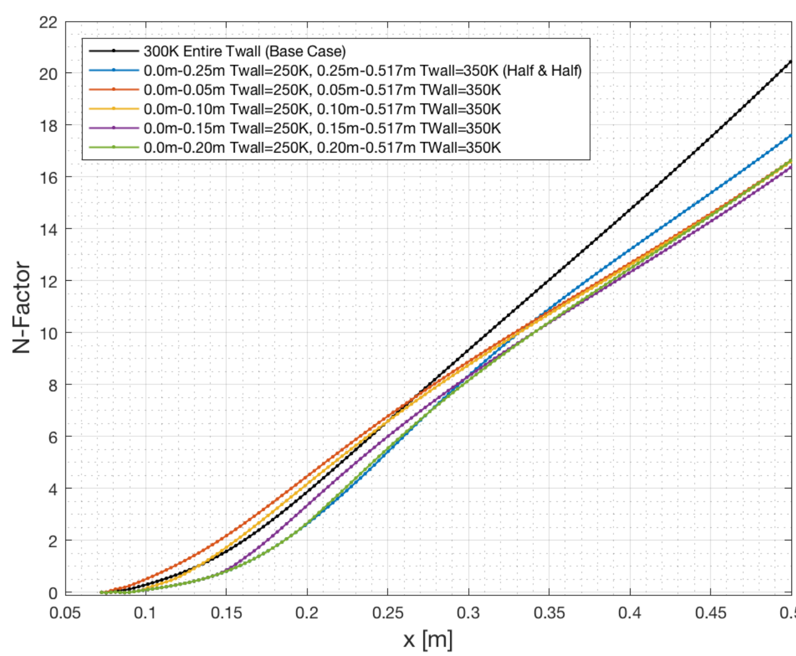

Figure 8.10: LPSE N-factor results - Full length Twall variations for limiting (ideal) case of cool/heat wall combinations at 300kHz.

To account for the shifting in the spectrum, a range of frequencies from 250kHz

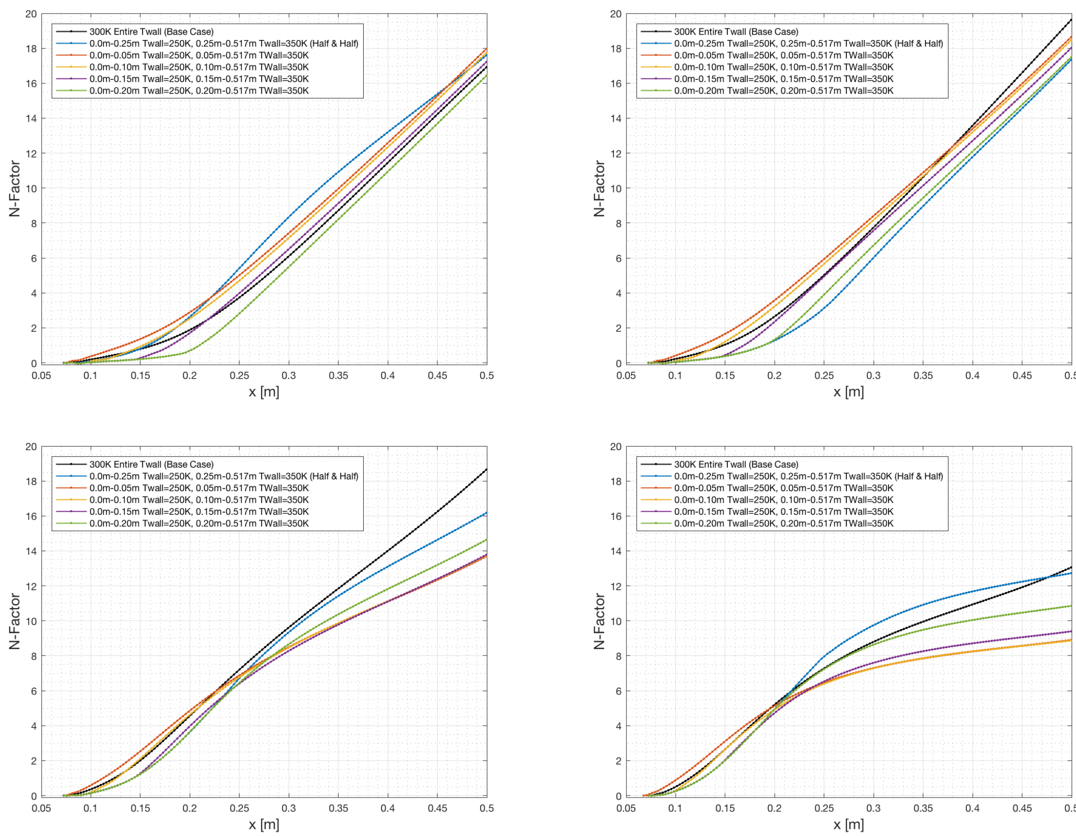

Figure 8.11: LPSE N-factor results - Full length Twall variations for limiting (ideal) case of cool/heat wall combinations at 275kHz (top left), 285kHz (top right), 310kHz (bottom left), and 325kHz (bottom left).

to 340kHz was considered for each of the ‘half & half’ cases and max N-factors are shown in figure 8.12 . The ’ideal’ case was found to cool until 0.2m, then heat the rest of the cone. Notice that the trend as the cooling region is lengthened: The overall maximum N-factor reduces while the frequency of the most unstable disturbance shifts to higher frequencies. Also note there is a weak trend of the spectrum to broaden. This behavior can be understood by returning to figure 8.2. The effect of cooling is to shift the stability diagram towards higher frequencies (by reducing the length scale of the thermoacoustic impedance well), while the affect of heating is to shift the stability diagram to lower frequencies (by reducing the length scale of the thermoacoustic impedance well). Thus, the combined effect on the stability diagram is an effective

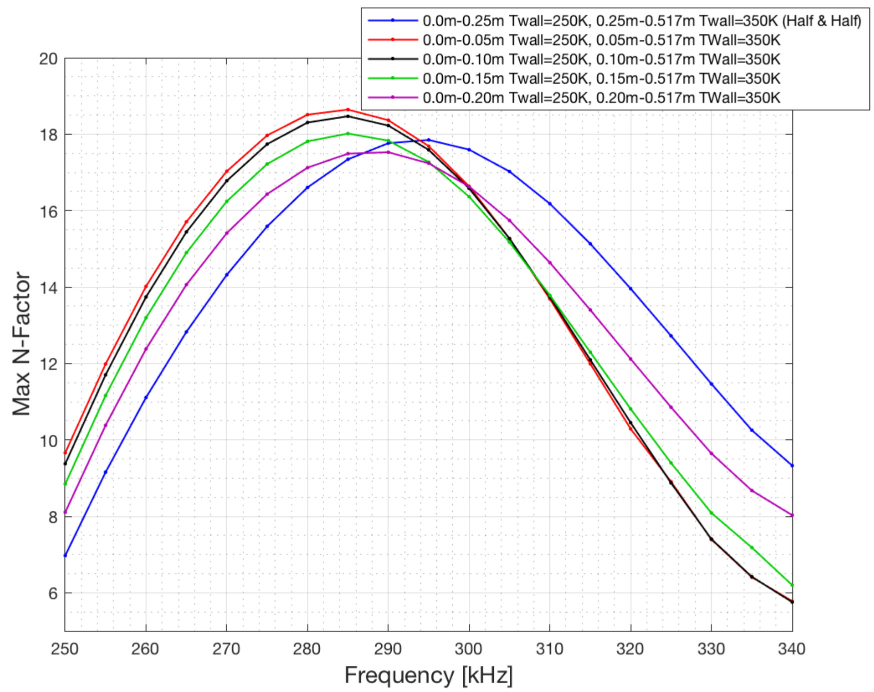

Figure 8.12: LPSE N-factor results - Ideal cases cool/heat wall combination localized strips spectrum plot.

clockwise rotation about the 0.2m, 300kHz point. Each individual frequency disturbance has a smaller streamwise distance over which it is resonant (ie growing), which accounts for the N-factor reduction. However, a larger bandwidth of frequencies is excited, which accounts for the broadening of the spectrum.

8.3.5 Practical Heating and Cooling Combinations

The previous test provided a benchmark for a limiting or ideal case, essentially showing us “the theoretical best one can do with cool/heat combinations given this situation”. However, the practicality of heating/cooling an entire geometry is not likely feasible. Therefore, we now consider a more feasible case of combinations of localized cooling and heating strips. N-factors were calculated at 300kHz (figure 8.13) and 275, 285, 310, 325kHz (figure 8.14) for finite length cooling and heating strips. Using the above results as a guide, strip lengths of 0.1 - 0.15m were considered. 300kHz disturbance N-factors were found to decreased by as much 3. Interestingly, the N-factors at the other tested frequencies all decreased from base case as well, though not quite as dramatically.

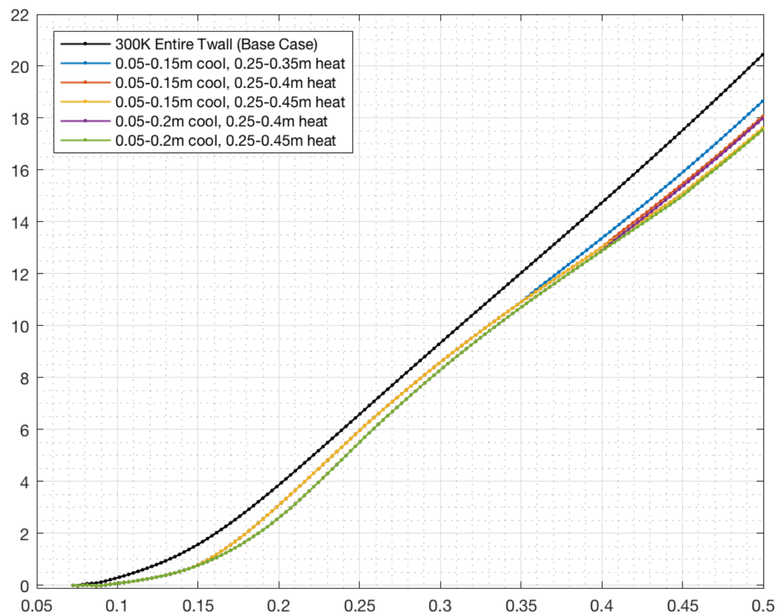

Figure 8.13: LPSE N-factor results - Optimal cases cool/heat wall combination localized strips.

The spectrum of disturbances spanning frequencies from 250kHz to 340kHz was again considered to determine maximum growth. Figure 8.15 shows a maximum N-factor comparison for different length strip combinations. It was found that the optimal case was that in which the wall was cooled from 0.05m - 0.2m, then heated from 0.25m - 0.45m. This case had a maximum N-factor of 18, which is 3 lower than the base case, and corresponds to more than an order of magnitude damping of second-mode growth, relative to the base case.

Figure 8.16 provides an overall summary of our result. Maximum N-factors for the base, entire cooled wall, entire heated wall, ideal cooled until 0.15m and 0.2m, and the more feasible, optimal cases were all plotted. As expected, heating the entire

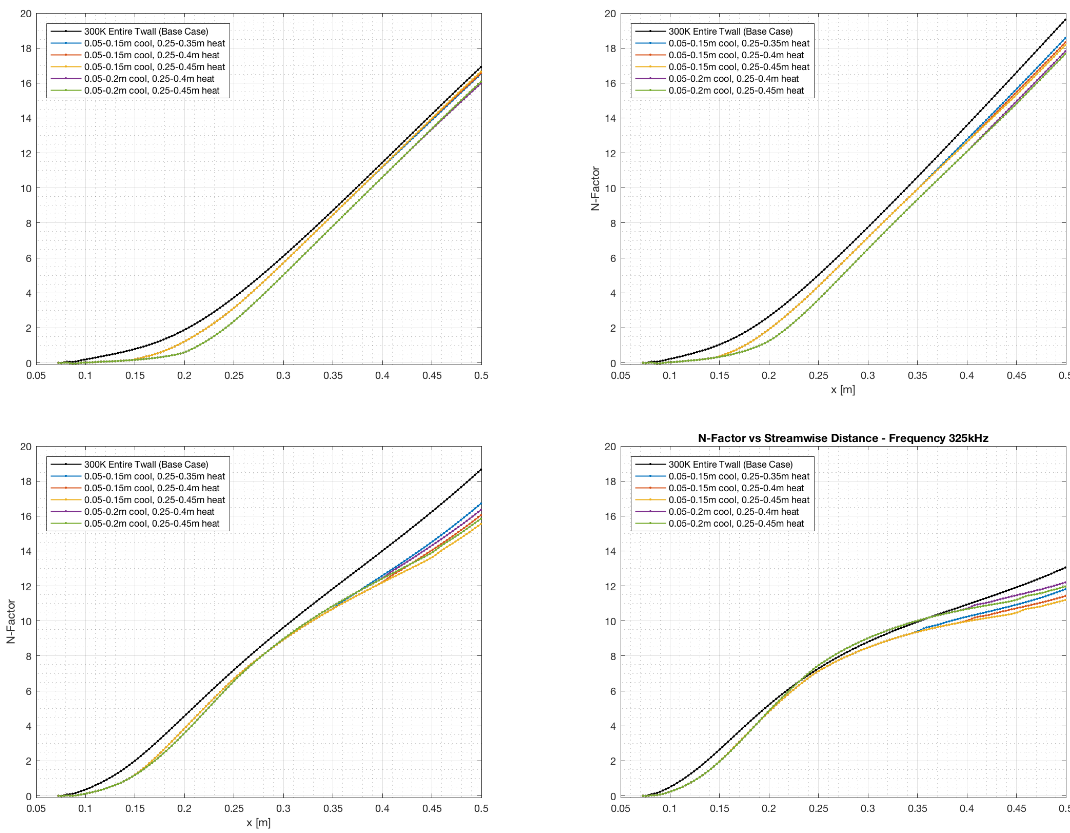

Figure 8.14: LPSE N-factor results - Optimal cases cool/heat wall combination localized strips.

wall suppressed second-mode growth and shifted the most unstable disturbances to lower frequencies. This can be physically understood as an increase in the thermoacoustic impedance well length scale. Note that wall heating is often associated with enhanced first-mode instability, though here we have not conducted a first-mode analysis. Similarly, cooling the entire wall enhanced second-mode growth and shifted the most unstable disturbances to higher frequencies. This can be physically understood as a decrease in the thermoacoustic impedance well length scale.

It is extremely interesting to observe that the effect of combined cooling (over the upstream portion of the cone) and heating (over the downstream portion of the cone) provides a stronger level of second-mode control than heating only. This can be

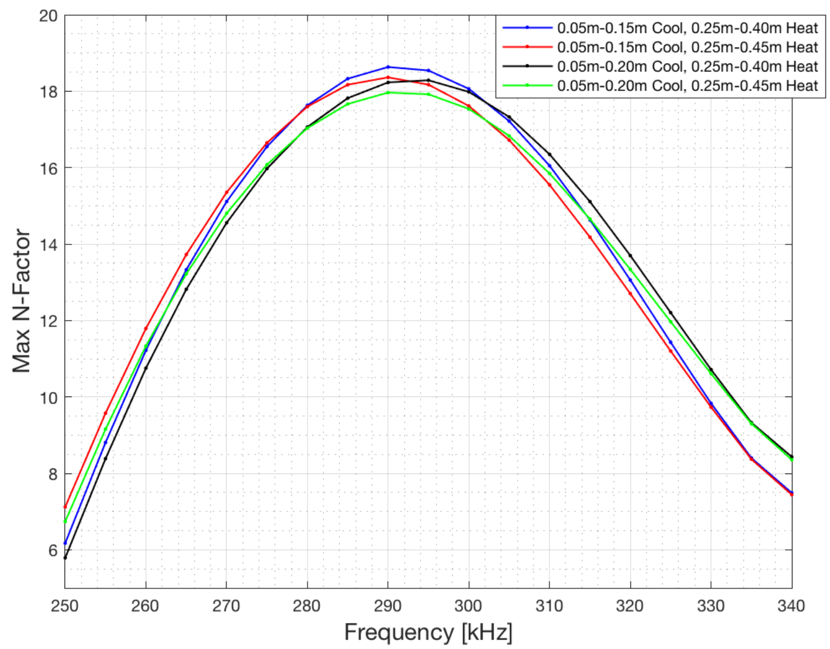

Figure 8.15: LPSE N-factor results - Optimal cases cool/heat wall combination localized strips spectrum plot.

understood by returning to figure 8.2. The affect of cooling is to shift the stability diagram towards higher frequencies, while the affect of heating is to shift the stability diagram to lower frequencies. Thus the combined effect on the stability diagram is an effective clockwise rotation. Each individual frequency disturbance has a smaller streamwise distance over which it is resonant (ie growing), which accounts for the N-factor reduction. Furthermore, we note that the 'ideal' case of cooling or heating over the entire length of the cone is impractical. However, we see that similar results to the 'ideal' case can be achieved using finite length (localized) cooling and heating strips. This 'optimal' case of finite length strips provides a level of second-mode damping which surpasses heating of the entire wall and only slightly less effective the the ideal case. Finally, we conjecture that the localized heating and cooling strips will be less susceptible to first-mode instability. This conjecture is the subject of on-going work, and is based on the idea that the heating effects are restricted to a smaller region of

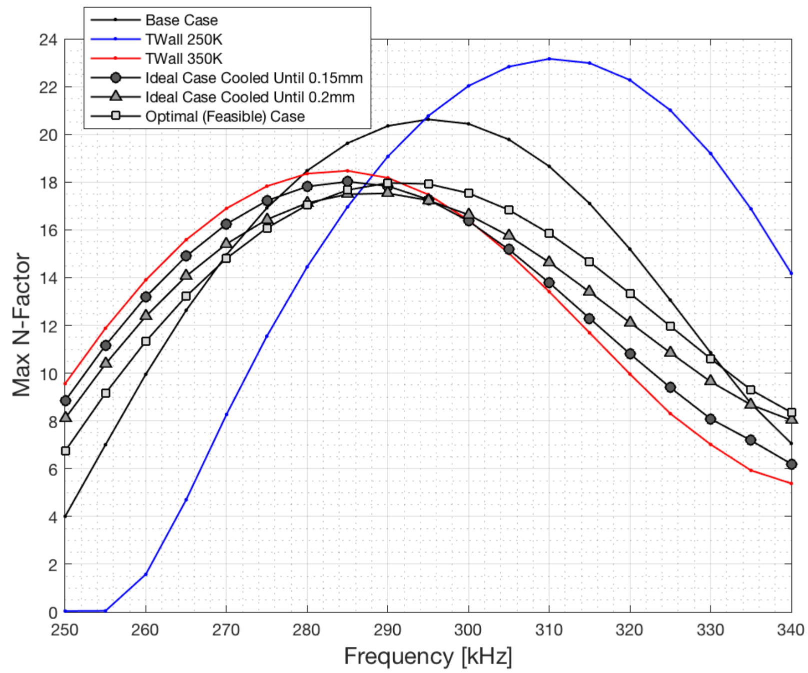

Figure 8.16: LPSE Max N-factor vs frequency spectrum plot comparing: base case with no cooling/heating, entire wall cooled, entire wall heated, the ideal (limiting) cases, and the optimal (feasible) case

the flow, thus any first-mode enhancement would be similarly mitigated.

8.3.6 Findings

The aforementioned results provided a motivation for the use of active thermocouple or passive material selection methods to dampen second-mode growth. Recapping, there are several important implications of the presented results, as well as some new directions for future investigation.

1. If wall cooling or heating is performed alone, then one might dampen the disturbance at a specific frequency, but excite greater growth at another frequency. These results show that a combination of upstream cooling and downstream heating mitigates this effect.

2. That cooling on the upstream portion of the cone dampens second-mode growth and heating on the upstream portion of the cone amplifies growth, and vice versa.

3. Wall cooling and heating physically affect second-mode growth through modification of the acoustic impedance well.

4. The combination of upstream cooling and downstream heating can be interpreted as a clockwise rotation of the stability diagram.

5. Downstream heating has an overall greater damping effect than upstream cooling.

6. Once past the localized region of heating or cooling, the velocity and density gradients relax to the undisturbed basic state behavior.

7. It was shown that a finite length combination of cooling and heating strips can lower max N-factors to similar levels as entire length wall temperature alterations, but in a more feasible manner.

8. Further investigation is needed to study the effect of localized heating and cooling on first-mode instability.

9. Further investigation is needed to quantify the influence of localized wall cooling/heating on the non-linear behavior of second-mode waves, particularly concerning finite-bandwidth effects, side-lobe generation, and spectral broadening.

Chapter 9

SUMMARY

9.1 Discussion

9.1.1 Research Applications and Implications of Wavepackets

The contributions fulfilling this objective are manifold. Recall, wavepackets represent the finite bandwidth nature of second-mode disturbances compared to traditional delta functions in nonlinear analysis resulting in the following implications. First, a more consistent scenario for spectral broadening utilizing wavepackets was shown, capturing the nonlinear dynamics of boundary layer disturbance growth more accurately. Second, spectral broadening is driven by the nonlinear energy feedback of the harmonics onto the primary disturbance inducing side lobe growth. Third, that low frequency disturbance content (ie. low frequency noise), is a consequence of spectral broadening, not the cause of it [42, 43, 46].

9.1.2 PSE and Experimental Data Comparison

Comparison of experiments and NPSE were completed [42, 43]. These comparisons were important not only for disturbance amplitude comparison, but also for the modeling the onset streamwise location of spectral broadening. Encapsulated within comparing the NPSE to experimental data, iterative improvements were made to the JoKHeR. This included automations and updates to the code for LST, LPSE, and NPSE. Additionally, NPSE was updated to support improved wavepacket formulations and testing. The first was using: 3 primary disturbances (1 primary frequency with 2 side lobe frequencies), a first harmonic + 2 side lobes, and a second harmonic + 2 side lobes. This is instead of only: 1 primary disturbance + side lobes, and a first harmonic with no side lobes. Second was testing side lobe bandwidths to determine which produced better results when comparing to experimental data. Third was testing the sensitivity of overall disturbance growth to disturbance initial conditions. The initial amplitude not only affects the spectral broadening onset location, but also the amplitude ratio of the primary disturbance divided by the first harmonic. Fourth, was increasing the number of modes from 3 to 5 to 7 to 9. For instance, the tested frequencies for the 5 mode case were: 300, 285, 315, 270, 330khz, with 5 mode first and second harmonics included. Once these improvements were made, the total disturbance amplitudes calculated with the NPSE were between 20-40%, which is a consistent range when compared with the approximate 30% total disturbance amplitude measured in experiments with similar spectral broadening onset.

A couple of side notes are also worth mentioning. Since it was found that increasing the number of modes from 3 to 5 to 7 improved the PSE results, it can be surmised that it is logical to try more modes. However, it was also found in this case that adding modes beyond 9 makes the calculation take substantially longer, is less stable, and protrudes into diminishing returns for capturing the physics. Along the way, several low frequency content (noise) frequencies were tested. These included: 25, 30, 50, 100, and 150khz, all of which only growing after spectral broadening had set in, and not before. This continues to show evidence that low frequency noise does not cause spectral broadening. Finally, spectral broadening is an indication that nonlinearities are asserting themselves in the disturbance flow field. In other words, the streamwise region where spectral broadening occurs, implies linear models, or even nonlinear models which do not include the finite bandwidths of disturbances, will miss some of the flow physics and disturbance amplitude.

9.1.3 PSE and DNS Comparison

The NPSE results were also compared to collaborators' DNS results and overall good agreement was found [45]. In other words, the NPSE solver has been validated against both experimental and numerical results. Therefore, assuming properly defined: initial conditions, number of modes, and side lobe bandwidth, the wavepacket NPSE formulation will sufficiently capture weak to moderate nonlinear disturbance physics for second-mode amplitude growth.

9.1.4 Applications and Implications of the Thermoacoustic Interpretation Regarding Second-mode Instability

The contributions with respect to the thermoacoustic interpretation are as follows. Recall, the blunt body paradox, which considers the downstream movement of transition with increased nose bluntness, then jumps upstream at a critical nose radius. The downstream movement mechanism of the transition front was quantified in this research by testing 7 degree half angle straight cones at AFOSR-Notre Dame Large Mach 6 Quiet Tunnel conditions. First, entropy contour plots of each cone showed substantial entropy layer increases with larger nose bluntness, as expected. The entropy layer swallowing length was consistent with the results that second-modes were suppressed in this region (Stetson 1983, Juliano 2015, and Tufts and Kimmel 2017). Then, applying the thermoacoustic interpretation, it was verified using LPSE and density gradient results that the second-modes were indeed being suppressed within the entropy layer swallowing length and present afterwards. Further, a criterion was developed to quantify this behavior using the generalized inflection point criterion $(\rho U')' = \rho U'' + \rho' U'$ (Lees and Lin 1946) to estimate the required density gradient strength for second-mode resonance to occur. Considering the zero point crossing or: $\|\hat{U}'\| = \bar{U}'$ and $\|\hat{\rho}'\| = \bar{\rho}'$. That is, second-mode instability was present when analyzing the data at the zero point crossing $\|\hat{\rho}'\| > \|\hat{U}'\|$, and suppressed otherwise, such that: $\hat{\rho}' = -\frac{\rho U''}{U'}$ and $\hat{U}' = -\frac{\rho U''}{\rho'}$. This identified the physical mechanism of second-mode suppression by nose bluntness: entropy layer modification of the acoustic impedance well. In the future work chapter, the transition front upstream movement research is suggested.

9.1.5 Utilize the Thermoacoustic Interpretation to Develop a New Control Method

The last objective was fulfilled by the contribution of applying the thermoacoustic interpretation to study a novel method for controlling second-mode growth via wall heating and cooling. It was shown that the best method applies a combination of upstream wall cooling and downstream wall heating. Furthermore, the mechanisms for this damping behavior were identified, which is a new contribution to the field. Cooling the wall disturbs the thermoacoustic impedance well by decreasing the density gradient height scale tuning higher frequencies, and heating increases the density gradient height scale, tuning lower frequencies. This can be interpreted as a clockwise rotation of the stability diagram, which then presents a smaller streamwise cross-section over which disturbance amplitude grows. Thereby, lowering total disturbance growth. Finally, it was shown that clever placement of the cooling and heating strips can produce similar levels of second-mode damping to an ideal case of total wall cooling/heating in combination than even total wall heating.

9.2 Research Summary

In summary, the goal of this research was to better understand the physical mechanisms governing second-mode instability, such that they may be appropriately modeled numerically for improved amplitude based prediction of hypersonic boundary layer stability and transition. The aforementioned published results completed all 5 research objectives, which have been reprinted and abbreviated below. Objectives 1 through 3 were achieved by four published contributions summarized in chapters 4, 5, and 6 [42, 43, 45]. Objectives 4 and 5 were achieved by two published contributions summarized in chapters 7 and 8 [79, 80].

9.2.1 Wavepackets

1. Research Applications and Implications

2. PSE and Experimental Data Comparison

3. PSE and DNS Comparison

9.2.2 Thermoacoustic Interpretation

4. Applications and Implications of the Thermoacoustic Interpretation Regarding Second-mode Instability

5. Utilize the Thermoacoustic Interpretation to Develop a New Control Method

Chapter 10
FUTURE WORK

In this chapter suggested future work is presented. There are many directions which can be taken in hypersonic boundary layer stability and transition. So, only the major extensions of the completed topics covered in this dissertation will be proposed.

10.1 Adjoint Methods

10.1.1 The Blunt Body Paradox

In chapter 7, it was mentioned that the downstream transition movement mechanism was quantified for the blunt body paradox. The next step is to determine the upstream transition movement upon reaching a sufficiently large nose radius (critical bluntness). A compressible adjoint (left eigenvalue problem) solver may be able to use the results from this research, and backward solve to determine the mechanisms for the upstream transition jump.

10.1.2 Initial Condition Amplitude Determination for Nonlinear Parabolized Stability Equations

As was shown in chapter 5, instability behavior has significant sensitivity to disturbance amplitude initial conditions, which is consistent with nonlinear dynamics theory [81]. In this research many disturbance amplitude initial conditions had to be hard coded and tested while performing NPSE. An adjoint solver study may be able to determine proper initial conditions to be used. This data could then be inputted into future NPSE runs for more accurate and/or faster nonlinear analyses.

10.1.3 Angle of Attack Analysis

Kuehl, Perez, and Reed (2012) showed NPSE results on a 7 degree, half-angle straight yawed cone, at a 6 degree angle of attack at Mach 6 [9, 82]. Consider figure 10.1 which plots wall normal direction y versus non-dimensional density ρ/ρ_∞. It can be seen, that there is similar behavior to the Notre Dame cones from chapter 7 where increased nose bluntness caused a shift in the impedance well. This may be another application opportunity for the thermoacoustic interpretation. The first step would be to plot the square root of density of similar yawed cone data in figure 10.1 to verify the shifting behavior. Next, the cone's angle of attack could be varied to detect shifts in the thermoacoustic impedance well. The purpose of this process would be to determine how the impedance well shifts with increasing angle of attack until a critical angle of attack where transition would jump upstream analogous to the blunt body paradox is potentially reached.

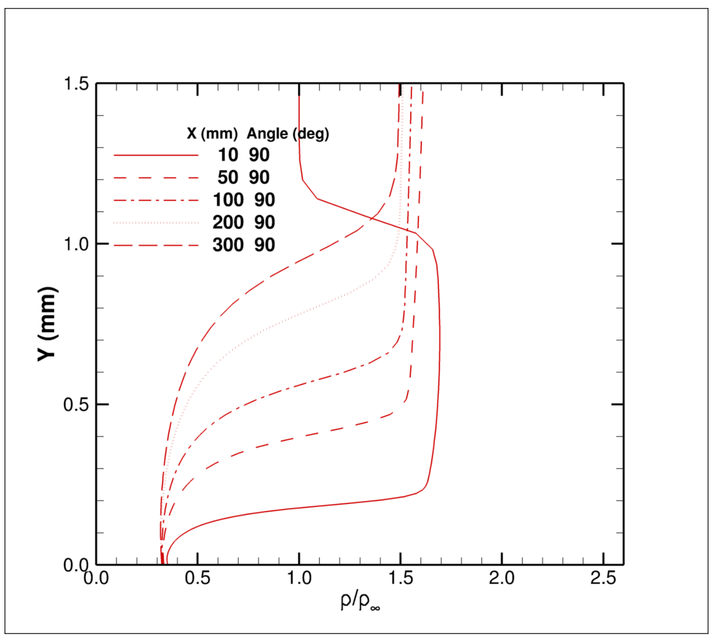

Figure 10.1: 7 degree half angle straight yawed cone at a 6 degree angle of attack at Mach 6. Plot is wall normal (y) vs ρ/ρ_∞ at various streamwise locations [9, 82]

10.2 Acoustic Impedance Well Shifts

It has been observed that second-mode frequency shifts as the disturbance moves downstream. This shift is caused by asymmetry from the pitch or yaw of the test article, from the geometry varying in height, and/or the boundary layer growing in height. This changes the relative the thermoacoustic impedance well height too. As such, a variable frequency NPSE is suggested to study this phenomenon. There appears to be a relation among the disturbance frequency shift, currently being referred to as the frequency divergence angle. As another part of this, the thermoacoustic interpretation may have implications towards this shifting frequency, and applying it to the PSE may further improve amplitude predictions.

10.3 First-Mode Control Using Wall Temperature Strips

As was mentioned in chapters 2 and 8, first-modes behave oppositely to second-modes with respect to wall heating and cooling. As such, wall heating tends to be discouraged, since although it may dampen second-modes, it amplifies first-modes. This is of particular concern at Mach numbers below 4. However, the novel control method in this research performs upstream cooling. Since cooling dampens first-modes, the cool/heat strip combination may mitigate the wall heating alone shortcoming. This is the subject of on-going work.

10.4 Wall Temperature Strips Data Comparison

A comparison of experiments and/or DNS would be very beneficial to verify the results from this research of the cool/heat strips. Additionally, a full nonlinear analysis would also help to verify that nonlinear growth is delayed, and the determination of any potential changes to the onset of spectral broadening.

10.5 Instability Interactions

10.5.1 Additional Instabilities and Interactions NPSE Implementation

Hot-cold-hot streaks were shown in the experimental and DNS collaborator results in the Mach 6 flared cone review paper summarized in chapter 5. Including oblique modes, Gortler modes, and K-type interactions into the wavepacket formulation of NPSE, may be able to capture this phenomenon, when compared to the aforementioned data.

10.5.2 First-Second-Mode Interaction

Finally, this research focused on second-mode instabilities. Since the Mach number studied was 6, this was a reasonable assumption since Mack showed in general second-modes tend to dominate above Mach 4 [19]. However, there may be an interaction of the first and second-mode between Mach 4 and 6 which could cause different instability behavior. This is also the subject of on-going work.

REFERENCES

[1] J. D. Anderson Jr. *Hypersonic and High-Temperature Gas Dynamics.* AIAA Education Series, 2nd edition edition, 2006.

[2] M. Lewis. *Hypersonic Flight: Progress and Challenges on the Way to High Mach Systems.* AIAA Presentation, 2018.

[3] E. H. Hirschel. *Basics of Aerothermodynamics.* Springer, 2nd edition edition, 2015.

[4] H. L. Reed, R. Kimmel, S. Schneider, D. Arnal, and W Saric. Drag prediction and transition in hypersonic flow. *AGARD Conference Proceedings*, 3:C15–C15, 1997.

[5] C. Peebles. *Road to Mach 10: Lessons Learned from the X-43A Flight Research Program.* AIAA, 2006.

[6] L. M. Mack. Boundary-layer linear stability theory. *AGARD Report 709*, 1984.

[7] J. J. Kuehl. Discrete- and finite-bandwidth-frequency distributions in nonlinear stability applications. *Physics of Fluids*, 29:024101–1–024101–8, 2017, 2017.

[8] J. Kuehl. Thermoacoustic interpretation of second-mode instability. *AIAA Journal*, doi:https://doi.org/10.2514/1.J057015, 2018.

[9] J. Kuehl, E. Perez, and H. L. Reed. Jokher: Npse simulations of hypersonic crossflow instability. *AIAA Paper 2012-0921*, 2012.

[10] B. C. Chynoweth. A new roughness array for controlling the nonlinear breakdown of second-mode waves at mach 6. *Purdue University, Master's Thesis*, 2015.

[11] B. C. Chynoweth. Measurements of transition dominated by the second-mode instability at mach 6. *Purdue University, Ph.D. Dissertation*, 2018.

[12] Frank M. White. *Viscous Fluid Flows.* McGraw-Hill, 3rd edition edition, 2006.

[13] P. K. Kundu, I. M. Cohen, and D. R. Dowling. *Fluid Mechanics.* Academic Press (Elsevier), 6th edition edition, 2016.

[14] A. Fedorov. Transition and stability of high-speed boundary layers. *Annual Review of Fluid Mechanics*, 43:79–95, 2011.

[15] E. Reshotko. Physics of fluids. *Transient growth: A factor in bypass transition*, 13:1067–1075, 2001.

[16] T. Herbert. Parabolized stability equations. *Annual Review Fluid Dynamics*, 29:245–283, 1997.

[17] P. G. Drazin. *Stability and Transition in Shear Flows*, volume 32. Springer, Applied Mathematical Science, 1st edition edition, 2002.

[18] P. J. Schmid and D. S. Henningson. *Stability and Transition in Shear Flows*, volume 142. Springer, Applied Mathematical Science, 6th edition edition, 2001.

[19] L. M. Mack. Boundary-layer stability theory. *Jet Propulsion Laboratory, Pasadena, CA.*, 900-277 Rev. A, 1969.

[20] W. S. Saric. Experiments in 3-d boundary layers: Stability and receptivity. *NATO Report*, RTO-EN-AVT-151, Paper 8:8–1–8–28, 2009.

[21] H. L. Reed. Computational methods for 3-d and supersonic flows. *NATO Report*, RTO-EN-AVT-151, Paper 1:11–1–11–24, 2009.

[22] J. J. Kuehl and P. Paredes. Gortler modified mack-modes on a hypersonic flared cone. *AIAA Paper 2016-0849*, 2016.

[23] H. L. Reed. Stability of hypersonic boundary - layer flows. *AFOSR-TR-97 Report*, 1997.

[24] J. Kuehl, H. Reed, T. Kocian, and N. Oliviero. Bandwidth effects on mack-mode instability. *AIAA Paper 2014-2777*, 2014.

[25] J. Kuehl. Nonlinear saturation versus nonlinear detuning: Quantification on a mach 6 flared cone. *AIAA Paper 2017-0763*, 2017.

[26] H. Fasel, J. Sivasubramanian, and A. Laible. Numerical investigation of transition in a flared cone boundary layer at mach 6. *Procedia IUTAM*, 14:26–35, 2015.

[27] J. Hofferth, W. Saric, J. Kuehl, E. Perez, T. Kocian, and H. Reed. Boundary-layer instability and transition on a flared cone in a mach 6 quiet wind tunnel. *International Journal of Engineering Systems Modelling and Simulation*, 5:109–124, 2013.

[28] T. Kocian, E. Perez, N. Oliviero, J. Kuehl, and H. Reed. Hypersonic stability analysis of a flared cone. *AIAA Paper 2013-0667*, 2013.

[29] E. Reshotko and A. Tumin. The blunt body paradox - a case for transient growth. *Laminar-Turbulent Transition. IUTAM Symposia (International Union of Theoretical and Applied Mechanics). Springer, Berlin, Heidelberg*, pages 403–408, 2000.

[30] P. Paredes and F. Choudhari, M. M. and. Li. Blunt-body paradox and transient growth on a hypersonic spherical forebody. *Physical Review Fluids*, 053903(2), 2017.

[31] P. Paredes, M. M. Choudhari, and F. Li. Blunt-body paradox and improved application of transient-growth framework. *AIAA Journal*, 56(7), 2018.

[32] E. C. Marineau, C. G. Moraru, J. D. Lewis, D. R.and Norris, J. F. Lafferty, R. M. Wagnild, and J. A. Smith. Mach 10 boundary-layer transition experiments on sharp and blunted cones. *AIAA Paper 2014-3108*, 2014.

[33] E. C. Marineau, G. C. Moraru, D. R. Lewis, J. D. Norris, J. Lafferty, and H. B. Johnson. Investigation of mach 10 boundary layer stability of sharp cones at angle-of-attack, part 1: Experiments. *AIAA Paper 2015-1737*, 2015.

[34] M. Tufts and R. L. Kimmel. Analysis of windward side hypersonic boundary layer transition on blunted cones at angle of attack. *AIAA Paper 2017-0764*, 2017.

[35] T. J. Juliano, R. L. Kimmel, S. Willems, A. Gulhan, and R. M. Wagnild. Hifire-1 boundary-layer transition: Ground test results and stability analysis. *AIAA Paper 2015-1736*, 2015.

[36] K. F. Stetson. Nosetip bluntness effects on cone frustum boundary layer transition in hypersonic flow. *16th AIAA Fluid and Plasmadynamics Conference, AIAA Paper 1983-1763*, 1983.

[37] S. P. Schneider. Developing mechanism-based methods for estimating hypersonic boundary-layer transition in flight: The role of quiet tunnels. *Progress in Aerospace Sciences*, 72:17–29, 2014.

[38] S. P. Schneider. Development of hypersonic quiet tunnels. *Journal of Spacecraft and Rockets*, 45, 2008.

[39] K. M. Casper, S. J. Beresh, and S. P. Schneider. Pressure fluctuations beneath instability wavepackets and turbulent spots in a hypersonic boundary layer. *Journal of Fluid Mechanics*, 756:1058–1091, 2014.

[40] B. C. Chynoweth, Christopher A. C. Ward, Roger T. Greenwood, Gregory R. McKiernan, Roy A. Fisher, and Steven P. Schneider. Measuring transition and instabilities in a mach 6 hypersonic quiet wind tunnel. *AIAA Paper 2014-2643*, 2014.

[41] G. McKiernan, B. Chynoweth, and S. P. Schneider. Instability and transition experiments in the boeing/afosr mach 6 quiet tunnel. *AIAA Paper 2015-1735*, 2015.

[42] B. Chynoweth, S. P. Schneider, H. Fasel, C. Hader, A. Batista, J. Kuehl, T. J. Juliano, and B. Wheaton. A history and progress of research on boundary-layer transition on a mach 6 flared cone. *AIAA Paper Scitech 2018-0060*, 2018.

[43] B. Chynoweth, S. P. Schneider, H. Fasel, C. Hader, A. Batista, J. Kuehl, T. J. Juliano, and B. Wheaton. A history and progress of research on boundary-layer transition on a mach 6 flared cone. *Journal of Spacecraft and Rockets*, 56(2), 2019.

[44] H. L. Reed, E. Perez, J. Kuehl, T. Kocian, and N. Oliviero. Verification and validation issues in hypersonic stability and transition prediction. *Journal of Spacecraft and Rockets*, 52:29–37, 2014.

[45] V. C. B. Sousa, A. Batista, J. Kuehl, and C. Scalo. Nonlinear dynamics of second mode waves on a hypersonic flared cone. *AIAA Aviation Forum Paper 2018-3852*, 2018.

[46] A. Batista and J. Kuehl. A mechanism for spectral broadening and implications for saturation amplitude estimates. *AIAA Aviation Forum Paper 2017-3635*, 2017.

[47] T. Herbert and F. P. Bertolotti. Stability analysis of nonparallel boundary layers. *Bulletin of American Physical Society 32*, 2079, 1987.

[48] M. Gaster. On the effects of boundary-layer growth on flow stability. *Journal of Fluid Mechanics*, 66(3):465–480, 1974.

[49] T. Herbert. Parabolized stability equations. *AGARD Report*, (793):465–480, 1994.

[50] F. P. Bertolotti. Compressible boundary layer stability analyzed with the pse equations. *AIAA Paper No. 91-1637*, 1991.

[51] C. L. Chang, M. R. Malik, G. Erlebacher, and M. Y. Hussaini. Compressible stability of growing boundary layers using parabolized stability equations. *AIAA Paper No. 91-1636*, 1991.

[52] R. D. Joslin, C. L. Streett, and C. L. Chang. 3-d incompressible spatial direct numerical simulation code validation study: A comparison with linear stability and parabolic stability equation theories in boundary-layer transition on a flat plate. *Report No. NASA TP-3205*, 1992.

[53] F. Li and M. R. Malik. On the nature of pse approximation. *Theoretical Computational Fluid Dynamics*, 8:253–273, 1996.

[54] M. Gaster. Simulation of swept-wing vortices using nonlinear parabolized stability equations. *Journal of Fluid Mechanics*, 405(3):325–349, 2000.

[55] G. Stuckert and H. Reed. Linear disturbances in hypersonic, chemically reacting shock layer. *AIAA Journal*, 32(7):1384–1393, 1994.

[56] C. L. Chang, H. Vinh, and M. R. Malik. Hypersonic boundary-layer stability with chemical reactions using pse. *AIAA Paper No. 97-2012*, 1997.

[57] H. B. Johnson, T. G. Seipp, and G. V. Candler. Numerical study of hypersonic reacting boundary layer transition on cones. *Physics of Fluids*, 10(10):2676–2685, 1998.

[58] M. R. Malik. Hypersonic flight transition data analysis using parabolized stability equations with chemistry effects. *Journal of Spacecraft and Rockets*, 40(3):332–344, 2003.

[59] C. L. Chang. The langley stability and transition analysis code (lastrac) version 1.2 user manual. *Report No. NASA/TM-2004-213233*, 2004.

[60] H. B. Johnson and G. V. Candler. Hypersonic boundary layer stability analysis using pse-chem. *AIAA Paper 2005-5023*, 2005.

[61] F. Li, M. Choudhari, C. L. Chang, and J. White. Analysis of instabilities in non-axisymmetric hypersonic boundary layers over cones. *10th AIAA/ASME Joint Thermophysics and Heat Transfer Conference*, 2010.

[62] V. Theofilis. Global linear instability. *Annual Review of Fluid Mechanics*, 43:319–352, 2011.

[63] P. Paredes, V. Theofilis, D. Rodriguez, and J. A. Tendero. The pse-3d instability analysis methodology for flows depending strongly on two and weakly on the third spatial dimension. *AIAA Paper 2011-3752*, 2011.

[64] E. Perez, T. S. Kocian, J. Kuehl, and H. L. Reed. Stability of hypersonic compression cones. *AIAA Paper AIAA Paper 2012-2962*, 2012.

[65] J. Kuehl and A. Batista. The influence of multiple interacting primary modes and mode representation on hypersonic boundary-layer stability and transition prediction. *Air Force Office of Scientific Research Presentation, NASA Langley Research Center*, 2017.

[66] I. Nompelis, T. Drayna, and G. Candler. Development of a hybrid unstructured implicit solver for the simulation of reacting flows over complex geometries. *AIAA Paper 2004-2227*, 2004.

[67] I. Nompelis, T. Drayna, and G. Candler. A parallel unstructured implicit solver for hypersonic reacting flow simulation. *AIAA Paper 2005-4867*, 2005.

[68] G. V. Candler, H. B. Johnson, I. Nompelis, P. K. Subbareddy, T. W. Drayna, V. Gidzak, and M. D. Barnhardt. Development of the us3d code for advanced compressible and reacting flow simulations. *AIAA Paper 2015-1893*, 2015.

[69] J. Sakakeeny. Linear stability theory analysis of mach 10 nitrogen flow over 7-deg half-angle cones. *Baylor University, Master's Thesis*, 2017.

[70] R. J. Lingwood. On the application of en-methods to three-dimensional boundary-layer flows. *European Journal of Mechanics - B/Fluids*, 18:581–620, 1999.

[71] B. Wheaton, T. Juliano, D. Berridge, A. Chou, P. Gilbert, K. Casper, L. Steen, S. Schneider, and H. Johnson. Instability and transition measurements in the mach-6 quiet tunnel. *AIAA Paper 2009-3559*, 2009.

[72] S. Willems, C. A. Ward, and S. P. Schneider. Free transition on a slender cone in a quiet and a conventional wind tunnel and the effect of ultrasonically absorptive materials. *Presented at the 6th European Conference for Aeronautics and Space Sciences*, 2015.

[73] C. Hader and H. F. Fasel. Fundamental resonance breakdown for a flared cone at mach 6. *AIAA Paper 2017-0765*, 2017.

[74] C. Hader and H. F. Fasel. Laminar-turbulent transition on a flared cone at mach 6. *AIAA Paper 2016-3344*, 2016.

[75] K. F. Stetson and R. L. Kimmel. Example of second-mode instability dominance at a mach number of 5.2. *AIAA Journal*, 30(12):2974?2976, 1992.

[76] M. T. Lakebrink, K. G. Bowcutt, T. Winfree, C. C. Huffman, and T. J. Juliano. Optimization of a mach-6 quiet wind tunnel nozzle. *Journal of Spacecraft and Rockets*, 55(2):315–321, 2018.

[77] K. D. Fong, X. Wang, Y. Huang, X. Zhong, G. R. McKiernan, R. A. Fisher, and S. P. Schneider. Second mode suppression in hypersonic boundary layer by roughness: Design and experiments. *AIAA Journal*, 53(10), 2015.

[78] R. Zhao, C. Y. Wen, X. D. Tian, T. H. Long, and W. Yuan. Numerical simulation of local wall heating and cooling effect on the stability of a hypersonic boundary layer. *International Journal of Heat and Mass Transfer*, 121:986–998, 2018.

[79] A. Batista, A. A. Khan, and J. Kuehl. On the mechanism by which nose bluntness suppresses second-mode instability. *AIAA Journal*, Under Review, 2019.

[80] A. Batista and J. Kuehl. Implications of local wall temperature variations on second-mode instability. *AIAA Aviation Paper 2019 Accepted*, 2019.

[81] S. H. Strogatz. *Nonlinear Dynamics and Chaos With Applications to Physics, Biology, Chemistry, and Engineering*. Westview Press, 2nd edition edition, 2015.

[82] P. Balakumar and L.R. Owens. Stability of hypersonic boundary layers on a cone at angle of attack. *AIAA Paper 2010-4718*, 2010.

[83] J. D. Anderson Jr. *Fundamentals of Aerodynamics*. McGraw-Hill, 5th edition edition, 2011.

[84] J. D. Anderson Jr. *Modern Compressible Flow With Historical Perspective*. McGraw-Hill, 3rd edition edition, 2002.

[85] Mythealias. Obliqueshockanglerelation.png. *Wikimedia Commons*, 2007.

[86] K. J. Devlin. *The Millennium Problems*. Basic Books, 2003.

Appendix A

HIGH-SPEED FLUID DYNAMICS OVERVIEW

A.1 Governing Equations of Fluid Mechanics

The purpose of this appendix is to provide the reader with a brief overview or reference to high-speed flow and the related equations in the context of hypersonic flow [1]. Further, this is from the perspective that if the reader is already familiar with these topics, then the reader can jump immediately into chapter 2, otherwise, this may be a good starting point before proceeding. The approach taken in this appendix is with increasing Mach number, common simplifications made to the governing equations can no longer be applied (ie. the simplified Navier-Stokes equations to solve Couette flow has a closed form solution). This is because as Mach number increases more physics must be considered. We start with the governing equations of motion and state for compressible flow.

A.1.1 Conservation of Mass

Continuity [1]:

$$\frac{\partial \rho}{\partial t} + \nabla \cdot (\rho \mathbf{V}) = 0 \tag{A.1}$$

A.1.2 Conservation of Momentum

x-Momentum [1]:

$$\rho\left(\frac{\partial u}{\partial t} + u\frac{\partial u}{\partial x} + v\frac{\partial u}{\partial y} + w\frac{\partial u}{\partial z}\right) = -\frac{\partial p}{\partial x} + \frac{\partial \tau_{xx}}{\partial x} + \frac{\partial \tau_{yx}}{\partial y} + \frac{\partial \tau_{zx}}{\partial z} \tag{A.2}$$

y-Momentum [1]:

$$\rho\left(\frac{\partial v}{\partial t} + u\frac{\partial v}{\partial x} + v\frac{\partial v}{\partial y} + w\frac{\partial v}{\partial z}\right) = -\frac{\partial p}{\partial y} + \frac{\partial \tau_{xy}}{\partial x} + \frac{\partial \tau_{yy}}{\partial y} + \frac{\partial \tau_{zy}}{\partial z} \tag{A.3}$$

z-Momentum [1]:

$$\rho\left(\frac{\partial w}{\partial t}+u\frac{\partial w}{\partial x}+v\frac{\partial w}{\partial y}+w\frac{\partial w}{\partial z}\right)=-\frac{\partial p}{\partial z}+\frac{\partial \tau_{xz}}{\partial x}+\frac{\partial \tau_{yz}}{\partial y}+\frac{\partial \tau_{zz}}{\partial z} \tag{A.4}$$

A.1.3 Conservation of Energy

Energy [1]:

$$\rho\left(\frac{DE_0}{Dt}\right)=\rho\dot{q}+\nabla\cdot(k\nabla T)-\nabla\cdot(p\mathbf{V}) \tag{A.5}$$
$$+\frac{\partial \tau_{xx}}{\partial x}+\frac{\partial \tau_{yx}}{\partial y}+\frac{\partial \tau_{zx}}{\partial z}+\frac{\partial \tau_{xy}}{\partial x}+\frac{\partial \tau_{yy}}{\partial y}+\frac{\partial \tau_{zy}}{\partial z}+\frac{\partial \tau_{xz}}{\partial x}+\frac{\partial \tau_{yz}}{\partial y}+\frac{\partial \tau_{zz}}{\partial z}$$

Where: $E_0 = E + \frac{1}{2}V^2$ is denoted as total energy.

A.1.4 Equations of State

Ideal Gas Law [1]:

$$p = \rho RT \tag{A.6}$$

Enthalpy [1]:

$$h = C_p T \tag{A.7}$$

A.1.5 Other

Shear Stresses [1]:

$$\tau_{xy}=\tau_{yx}=\left(\mu\frac{\partial v}{\partial x}+\frac{\partial u}{\partial y}\right) \tag{A.8}$$

$$\tau_{yz}=\tau_{zy}=\left(\mu\frac{\partial w}{\partial y}+\frac{\partial v}{\partial z}\right) \tag{A.9}$$

$$\tau_{zx}=\tau_{xz}=\left(\mu\frac{\partial u}{\partial z}+\frac{\partial w}{\partial x}\right) \tag{A.10}$$

Normal Viscous Stresses [1]:

$$\tau_{xx}=\lambda(\nabla\cdot\mathbf{V})+2\mu\frac{\partial u}{\partial x} \tag{A.11}$$

$$\tau_{yy} = \lambda(\nabla \cdot \mathbf{V}) + 2\mu\frac{\partial v}{\partial y} \tag{A.12}$$

$$\tau_{zz} = \lambda(\nabla \cdot \mathbf{V}) + 2\mu\frac{\partial w}{\partial z} \tag{A.13}$$

Mach Number [1]:

$$M = \frac{V}{a} \tag{A.14}$$

Speed of Sound [1]:

$$a = \sqrt{\gamma RT} \tag{A.15}$$

Ratio of Specific Heats [1]:

$$\gamma = \frac{C_p}{C_v} \tag{A.16}$$

Gas Constant Specific Heat Relation [1]:

$$R = C_p - C_v \tag{A.17}$$

Reynolds Number [1]:

$$Re_x = \frac{\rho V x}{\mu} \tag{A.18}$$

Prandtl Number [1]:

$$Pr = \frac{\mu C_p}{k} \tag{A.19}$$

A.1.6 Inviscid Flow Characteristics

In the most general case, a closed form solution of equations A.1 through A.5 has not yet been determined to date [12]. However, in practical applications, assumptions are made which do yield solutions and much insight. Some of the common explicit assumptions are negligible viscosity (inviscid flow) or viscosity is only important within a thin region near the body's surface (boundary layer), negligible body forces, constant density, 1D or 2D only flow field dependence (symmetry), and irrotationality. Some of the more implied assumptions in fluid mechanics are negligible heat transfer (isothermal), no heat generation, and no chemical reactions / chemical equilibrium (no mass transfer). These assumptions allow one to omit negligible terms and simplify the equations to simpler PDEs, or even ODEs which can be solved.

These assumptions work great for a wide range of fluid applications. However, for high-speed flows, as the fluid increases, these assumptions start to break down. Fortunately, they do not all stop applying at once. In the next section viscosity will be addressed, for now, let's consider the bulk, inviscid flow region, as we march up the Mach number. For instance, consider the figure below where as the Mach number is increased, the fluid exhibits different behaviors which will be addressed in turn [1, 83, 84].

Additional aspects for a highly, increasing Mach number can be seen in figure A.2 below. This figure illustrated how certain assumptions may cause errors in calculations, or miss some of the physics and even chemistry of the flow. For this research, we will focus on the more classical nature regarding fluid mechanics for hypersonic flows at Mach 6 though.

A.1.6.1 Subsonic Flow - Incompressible vs Compressible Flow

At around Mach 0.3, the compressibility of air starts to become a concern, so density can no longer be considered constant. This subsonic and transonic compressible flow region is where commercial aircraft spend much of their time flying in. Incompressibility can be viewed as the first assumption which does not carry over to hypersonic flow.

A.1.6.2 Supersonic Flows

The transonic range is when the global, freestream Mach number range is between $0.8 < \mathrm{M} < 1.0$, and may have a local region where $\mathrm{M} > 1$. Transonic flow has a wide variety of open questions, but these are beyond the scope of this paper. As such, next we move up to supersonic flow where the freestream Mach number is greater than 1. An important aspect of sonic flow ($\mathrm{M} = 1$), is that this is the velocity which an acoustic wave, can propagate within a fluid medium. Also, it corresponds to the

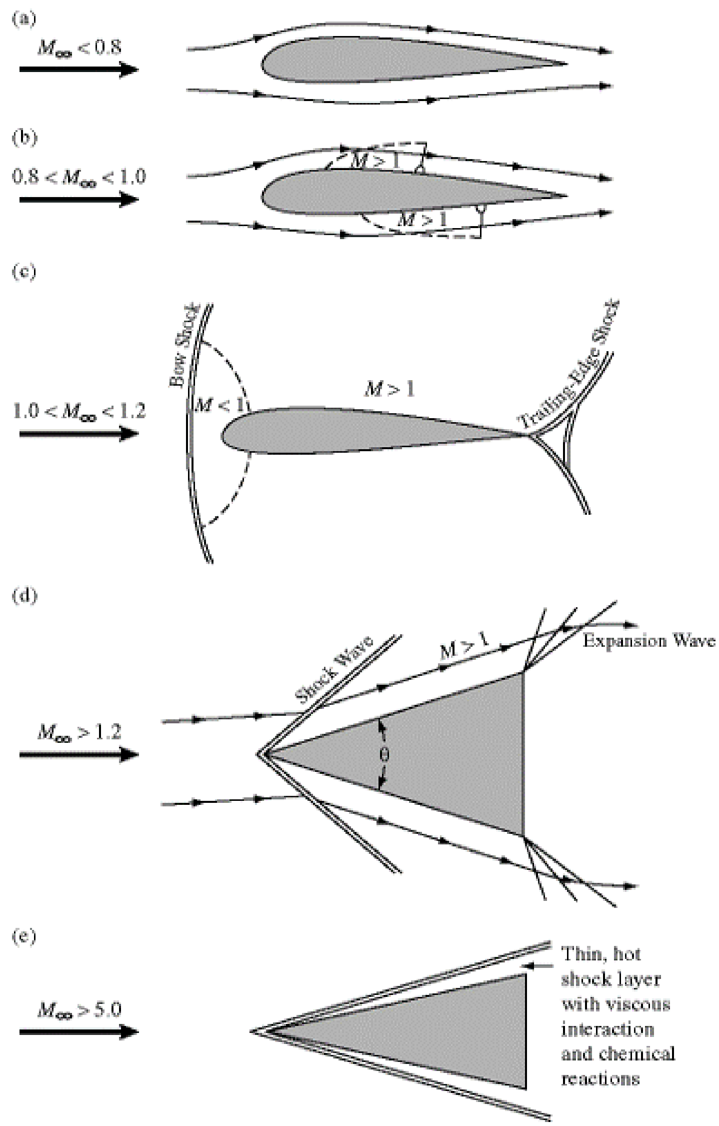

Figure A.1: Walking up the Mach number various flow regimes [83].

limit where information (the molecular forces of the fluid) can communicate to each other. This explains the elliptic terms in the Navier-Stokes equations, and why the computational domain depends on upstream fluid mass, momentum, and energy, not just downstream. Once the flow goes supersonic, the fluid in that region can no longer communicate upstream. As we'll see later, this is taken advantage of in parabolized equations, because a marching scheme can be taken advantage of. For instance, one

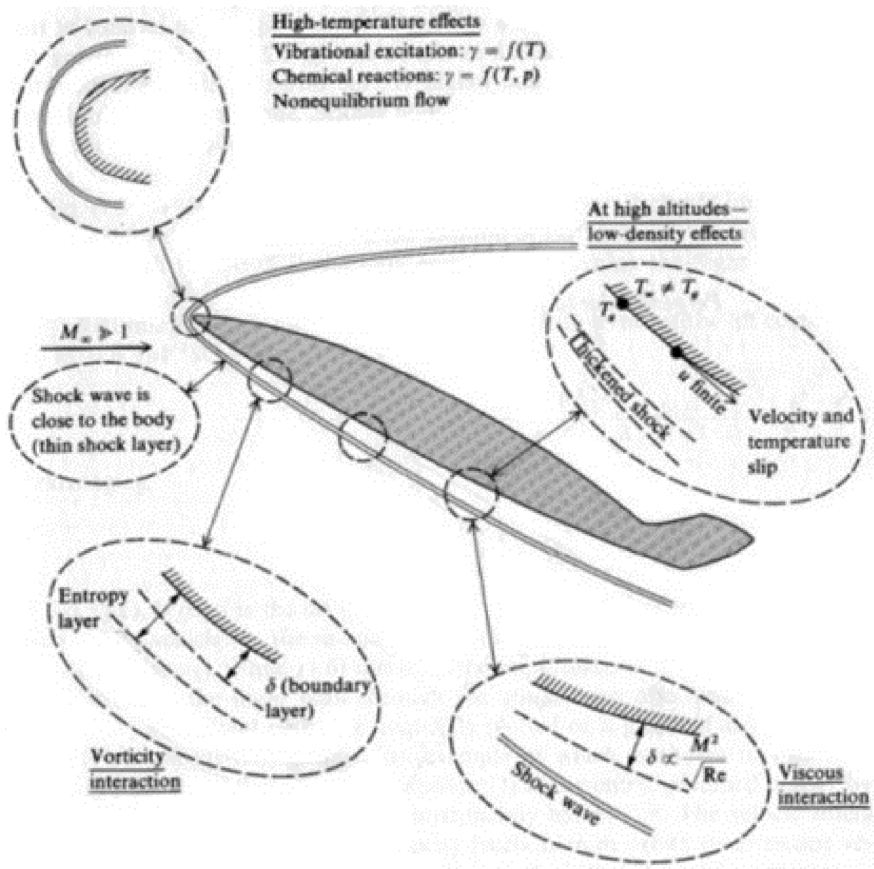

Figure A.2: Hypersonic flow phenomena [83].

may ask, if an air molecule cannot "talk" to the molecule behind it, how does the flow know to change its movement or behavior accordingly when an object is in its path, such as an airfoil or a wedge? This phenomenon is handled via shock waves.

A.1.6.3 Shock Waves

Physically, a shock wave is a region of very large gradients of fluid properties (ie. density, temperature, pressure, velocity, and entropy). Mathematically, it is a discontinuity of the flow field's parameters [1]. Intuitively, the dilemma of a supersonic flow which needs to slow down or speed up due to an object's presence or significant pressure change is "handled" by nature through shocks and expansion waves.

There are two main types of shock waves, normal shocks and oblique shocks. A normal shock is shock wave which forms normal to the flow's direction [83, 84]. Some examples are the region along the pathline directly perpendicular to a body such as the nose of an aircraft, an adverse pressure gradient such as a blast wave, or inside a rocket nozzle where the ambient pressure is much higher than the nozzle exit pressure. A supersonically traveling fluid always slows to subsonic speeds after passing through a normal shock [83, 84]. An oblique shock, (an obliquely angled shock), changes the fluid's velocity, by changing its direction and magnitude, but it does not necessarily slow it to subsonic velocities [83, 84]. These oblique shocks form in front of streamlined bodies which compress the flow such as a wing, wedge, cone, or in the obliquely angled region of a bow shock [83, 84]. There are two types of oblique shocks: strong and weak. Strong shocks are usually characterized by larger shock angles, slowing the flow to subsonic velocities, and being detached from the object [83, 84]. Whereas weak shocks are often attached, have smaller angles, and do not necessarily slow the fluid to subsonic velocities [83, 84]. The θ-β-Mach diagram shows (see figure A.3) is one tool which shows the relation amongst the object's inclination angle θ, the shock angle β, and the Mach number [83, 84]. The top half is for strong shocks, and the bottom half is for weak shocks. Lastly, bow shocks are essentially a combination of a normal and an oblique shock formed in external flows around a sufficiently blunt body (ie. a re-entry capsule). Figure A.1c shows an example of a bow shock in front of an airfoil.

There are not any pertinent instances of expansion waves in this research, but it is noting that expansion waves are the opposite deflection angle of a supersonic flow to a shock wave. For instance, when a supersonic flow moves entirely past the trailing edge of sharp wing at a positive angle of attack (AoA), the flow expands, which turns the flow back to the direction and accelerates it to freestream conditions [13, 83, 84].

A.1.6.4 Flow Regions

The brief review of supersonic flow and shock waves above provides a basis for understanding the inviscid supersonic flow region. It is important to remember, that

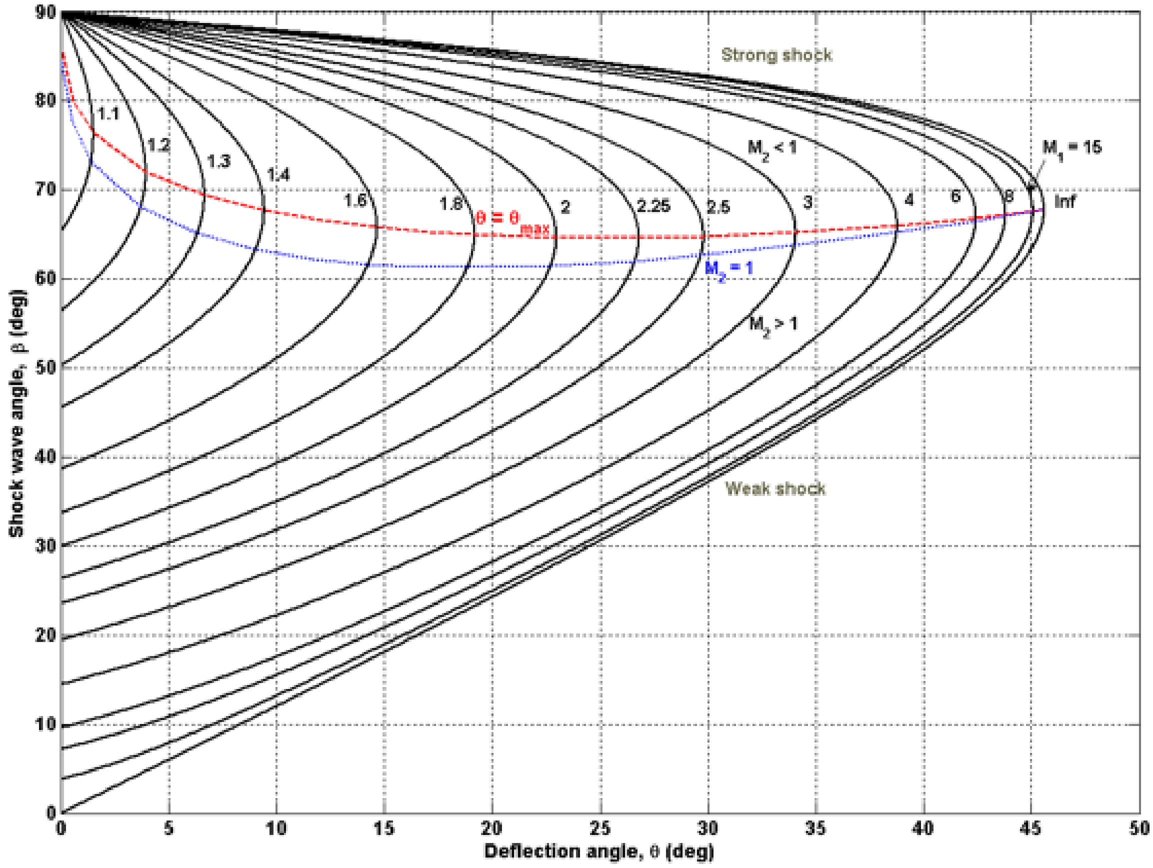

Figure A.3: θ - β - Mach Diagram, depicting the relationship amongst the body turn angle, shock angle, and the freestream Mach number. Also, the determining Mach number for when the oblique shock is weak or strong [83, 84, 85].

this "divide and conquer" perspective is quite powerful for analyzing high-speed flows, it should not be performed in a vacuum. One needs to remember the whole picture, let's consider an example. A jet fighter is flying at Mach 2. The freestream passes through an oblique shock as it nears the wing, slowing the velocity to M $<$ 2 and turning it parallel to the wing's AoA. Next, move closer to the wing measuring the fluid's velocity. One would measure the fluid is slower as we get closer to the wing's surface, at some point reaching a subsonic velocity until reaching a velocity of 0 at the wing's surface by the no-slip condition. Viscosity is the cause for this velocity gradient, the same as in incompressible flow cases [12]. However, unlike the incompressible case, the aforementioned phenomena must be considered. The key takeaway is that high-speed flows are very much a coupled system, and the separation of flow regions can become blurred.

A.1.6.5 Hypersonic Flows

From one perspective, hypersonic flows are simply supersonic flows, where even less simplifications are applicable. Although in general hypersonic flows are usually described as Mach 5 and greater, in the stability sense, low hypersonic flows are often described as starting as low as Mach 3 [1, 38, 83, 84]. For higher hypersonic flows, they are often described as roughly Mach 10 or 15 and higher, depending on gas density and geometry where chemical reactions can begin to occur spontaneously due to the fluid's high speed (Note: This should not be confused with a combustion situation, where chemical reactions occur independent of the flow velocity) [3].

A.1.7 Viscous Flows Characteristics

A.1.7.1 Explicit Solution Cases and Limitations

The previous section discussed the general characteristics and the inviscid flow region with increasing fluid velocity. Now we add viscosity back into the problem. It is well known that the aforementioned Navier-Stokes (N-S) equations describe the full characteristics of fluid flow including viscosity, however, their nonlinear and elliptic nature make solving them explicitly a bit of a chore to say the least [86]. As such, there do exist some explicit solutions to quantify fluid flow (ie. Couette and Poiseulle flows), or by breaking the problem up into an inviscid region and a thin viscous region (Boundary Layer Theory) [12, 13]. More often than not though, experimental and numerical methods are used to capture the physical mechanisms and behavior of fluids.

A.1.8 High-Speed & High-Temperature Effects

A.1.8.1 Translation, Rotational, Vibrational Excitations

So far, as we have marched up the Mach number, several assumptions have been removed, and with viscosity added back in, the full Navier-Stokes equations apply. As the Mach number continues to rise, viscous flows produce large shear and normal stresses which in turn produces more heat on the object. If air which is mostly comprised of N_2 and O_2 is considered, the gas molecules first undergo translational excitation, then rotational excitation, and finally vibrational excitation as the temperature rises above 600K [1]. Various statistical mechanics and kinetic theory of gases are incorporated to capture these effects.

A.1.8.2 Chemical Reactions

Once the air temperature reaches about 2500K, the oxygen begins to dissociated [1, 84]. Now, chemical reactions must also be considered, and the conservation of mass equation becomes multiple equations for mass transfer, one for each chemical compounds or species. If the velocity keeps rising, nitrogen begins to dissociate, adding even more equations [1, 84]. Lastly, at around 9000K the air begins to ionize, and can even form cold plasmas [1, 3]. These phenomena are quite important for re-entry vehicles structures, heat dissipation, and even communications as they travel through the atmosphere at hypersonic speeds between $10 < M < 50$ [1].

Appendix B

PUBLICATION REUSE PERMISSIONS

B.1 Publication Content Reuse Permissions

7/22/2019 RightsLink Printable License

CAMBRIDGE UNIVERSITY PRESS LICENSE
TERMS AND CONDITIONS

Jul 22, 2019

This Agreement between University of Delaware -- Armani Batista ("You") and Cambridge University Press ("Cambridge University Press") consists of your license details and the terms and conditions provided by Cambridge University Press and Copyright Clearance Center.

License Number	4634310955415
License date	Jul 22, 2019
Licensed Content Publisher	Cambridge University Press
Licensed Content Publication	The Journal of Fluid Mechanics
Licensed Content Title	Pressure fluctuations beneath instability wavepackets and turbulent spots in a hypersonic boundary layer
Licensed Content Author	Katya M. Casper, Steven J. Beresh, Steven P. Schneider
Licensed Content Date	Sep 9, 2014
Licensed Content Volume	756
Licensed Content Issue	undefined
Start page	1058
End page	1091
Type of Use	Dissertation/Thesis
Requestor type	Not-for-profit
Portion	Text extract
Number of pages requested	2
Order reference number	
Territory for reuse	North America Only
Title of your thesis / dissertation	Fluid Dynamics Numerical Modeling of Second-Mode Instability Mechanisms at Mach 6
Expected completion date	Aug 2019
Estimated size(pages)	1
Requestor Location	University of Delaware 126 Spencer Lab Newark, DE 19716 United States Attn: University of Delaware
Publisher Tax ID	GB823847609
Total	0.00 USD

https://s100.copyright.com/AppDispatchServlet 1/2

Figure B.1: Permission from Copyright Clearance Center for Journal of Fluid Mechanics article, Casper et al. [39].

G Suite

Armani Batista <abatista@udel.edu>

Results & Figures Citation Permission Request

3 messages

Armani Batista <abatista@udel.edu> Sat, May 18, 2019 at 7:51 PM

To: "Schneider, Steven P" <steves@purdue.edu>, Brandon Chynoweth <bchynowe@purdue.edu>

Hi Prof. Schneider and Brandon,

I'm working on my dissertation, and I wanted to ask permission to cite and include some of the figures from your results in a collaboration section? This is regarding the Scitech and JSR review papers for the flared cone Dr. Kuehl and I worked with both of you on. There are also some pictures I was looking to include and cite in my literature review section on experimental methods which were listed in your dissertation Brandon and other papers published (ie. figures for examples of: the BAM6QT, flared cone, wavepackets, PSD, TSP, etc...)? I fully understand if they cannot be included though, thank you both for all your help and consideration.

Regards,
Armani

Virus-free. www.avg.com

Chynoweth, Brandon C <bchynowe@purdue.edu> Sat, May 18, 2019 at 8:02 PM

To: "Schneider, Steven P" <steves@purdue.edu>, Armani Batista <abatista@udel.edu>

Hi Armani,

I approve use of any figures I have published in papers or my MS Thesis or PhD Dissertation. If you need the figure files just let me know which ones. When you finish, I would be interested in getting a copy of your dissertation.

Regards,

Brandon

Get Outlook for Android

https://mail.google.com/mail/u/0?ik=bf7630729d&view=pt&search=all&permthid=thread-a%3Ar-1792679114758415537&simpl=msg-a%3Ar-55006098821562808… 1/2

Figure B.2: Permission from lead author Brandon Chynoweth for experimental sections and content for reference [42, 43].

Copyright Clearance Center

Confirmation Number: 11831187
Order Date: 07/11/2019

Customer Information

Customer: Armani Batista
Account Number: 3001482668
Organization: University of Delaware
Email: abatista@udel.edu
Phone: +1 (302) 831-2421
Payment Method: Invoice

This is not an invoice

Order Details

Journal of spacecraft and rockets

Billing Status: **N/A**

Order detail ID:	71943756
ISSN:	1533-6794
Publication Type:	e-Journal
Volume:	
Issue:	
Start page:	
Publisher:	AMERICAN INSTITUTE OF AERONAUTICS AND ASTRONAUTICS, INC.
Author/Editor:	American Institute of Aeronautics and Astronautics

Permission Status: ✔ **Granted**

Permission type: Republish or display content
Type of use: Republish in a thesis/dissertation
Order License Id: 4626180946940

Requestor type	Academic institution
Format	Print, Electronic
Portion	chapter/article
Number of pages in chapter/article	14
The requesting person/organization	Armani Batista
Title or numeric reference of the portion(s)	History and Progress of Boundary-Layer Transition on a Mach-6 Flared Cone
Title of the article or chapter the portion is from	History and Progress of Boundary-Layer Transition on a Mach-6 Flared Cone
Editor of portion(s)	Hanspeter Schaub
Author of portion(s)	Brandon C. Chynoweth, Steven P. Schneider, Christoph Hader, Hermann Fasel, Armani Batista, Joseph Kuehl, Thomas J. Juliano and Bradley M. Wheaton
Volume of serial or monograph	56
Issue, if republishing an article from a serial	2
Page range of portion	333–346
Publication date of portion	8 Feb 2019
Rights for	Main product
Duration of use	Life of current edition
	no

Figure B.3: Permission from Copyright Clearance Center for Journal of Spacecraft and Rockets article [43].

G Suite **Armani Batista <abatista@udel.edu>**

Results & Figures Citation Permission Request

3 messages

Armani Batista <abatista@udel.edu> Sat, Jun 1, 2019 at 8:41 PM
To: faselh@email.arizona.edu, christoph.hader@gmail.com

Hi Dr. Fasel and Dr. Hader,

I'm working on my dissertation, and I wanted to ask permission to cite and include some of the figures from your results in a collaboration section? This is regarding the Scitech and JSR review papers for the flared cone Dr. Joe Kuehl and I worked with both of you on (A History and Progress of Research on Boundary-Layer Transition on a Mach 6 Flared Cone).

There is also a flared cone contour plot from another paper ("H. Fasel, J. Sivasubramanian, and A. Laible. Numerical investigation of transition in a flared cone boundary layer at mach 6. Procedia IUTAM, 2015.") if I may cite and include the figure as a benchmark comparison for my flared cone basic state?

I fully understand if they cannot be included though, thank you both for all your help and consideration.

Regards,
Armani

Christoph Hader <christoph.hader@gmail.com> Sat, Jun 1, 2019 at 9:25 PM
To: Armani Batista <abatista@udel.edu>
Cc: "Hermann F. Fasel" <faselh@email.arizona.edu>

Hi Armani,

From my side, you can, of course, cite and include the figures from the Scitech and JSR collaboration paper in your dissertation. If you don't have the eps files of the figures I can send them your way if you tell me which ones you would like to use. This way you could avoid taking screenshots and therefore loss of quality of the figures.

Just let me know if you have any other questions. Good luck with your dissertation and your defense. If you are allowed to then please send us a copy of your dissertation once you're done with everything, we would definitely be interested in your findings.

Best,
Christoph
[Quoted text hidden]

https://mail.google.com/mail/u/0?ik=bf7630729d&view=pt&search=all&permthid=thread-a%3Ar81516041194945037&simpl=msg-a%3Ar-1411059825690089783… 1/2

Figure B.4: Permission from Christoph Hader for DNS sections and content [42, 43].

G Suite Armani Batista <abatista@udel.edu>

Results & Figures Permission Request
4 messages

Armani Batista <abatista@udel.edu> Thu, May 16, 2019 at 2:09 PM
To: "Scalo, Carlo" <scalo@purdue.edu>, "de Carvalho Britto Sousa, Victor" <vsousa@purdue.edu>

Hi Dr. Scalo and Victor,

I'm working on my dissertation, and I wanted to ask permission to cite and include the figures from your results in collaboration sections of my dissertation? This is regarding the Aviation 2018 paper Nonlinear Dynamics of Second Mode Waves on a Hypersonic Flared Cone Dr. Joe Kuehl and I worked with both of you on? I fully understand if they cannot be included, thank you for your consideration.

Regards,
Armani

de Carvalho Britto Sousa, Victor <vsousa@purdue.edu> Thu, May 16, 2019 at 4:18 PM
To: Armani Batista <abatista@udel.edu>
Cc: "Scalo, Carlo" <scalo@purdue.edu>

Good Afternoon Armani,

We are perfectly fine with you including results from our collaboration regarding the Aviation 2018 paper in you dissertation as long as you reference the work.

Thank you,

Victor Sousa
PhD Student, School of Mechanical Engineering
Purdue University, West Lafayette.
[Quoted text hidden]

Scalo, Carlo <scalo@purdue.edu> Thu, May 16, 2019 at 4:20 PM
To: "de Carvalho Britto Sousa, Victor" <vsousa@purdue.edu>, Armani Batista <abatista@udel.edu>

Dear Armani — I second Victor's reply and congratulations on your upcoming defense!

Dr. Carlo Scalo

Assistant Professor of Mechanical Engineering, and
Aeronautical and Astronautical Engineering (by courtesy)
FLEX 2081A, Purdue University
Gates Rd, West Lafayette, 47907
Website: https://engineering.purdue.edu/~scalo/
Webex: https://purdue.webex.com/join/scalo
[Quoted text hidden]

https://mail.google.com/mail/u/0?ik=bf7630729d&view=pt&search=all&permthid=thread-f%3A1633713064957719468&simpl=msg-f%3A1633713064957719468&… 1/2

Figure B.5: Permission from Victor Sousa and Carlo Scalo for DNS sections and content [45].